Characterization of the flagellar beat of the single cell green alga Chlamydomonas Reinhardtii

DISSERTATION

Zur Erlangung des akademischen Grades
Doctor rerum naturalium
(Dr. rer. nat.)

vorgelegt der Fakultät Mathematik und Naturwissenschaften
der
Technischen Universität Dresden

von

Veikko F. Geyer

geboren am 21. Dezember 1979 in Eberswalde – Finow

Gutacher: Prof. Dr. Frank Jülicher und Prof. Dr. Jochen Guck

Eingereicht am: 12. August 2013

Tag der Verteidigung: 23. Oktober 2013

1. Gutachter: Prof. Dr. Frank Jülicher

Max Planck Institut für Physik komplexer Systeme (MPI-PKS)
Nöthnitzer Str. 38, 01187 Dresden, Germany

2. Gutachter: Prof. Dr. Jochen Guck

Biotechnologisches Zentrum (BIOTEC)
Tatzberg 47/49, 01307 Dresden Germany

Declaration

I herewith declare that I have produced this paper without the prohibited assistance of third parties and without making use of aids other than those specified; notions taken over directly or indirectly form other sources have been identified as such. This paper has not previously been presented in identical or similar form to any other German or foreign examination board.

The thesis work was conducted from October 2009 to August 2013 under the supervision of Prof. Jonathon Howard, PhD am Max Plank Institut für molekulare Zellbiologie und Genetik (MPI-CBG) Dresden.

I declare that I have not undertaken any previous unsuccessful doctorate proceedings. I declare that I recognize the doctorated regulations of the Fakultät für Mathematik und Naturwissenschaften of the Technische Universität Dresden.

Erklärung

Hiermit versichere ich, dass ich die vorliegende Arbeit ohne unzulässige Hilfe Dritter und ohne Benutzung anderer als der angegebenen Hilfsmittel angefertigt habe; die aus fremden Quellen direkt oder indirekt übernommenen Gedanken sind als solche kenntlich gemacht. Die Arbeit wurde bisher weder im Inland noch im Ausland in gleicher oder ähnlicher Form einer anderen Prüfungsbehörde vorgelegt.

Die Doktorarbeit wurde von Oktober 2009 bis August 2013 unter der Aufsicht von Prof. Jonathon Howard, PhD am Max Plank Institut für molekulare Zellbiologie und Genetik (MPI-CBG) Dresden durchgeführt.

Hiermit erkläre ich, dass keine früheren Promotionsverfahren stattgefunden haben. Hiermit erkläre ich, dass ich die Promotionsordnung der Fakultät für Mathematik und Naturwissenschaften an der Technischen Universität Dresden anerkenne.

Veikko Geyer

Dresden, im August 2013

Veikko Geyer

> One can't be satisfied with just looking at so wonderful a structure: chiefly because one can't get clear on how such an unbelievable motion is brought about
>
> ---
>
> Antoni van Leeuwenhoek
> June 28, 1713, concerning cilia

Abstract

Subject of study: Cilia and flagella are slender appendages of eukaryotic cells. They are actively bending structures and display regular bending waves. These active flagellar bending waves drive fluid flows on cell surfaces like in the case of the ciliated trachea or propels single cell micro-swimmers like sperm or alga.

Objective: The axoneme is the evolutionarily conserved mechanical apparatus within cilia and flagella. It is comprised of a cylindrical arrangement of microtubules, which are the elastic elements and dyneins, which are the force generating elements in the structure. Dyneins collectively bend the axoneme and must be specifically regulated to generate symmetric and highly asymmetric waveforms. In this thesis, I address the question of the molecular origin of the asymmetric waveform and test different theoretical descriptions for motor regulation.

Approach: In this study I introduce the isolated and reactivated *Chlamydomonas* axonemes as an experimental model for the symmetric and asymmetric beat. This system allows to study the flagellar beat in a controlled and cell free environment. I use high-speed microscopy to record shapes with high spatial and temporal resolution. Through image analysis and shape parameterization, I extract a set of parameters that describe the flagellar waveform. Using *Chlamydomonas* I can make use of different structural and motor mutants to study their effect on the shape in different reactivation conditions. Although the isolated axoneme system has many advantages compared to the cell-bound flagellum, to my knowledge, it has not been characterized yet.

Results: I present a shape parameterization of the asymmetric beat using Fourier decomposition methods and find that the asymmetric waveform can be understood as a sinusoidal beat around a circular arc. This reveals the similarities of the two different beat types, the symmetric and the asymmetric beat.

I investigate the origin of the beat-asymmetry and find evidence for a specific dynein motor to be responsible for the asymmetry.

I furthermore find experimental evidence for a strong sliding restriction at the basal end of the axoneme, which is important to establish a static bend.

In collaboration with P. Sartori and F. Jülicher, I compare theoretical descriptions of different motor control mechanisms to the experimentally gained waveforms and find that a curvature controlled motor-regulation mechanism describes the data best. We find that in the dynamic case an additional sliding restriction at the base is unnecessary.

By comparing the waveforms of intact cells and isolated reactivated axonemes, I reveal the effect of hydrodynamic loading, and the influence of boundary conditions on the shape.

Acknowledgements

Having been introduced to molecular motors by Prof. Stefan Diez, for whom I am very grateful teaching me much of what I understand about science and most I know about *in vitro* reconstitution and microscopy in the most polite and understanding way, I became excited about studying the macroscopic output of molecular motor systems.

Inspired by the initial idea that cooperatively acting motors in a more intact or natural environment would give rise to a more understandable behavior I was looking for a PhD project.

I was fortunate that at this time Prof. Joe Howard introduced me to the axoneme project, which turned out to become a great experience and adventure for the next four years. Working in a completely international group was one of the major experiences. I learned a lot about different ways of thinking and approaching scientific and non-scientific problems and life in general. I am proud and fortunate enough to have been working with such wonderful colleagues.

Overwhelming was the endless scientific freedom and support, Joe Howard provided during the time of my PhD, for that I am deeply grateful and feel honored by.

Starting with establishing a mostly new experimental branch of science in the lab, this work would have been not as enjoyable without the company of Vikram Mukundan and Joshua Alper, whom I am fortunate enough to call my co-workers and my friends. Vikrams excitability for interesting ideas and Joshs endless constructive criticism provided an excellent environment to test and work out crazy ideas. A platform for our discussions was our weekly journal club termed 'Dresden Axoneme Club', which helped me a lot to get familiar with literature and ideas.

After having worked on the project for one year, we established a close collaboration with the group of Prof. Frank Jülicher at the Max Planck Institute for the physics of complex systems whos interest and kind support I am grateful for.

In the tradition of the former PhD students Ingmar Riedel and Andy Hilfinger the new students Pablo Sartori and I started discussing, arguing and speculating about the axonemal beat. For me, it was very interesting how understanding problems with different perspectives can promote insights for both sides and converge into better solutions and approaches.

I also want to point out the help and support of the students Magdalena Preciado López, Adian Wichmann and Laura Catalina Bohorquez. Adian and Magdalena, at the time Master/Diploma students, gave us great support and a valuable start by setting up *Chlaydomonas* and dynein work in the lab. Laura, who worked in the lab as a student helper, I am grateful for helping me with bench-work and data evaluation.

I am also very grateful to Benjamin Friedrich who became a very reliable colleague who was always approachable spend time discussing, teaching and helping with problems. His ability to simplify and direct work was very instructive to me.

I furthermore want to thank the light microscopy facility of the MPI and Peter Pitrone for always being helpful with solving microscopy related problems.

I thank Silke Thüm for always helping me with tracing down publications and providing me a home in the library for the time I was writing my thesis.

I thank Erik Schäffer for being a thesis advisor and for very kind and helpful discussions on the project. For comments on the manuscript and I also thank Pablo Sartori, Benjamin Friedrich, Marija Zanić, Joshua Alper and Joe Howard. For mental support during the writing period, I thank Marija P. and Anita J.

For convincing me to use LaTex to write my thesis and for teaching me how to use it I am grateful to Anita Jannasch, who thereby probably saved me one week of editing a word document.

The invaluable support during this time I perceived from my wife Vera, who provided endless love, understanding and support. Her positive attitude towards live enabled me to do this work. She also blessed me with the most beautiful gift: our 2 children Hannah and Lukas, whom I thank for their understanding and the time that they left me with my work.

Finally, I want to thank my parents who stayed a reliable and supportive source of energy during the whole time of my studies. Their fascination and devotion to science mainly influenced me on my way and was a reason for my desire to become a scientist.

Contents

Chapter 1

Introduction

1.1 Biology of Cilia and Flagella

Swimming at the micrometer scale is different from our every day experience of swimming. In the regime of small Reynolds numbers where inertia is negligible compared to viscous forces, micro-swimmers had to develop specific strategies for propulsion [Purcell, 1976].

Prokaryotic cells generally achieve propulsion by the use of bundled bacterial flagella, which are hollow whip like tubes made from flagellin [Namba et al., 1989]. The beat is driven by a rotatory stepping motor, which used the proton motive force [Sowa and Berry, 2008]. The flagellum itself is a passive structure.

Eukaryotic cells can have cilia or flagella that are membrane enclosed organelles that protrude from the cell body [Lodish, 2012]. They are actively bending structures [Machin, 1958]. Their beat is characterized by bends that propagate along the structure as the result of the concerted action of force generators [Gibbons, 1982] distributed along the entire length [Afzelius et al., 1995, Bui et al., 2012]. The internal structure in eukaryotic cilia and flagella is the **Axoneme**. It shows amazing evolutionary conservation [Carvalho-Santos et al., 2011] and has key functions in embryo development, fluid propulsion and cell locomotion. Due to the evolutionary conservation of the structure, the results gained with one type of cilia usually have implications on other organisms as well. The number of cilia on a single cell can reach from 1, like in the case of sperm cells to several hundreds in the case of *Paramecium* and *Tetrahymena* [Vincensini et al., 2011]. In organisms, cilia are closely arranged on tissue surfaces. To fulfill their functions these flagella synchronize their beat and exhibit the so-called metachronal-waves which, then drive fluid flows over long distances [Elgeti and Gompper, 2013].

In this thesis, I am only considering eukaryotic cilia. The reader might also find the terms cilia and flagella used interchangeably where cilia is usually used for organisms that possess more than 2 flagella and therefore is the more general term. The term axoneme I use for demembranated *Chlamydomonas* flagella.

1.1.1 The dimensions of flagellated micro-swimmers

Single cell micro-swimmer can have flagella with greatly different length from 5 to 1000 μm that are capable of producing the characteristic periodic bending waves. Sperm flagella show the greatest range of length: The *Anopheles* sperm reaches into the mm range, bull sperm has a length of 60 μm and sea urchin sperm is 30 μm long as shown in Figure 1.1 . *Trypanosoma* , which is a human parasite and responsible for the sleeping sickness, uses its 30 μm long flagellum to propel itself through the bloodstream. The green alga *Chlamydomonas reinhardtii* has two approximately 12 μm long flagella see Figure 1.1, the shortest of the presented species. It uses the coordinated beat of these two flagella to swim.

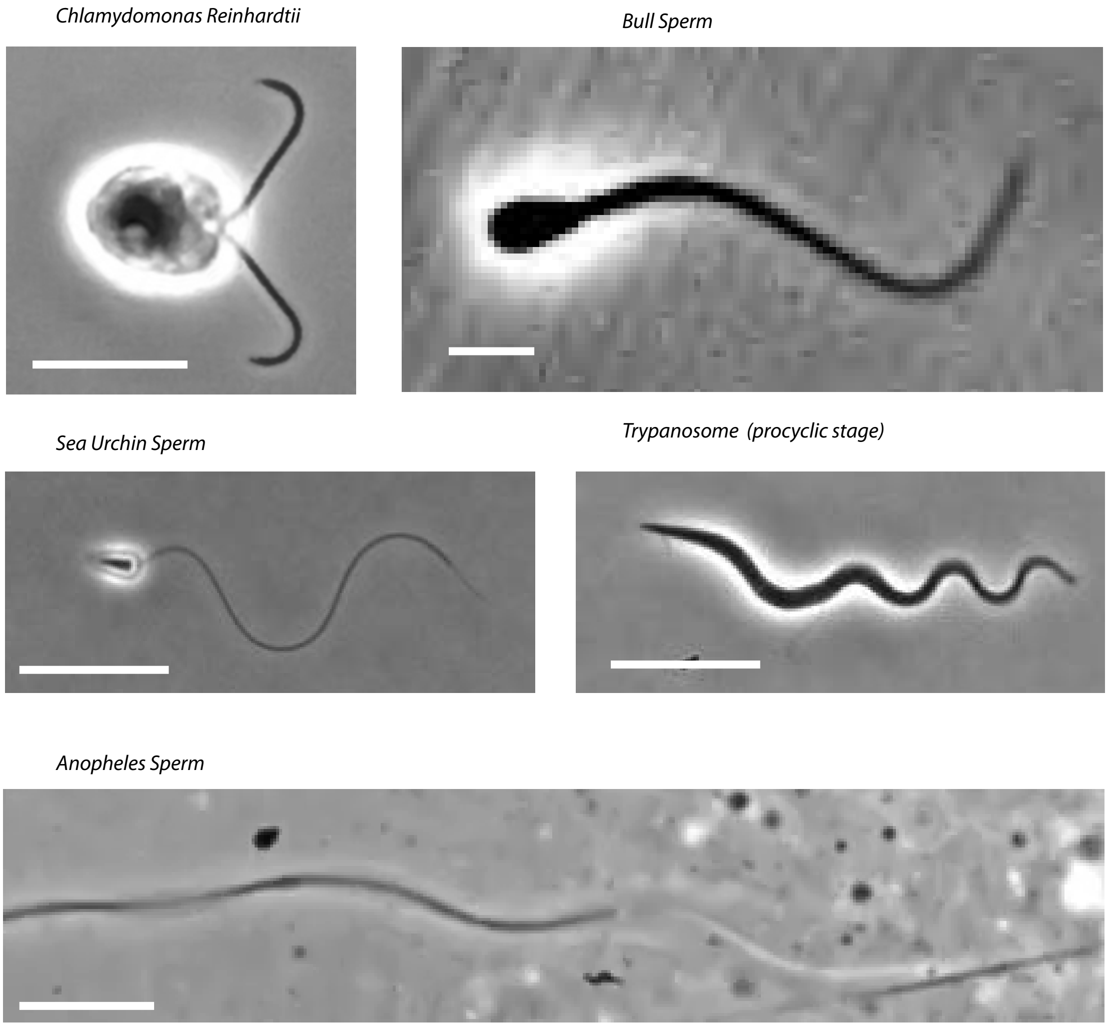
Chlamydomonas Reinhardtii

Bull Sperm

Sea Urchin Sperm

Trypanosome (procyclic stage)

Anopheles Sperm

Figure 1.1: Flagellated micro-swimmers. Phase-contrast micrographes of various flagellated micro-swimmers. The bull-sperm image has been taken by Ingmar Riedel-Kruse, all other images were taken by Veikko Geyer. Scale bars are 10 μm

1.1.2 The symmetric and the asymmetric beat

Among the presented species we find two major differences in the waveforms: The symmetric and the asymmetric beat. The symmetric, more sinusoidal waveform is typically found in sperm cells. The aymmetric waveform is found in the cilia of the airways and in *Chlamydomonas* cells, see Figure 1.2. The difference in waveform affects the swimming behavior: sperm cells swim with their head forward (Figure 1.2 A) so that they reach to the egg with the head first. They change directionality by changing their mean shape, which is related to the radius of their swimming path [Friedrich et al., 2010] . *Chlamydomonas* drags its cell body as it swims forward. During forward swimming cells change their swimming direction by skipping a beat in one of the flagella [Polin et al., 2009, Rüffer and Nultsch, 2005].

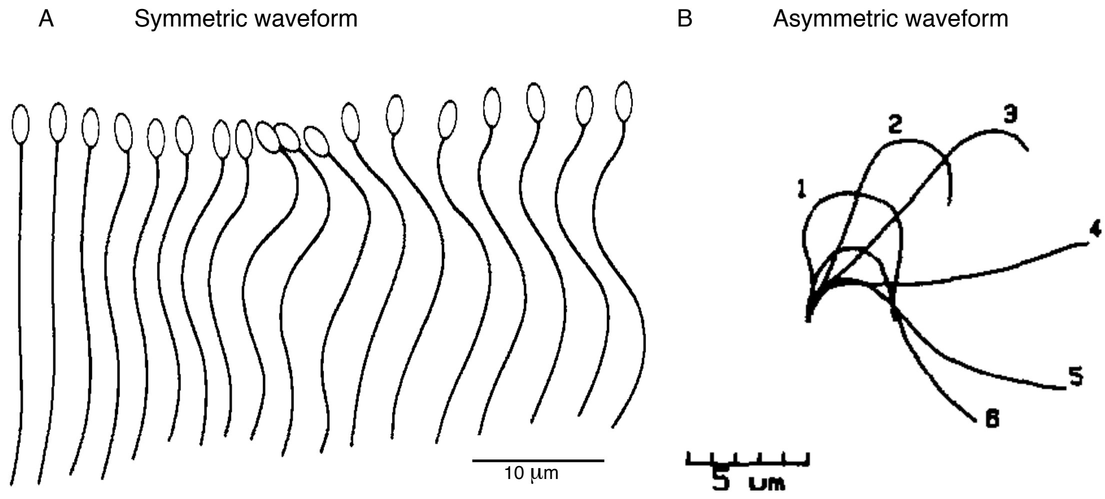

Figure 1.2: The symmetric and asymmetric waveform. Flagella can exhibit different types of waveforms. **A** The symmetric waveform, sea urchin sperm, [Rikmenspoel, 1978]. **B** The asymmetric waveform, here from a *Chlamydomonas* flagellum, [Brokaw et al., 1982]. The numbers denote the time progression of the shapes.

Since the axonemal structure is highly conserved it is interesting to ask characterize the difference between these two types of waveforms and to ask: What is the molecular origin for the difference?

1.1.3 Chlamydomonas reinhardtii as a flagella model

The specific focus of this thesis lies on the single-cell green alga *Chlamydomonas reinhardtii*, see Figure 1.1, that has been used as a model organism to study the eukaryotic flagella for decades (Brokaw and Luck, 1983; Hyams and Borisy, 1975; Ringo, 1967; Witman et al., 1978). *Chlamydomonas* uses the coordinated beat of its two flagella to swim to nutrient sources and to the light.

Swimming description of the cell: In the literature, its swimming is usually compared to the brest-stroke like swimming of a human that consists of a breast and a recovery stroke. In Figure 1.2 B the breast stroke is numbered 3-6 where the axoneme performs its principle bend, the recovery stroke is numbered 1-3 where the axoneme performs its reverse bend.

For my studies, *Chlamydomonas* is an interesting model because: 1. An extensive library of strains, including those with mutations in cilial proteins, is made publicly available by the University of Minnesota at chlamycollection.org; 2. cells can be induced to de-flagellate, and the isolated flagella can be reactivated in controlled and cell-free environments, in which one wants to study cilia; 3. *Chlamydomonas* flagella can exhibit both the symmetric, sperm-like waveform, and the asymmetric, cilia-like waveform; 4. *Chlamydomonas* can be grown in sufficient quantity to purify components for in vitro biophysical and biochemical studies. Although short, *Chlamydomonas* flagella can be visualized by light microscopy.

1.2 The axoneme is the internal structure in eukaryotic cilia and flagella

The axoneme is the conserved mechanical structure in eukaryotic cilia and flagella [Carvalho-Santos et al., 2011]. A cartoon of a cross-section of a typical motile axoneme is presented in Fig. 1.3. It shows the internal arrangement of the key axonemal components: The microtubule doublets and the Dynein motors.

Radial arrangement: 9 doublet microtubules are cylindrically positioned around a pair of singlet microtubules [Afzelius et al., 1995, Ringo, 1967]. Dynein motors are statically attached to the A-tubule of each doublet, mechanical linker-elements like nexin-links connect adjacent microtubule doublets, radial spokes fill the space between the doublets and the central pair microtubules as shown in Figure 1.3 A. The axoneme has a diameter of about 200 nm, the spacing between adjacent doublets is about 30 nm [Nicastro et al., 2006]. The A to- B tubule arrangement of the adjacent doublets and the specific binding of dyneins to the B-tubule gives the axoneme a radial polarity.

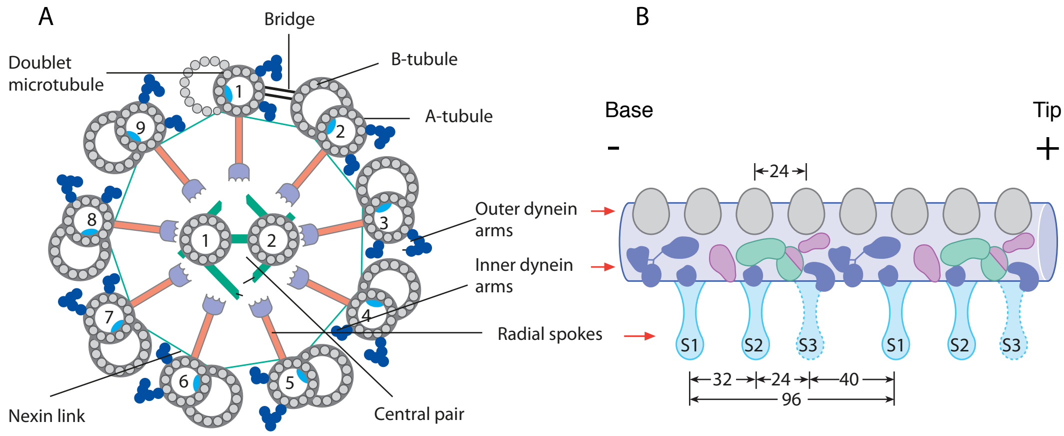

⊗ View from **base** (proximal end) to **tip** (distal end)

Figure 1.3: Cartoon of the axonemal structure. **A** Cross-section of the axoneme. **B** Longitutional-section of one microtubule doublet. Adapted from [Linck, 2001]

Longitudinal arrangement: The presented cross-section in Fig. 1.3 A shows atypical cross-section of an axoneme. The described elements have a repeating longitudinal arrangement with a 96 nm periodicity (see Figure 1.3). Each segment contains 4 outer arm dyneins (OAD), which are positioned on the outside of the A-tubule and 7 inner arm dyneins (IAD), which are positioned towards the inside of the axoneme. Each repeat contains 3 radial spokes, which point towards the central pair. This motor arrangement gives the axoneme a longitudinal polarity.

The ends of the axoneme: The ends of the axoneme are distinct from each other. The proximal end or the basal-end nucleates from the centriol, which is a microtubule-based cylindrical organelle in *Chlaydomonas* and named the basal body see Figure 1.4 A. The basal body is structurally different from the axoneme. Triplet microtubules, which are called microtubule swords are arranged in a cylindrical manner. The outgrowing triplet looses one microtubule in the so-called transition zone and by the end of which the axoneme has doublets and gains the central pair see Figure 1.4 A1. The distal tip is an up to 1 μm long region in which the outer doublets are lost and just the central pair sticks out of the end of the cylinder see Figure 1.4 A10. As any microtubule, the doublet microtubules have a given polarity. Doublets point with their minus ends towards the basal body and with their plus ends towards the distal tip. The microtubule polarity gives an additional longitudinal polarity to the axoneme.

The axoneme is a chiral structure: The combination of the different asymmetries makes the axoneme a chiral structure: The parallel arrangement of microtubules, which are polar structures, gives longitudinal polarity to the axoneme. Dyneins, are exclusively attached to the A-tubule of the microtubule doublet, which gives the structure a radial polarity. The combination of longitudinal and radial polarity makes the axoneme a chiral structure. Whether this chirality reflects back on the axonemal beat is not known. The chirality is tied to the force production via the arrangement and the directionality of the motors. Therefore it is conceivable, that the chirality of the axoneme reflects on the swimming behavior of the cell and the axoneme, which is discussed in Section 4.3.3 .

The *Chlamydomonas* axoneme can be severed from the basal body: This transition region contains the so-called stellate structure, which shows a star-like arrangement of fibers as depicted in Figure 1.4 A. Centrin, a Ca^{2+} sensitive 20 kD protein, is a main component of these fibers [Wiech et al., 1996] . The presence of calcium the diameter of the axoneme is decreased (see Figure 1.4). This suggests a contraction of these fibers [Sanders and Salisbury, 1989]. This reduction of diameter is thought to contribute to the severing of the outer doublet microtubules and hence to flagellar release Fig. 1.4. Another severing factor is thought to be a katanin-like protein, which has shown to also localize to the basal body and is likely to be involved in calcium-induced axonemal microtubule severing [Lohret et al., 1998]. Increased calcium influx can be induced by pH shock or by the application of poisons like the anesthetic dibucaine [Bessen et al., 1980, Quarmby, 1996] . I use the deflagellation response as a method to isolate flagella for biochemical or biophysical studies, see Section 3.1.2 .

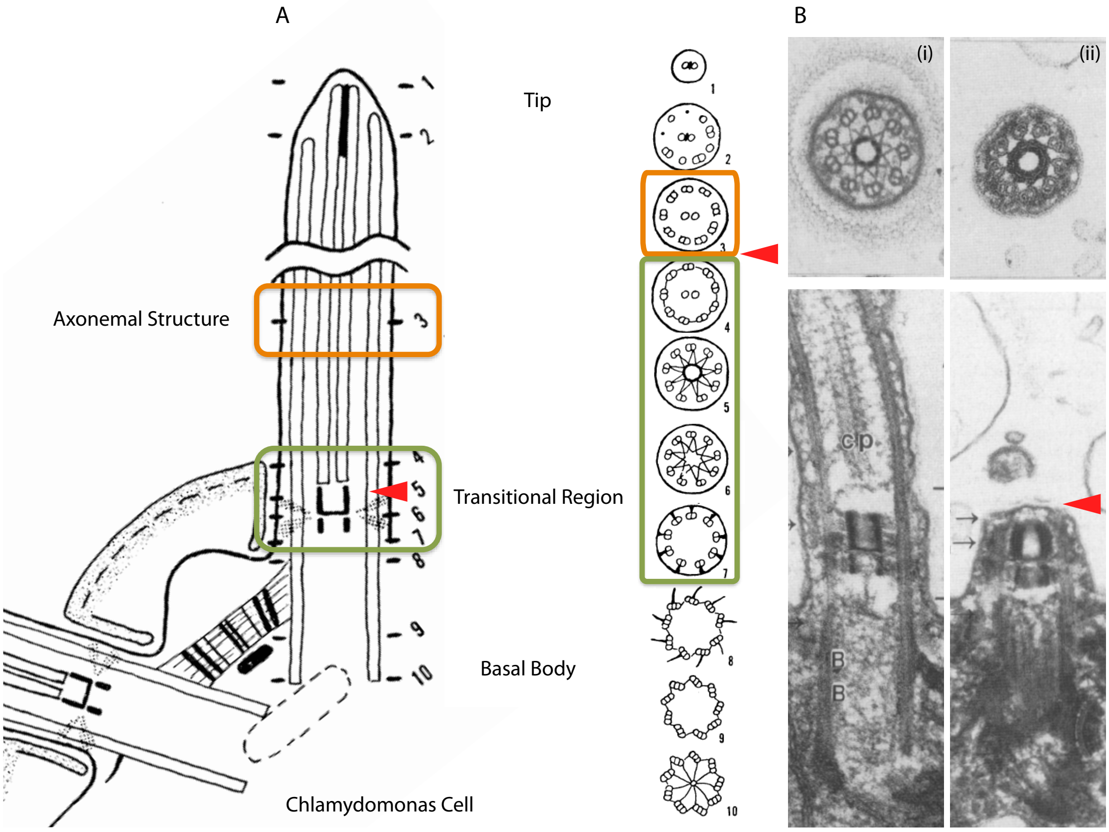

Figure 1.4: Longitudinal sections of the chlamydomonas axoneme. (A) Schematic of the different longitudinal regions and related cross-sections of the *Chlamydomonas* axoneme from [Ringo, 1967]. **(B)** Electron micrograph of the flagellum and the stellate structure in **(i)** absence of calcium and **(ii)** in presence of calcium from [Sanders and Salisbury, 1989]
.

The isolated axoneme can be reactivated and it has been reported that the waveform after severing closely resembles the waveform of the cell attached flagellum [Bessen et al., 1980]. This is surprising since the detachment from the cell body cases a dramatic change in boundary conditions. Therefore, it is interesting to compare these two waveforms more rigorously, which will be discussed in Section 4.2.4. After deflagellation, the orientation of the axoneme with respect to the cell-body is lost and the direction of wave-propagation can not be determined. Thus, it is interesting to find a way to distinguish the distal from the basal end. This problem is discussed in Section 4.1.2.

1.3 Structure and function of microtubules and dyneins

The main structural components in the axoneme are microtubules and the force generators are the dynein motors. This section summarizes their specific properties.

1.3.1 Microtubules: The structural elements in the axoneme

Biological functions: In eucaryotic cells, microtubules fulfill scaffold-like functions and in large part determine their mechanical properties. They usually show a radial organization and serve as tracks for motor proteins like kinesin-1 and cytoplasmatic dynein that drive intracellular transport. Moreover, microtubules fulfill major tasks in the cell proliferation by forming the mitotic spindle. Microtubules also serve as the main structural elements in the axoneme of eukaryotic cilia and flagella.

Structure of microtubules: Microtubules are hollow cylinders with an outer and inner diameter of about 25 and 15 nm, respectively. The mechanical properties of microtubules are summarized in Table 1.1. Most cellular microtubules consist of 13 protofilaments [Tilney et al., 1973] , which run parallel to the long axes of the microtubule as shown in Figure 1.5 B. A protofilament is formed from tubulin heterodimers, which consist of α and β tubulin monomers. A crystal-structure of the tubulin-heterodimer is shown in Figure 1.5 A. The monomers are 50 kDa globular GTP-ases that interact longitudinally in a head to tail manner to build up the protofilaments. Neighboring protofilaments associate laterally to build tubes. Tubulin heterodimers, protofilaments and microtubules have an intrinsic polarity because there is α tubulin on one end of the microtubule and β tubulin end on the other. These two ends have a different affinity for free GTP tubulin and thus different growth speeds. Due to this difference they are termed the plus and minus end: plus for the 2x faster growing α-tubulin displaying end, minus for the more slowly growing β-tubulin displaying end [Walker et al., 1988] .

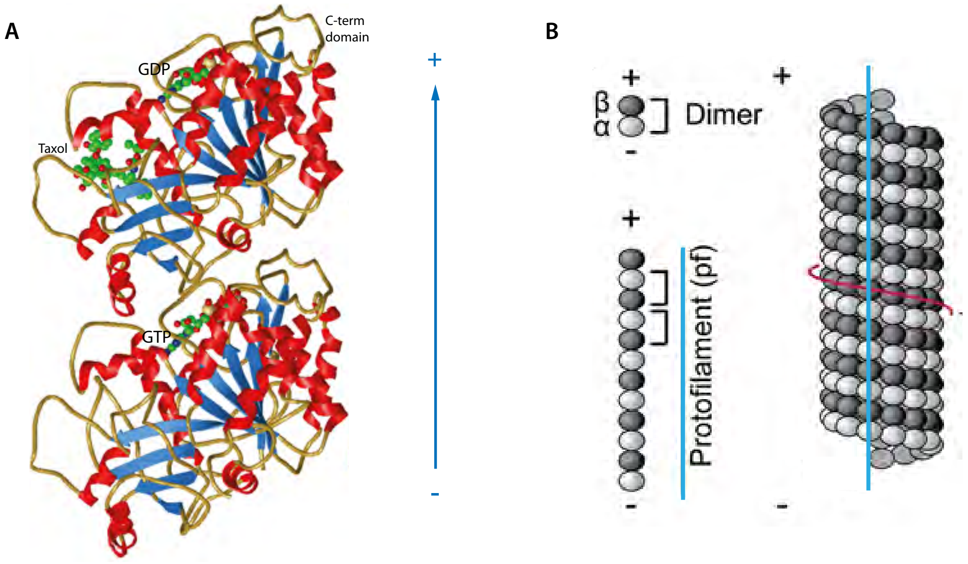

Figure 1.5: The microtubule structure. Cartoon of the microtubule and its substructures. **A** Ribbon diagram of the structure of the $\alpha\beta$ tubulin heterodimer solved by electron crystallography. The structure of bovine-brain tubulin in complex with Taxol, a microtubule stabilizing drug, is shown in an orientation corresponding to the outside view of a microtubule. GDP is bound to β tubulin [Nogales et al., 1998]. **B** Cartoon of the polar microtubule substructures,the tubulin heterodimers, the protofilaments and the closed 13 protofilament 3-start microtubule. Figure is adapted from [Coquelle et al., 2009].

Microtubule doublets in the axoneme: In the axoneme microtubules are arranged in doublets consisting of a A and B tubule. The A microtubule is a 13 protofilament-microtubule and core of the doublet. The B-microtubule consists of 10 and a half protofilaments and is associated to the A-tubule in a half open manner. Compared to a singlet microtubule, the bending rigidity of a doublet microtubule is 3 times higher. This is mainly due to the geometry and the extra material of the B tubule. For the whole axoneme this works out to ~30 times the bending rigidity of a 13 protofilament microtubule [Howard, 2001]. MAPs do not significantly contribute to the stiffness of the axoneme [Mickey and Howard, 1995]. A summary of the measured mechanical properties of flagella and axonemes can be found in Table 1.1.

1.3.2 Dyneins: The force generators that drive the axonemal beat

Biological functions of dyneins Dyneins are a family of molecular microtubule-motors that fulfill various tasks in the cell: Cytoplasmic dyneins realize retrograde transport of vesicles, they have been shown to be involved in producing pulling forces on astral microtubules during cell devision while being bound to the cortex. Axonemal dyneins drive the beat of eukaryotic cilia and flagella.

Structure of cytoplasmic dynein The fine structural details of dynein are known from the crystal structure of cytoplasmic dynein [Carter et al., 2011, Kon et al., 2012, Schmidt et al., 2012] as shown in Figure 1.6 B. Axonemal dynein has been crystallized lately and shows a great similarity to cytoplasmic-Dynein [Roberts et al., 2012]. All Dyneins have a ca. 300 kDa motor domain consisting of a ring of six non iden-

Table 1.1: Flexural rigidity of microtubules, axonemes and sperm.

Object	Flexural Rigidity $10^{-24}\,Nm^2$	Source and condition
Microtubule	26±2	Bovine brain microtubule (1)
Microtubule	7.9±0.7	Bovine brain microtubule (2)
Microtubule	2±0.8	Bovine brain microtubule Taxol stabilized (2)
Sperm	900±300	Demembranated sea urchin sperm ADP+Vanadate (3)
Sperm	1 900±200	Demembranated sea urchin sperm ATP (3)
Sperm	10 000±1000	Demembranated sea urchin sperm Rigor (3)
Axoneme	400±150	Chlamydomonas axoneme ATP+Vanadate (4)
Axoneme	2700±1100	Chlamydomonas axoneme ATP (4)
Axoneme	10 000±1000	Chlamydomonas axoneme Rigor 4)

Unit conversion: $10^{-24}\,Nm^2 = pN\mu m^2$. Values are (Mean±SEM,N=7),
(1)[Mickey and Howard, 1995],
(2)[Kikumoto et al., 2006] Values are (Mean±SD,N=25) Microtubule lengh-independent measurement using the buckling force by optical tweezers. The authors report a 4x decreased stiffness for taxol-microtubules consistent with [Felgner et al., 1996, Kikumoto et al., 2006, Kurachi et al., 1995].
(3) [Howard, 2001]
(4) Demembranated WT axonemes. Data from a talk at the Biophysical Society meeting in San Diego: Flexural Rigidity and Shear Stiffness of Flagella, Gang Xu from Philip V. Bayly's lab at Washington University, Saint Louis, MO, USA.

tical AAA+ domains called AAA1-AAA6 as depicted in Figure 1.6 A. Four of them AAA1-4 are capable of binding and hydrolyzing ATP [Mocz and Gibbons, 1996]. Only the AAA1 domain is linked to force production and drives the cyclic relocation of the so-called linker-domain [King, 2011, Kon et al., 2004] shown in Figure 1.6 A. The linker-arm-domain is allocated with the AAA1 domain that reaches across one side of the ring and connects the motor to the stem or tail region [Burgess et al., 2003]. This tail mediated motor interactions with either (1) cargo in the case of cytoplasmic dynein or (2) doublet microtubules in the case of axonemal dynein [Tynan et al., 2000]. The motor - ring is interrupted between AAA4 - AAA5, from where a 10 nm long coiled-coil stalk emerges. At its distal tip a small globular region, the microtubule binding domain, is located [Gee et al., 1997]. The location of this domain is interesting, since it is almost opposite to the force generating AAA1 domain. This implies, that the ring can support a moment.[Samso and Koonce, 2004]

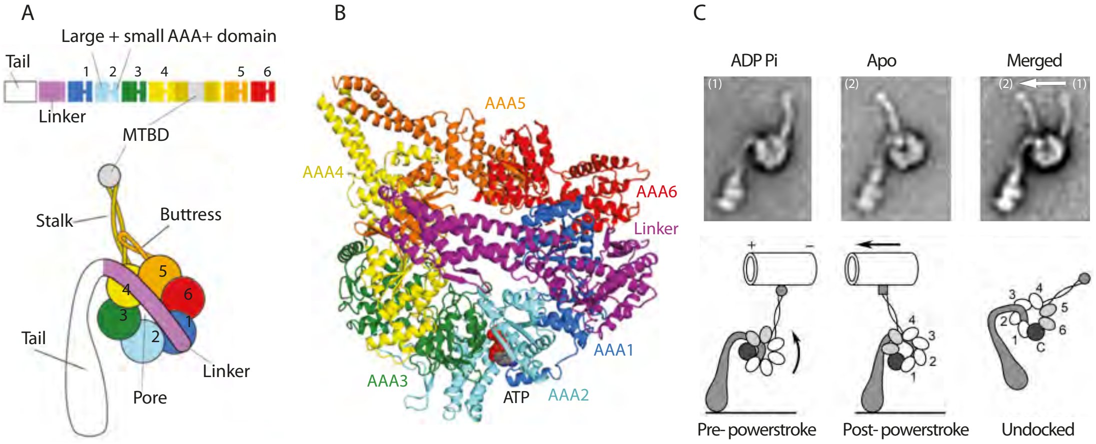

Figure 1.6: Structure and power stroke of Dynein. A Cartoon of gene and structure of dynein. **B** Crystal structure of the motor-domain of *Saccharomyces cerevisiae* cytoplasmic dynein [Schmidt et al., 2012]. **C** Averaged electron-micrographs of *Chlamydomonas* IDA c at the start and end of its power stroke. The different pre and post - power-stroke states are mimicked by vanadate and nucleotide depletion, respectively. [Burgess et al., 2003]

Hydrolysis cycle of dynein Dynein is strongly bound to the microtubule in the ADP or nucleotide free state. ATP binding weakens the dynein-microtubule interaction while the linker arm moves to its pre-power-stroke position. This is considered to happen very fast, at a rate of 180 s^{-1}. This conformational change is followed by nucleotide hydrolysis and phosphate release. ADP release represents the rate limiting step of the force production cycle and happens at a rate of 0.2 s^{-1}. During that step, the affinity of dynein for the microtubule is increased and it is thought to be followed by the power stroke of the linker-arm-domain. In the nucleotide free state the affinity dyneins affinity for the microtubule is high [King, 2011].

Power stroke and force production Dynein conformations in different nucleotide states have been studied using electron microscopy as shown in Figure 1.6 C. These studies show that in the ATP or ADP+P_i bound state (weakly bound state, pre-power-stroke confirmation) the tail-domain extents of the ring at a position near the AAA2 domain. In the nucleotide free state (strongly bound state, post-power-stroke confirmation) the tail emerges at the base of the microtubule binding stalk, close to the AAA4 domain [Burgess et al., 2003, Roberts et al., 2009]. These findings illustrate that dynein's power stroke differs from the power stroke produced by other cytoskeletal motors. Unlike kinesin or myosin motors, dyneins do not rotate their motor heads and maintain a roughly constant angle with respect to the microtubule [Ueno et al., 2008]. The power stroke is produced by ATP-dependent remodeling of the linker and an unconventional sliding movement of the helices in the stalk [Carter, 2013].

The axoneme contains various dyneins The *Chlamydomonas* axoneme contains 14 different kinds of dynein motor domains that contribute to the beat [Witman, 2009]. Dyneins are subdivided into outer (OAD) - and inner(IAD)- arm dyneins, which are located on the outer and inner side of each A-tubule respectively as shown in Figure 1.3.
Outer arm dyneins (OAD) There is only one kind of outer arm dynein. It consists of tree stacked dynein motor domains. The motor domains are called $\alpha\beta\gamma$ heavy chains.
Inner arm dyneins (IAD) Inner arm dyneins have several species. The 7 most abundant ones are named with the letters a to g: They are all single headed except IAD f, which consists of 2 heavy chains. Three more IAD with a much lower abundance have been identified lately [Yagi et al., 2009]. Names and properties of the different species are summarized in Table: 1.2. Outer arm dynein and inner arm dyneins have a huge variety of light and intermediate chains, which I will not discuss in this thesis. Interestingly, OAD and IAD f are bound to docking complexes (DC) that specify the longitudinal position of the dynein arms. In the case of OAD, the DC's bind with a 24 nm spacing to the A-tubule and therewith define the positioning of the motors. All these microtubule-binding proteins find exact positions on the microtubules. This implies that in addition to the 8 nm periodicity of the tubulin dimers, there is some kind of molecular ruler on the microtubule. In axonemes of sea urchin sperm tektin has been proposed to play this role [Norrander et al., 1996] , however in *Chlamydomonas* such ruler proteins currently remain unknown [Pigino et al., 2012] . However, the periodicity of the OAD's could be reconstituted on microtubules polymerized *in vitro* in the presence of axoneme extract [Oda et al., 2007] , which might suggest that specific proteins fulfill that function.

Biochemical and biophysical properties of axonemal dyneins
Dynein assays: On way of accessing the dynamic properties of axonemal dyneins is their reconstitution in a microtubule gliding assay [Kagami and Kamiya, 1992, Sakakibara and Nakayama, 1989]. In these assays one has no control over the orientation of the dyneins with respect to the microtubule, however general motor properties like collective transport speeds, duty ratio, pitch and direction of microtubule rotation and the ATP dependence of both can be accessed.
Duty ratio: Axonemal dyneins have been found to have a low duty ratio of approximately 0.1, which means that they only spend 10 % of their time being attached to the filament see [Howard, 2001] . One exception to that rule is the IADf, which has been

reported to have a duty ratio of 0.6-0.7% [Kotani et al., 2007] .
Microtubule gliding velocity and ATP-affinity: To determine nucleotide binding affinities from filament gliding assays the Michaelis Menten kinetics model was applied to the ATP dependent gliding speed and the K_M value was calculated. The K_M value defines the nucleotide concentration at half-maximal gliding velocity V_{max} and is a measure for the dynein affinity for its nucleotide ATP. Properties of different dynein sup-species are summarized in Table: 1.2 . These values show that IAD *c* translocates microtubules at the highest velocity while IAD *f* is the slowest subspecies, IAD *b* has the highest affinity for ATP, while IAD *c* and the OAD $\alpha\beta$ have the lowest.
Dyneins rotate microtubules: Interestingly all IAD except IAD *b* rotate microtubules clockwise when viewed from the minus end while the OAD's do not. This implies that torque generation is a feature common to many of the inner arm dyneins. Subspecies *c* showed a constant, ATP independent pitch of 0.4-0.5 μm while subspecies *g* showed a linearly increasing pitch from about 0.2 to 0.5 μm. The pitch varies because the apparent K_m for ATP for translocation and rotation differs: $31.5 \pm 5.3\,\mu$M (mean ± SD) translocation velocity and $10.6 \pm 2.1\,\mu$M for rotation frequency. In contrast, the two kinds of movements caused by subspecies *c* had almost identical K_m values: $79.4 \pm 11.5\,\mu$M and $67.4 \pm 9.1\,\mu$M [Kagami and Kamiya, 1992].

This is an overview on the properties of the different dynein species. However, calculating K_m values using the gliding velocity could be somehow problematic since ATP hydrolysis in the presence of microtubules, force production and gliding behavior must not directly relate to ATP turn over and thus could alter the gained values. One example for that is the study on IAD*f* and IAD*c* by [Kotani et al., 2007]. The authors report K_m values gained from the gliding assay and ATP-ase assay. For IAD *c*, they find the measured K_m values in the ATP-ase assay to be 3 times lower than in the gliding assay. This emphasizes the difference of these two assays and the hints towards the microtubule activated ATP-ase activity of dynein.

Table 1.2: Microtubule translocation caused by different dynein subspecies

OAD				
Heavy chain (HC)		$\alpha\beta$	γ	β
Velocity	(μm/s)	5±2	4±2.5	1±1
V_{max}	(μm/s)	7	7	2
K_{m}	(μM ATP)	110	45	200*
Rotation		-	-	-

Values: Mean±SD.Assay condition for gliding-velocities: 1 mM ATP
* Hypothetical value: behavior did not follow Michaelis-Menten kinetics. Source: [Sakakibara and Nakayama, 1989].

IAD - species	a	b	c	d	e	f^*	g
Alternative name	$I2'$	$I3'$	$I2A$	$I2'$	$I2B$	$I1\alpha\beta$	$I3$
Heavy chain (HC)	$DHC6$	$DHC5$	$DHC9$	$DHC2$	$DHC8$	$DHC1/10$	$DHC7$
Velocity (μm/s)	3.1±0.5	2.3±0.9	6.8±1.4	5.5±1.3	2.9±0.9	0.76	3.3±0.7
V_{max} (μm/s)	4.3±0.9	2.3±0.1	10.7±1.2	7.8±0.4	3.9±0.2	1.6±0.1	5.8±0.6
K_{m} (μM ATP)	32±14	10.3±4.7	86±14	44±10	22±6.7	55±11	37±9
Rotation	+	-	+	+	+	+	+

Additional IAD species: Data was obtained from [Kotani et al., 2007]. *Species f gliding velocity obtained from [Smith and Sale, 1991]. Additionally, 3 low abundance IAD's, $DHC3$, $DHC4$ and $DHC11$ have been identified but not tested in *in vitro* assays yet [Yagi et al., 2009]. Values: Mean±SD of measurements in triplicate. Assay condition for gliding-velocities: 100 μM ATP. Source: [Kagami and Kamiya, 1992]

Dynein Mutants A huge variety of *Chlamydomonas* mutants have been characterized over the years. These mutants are maintained and made available via *chlamycollection.org* a collection of the Chlamydomonas Resource Center of the University of Minnesota. Among plenty of others, there are dynein mutants, strains with structural mutations or mutations on associated structures like DRC, light or intermediate chains. Table 1.3 summarizes interesting mutants and details the defects of the ones which have been used in this study. A general observation on the level of the organism is that dynein mutants swim slower. This can be due to a reduced beat frequency like in the case of ODA1 and IDA5 or due a alteration of waveform like in the case of IDA3. Although they have different swimming behaviors, all these mutants beat with the asymmetric waveform typical for *Chlamydomonas*. There are a couple of mutants that have been classified paralyzed. Paralyzation can be due to different mutations: Dynein mutations in the inner and outer dynein arms, central pair-related mutations and radial spoke related mutations [Silflow and Lefebvre, 2001]. For paralyzed dynein mutants it has been shown that additional mutations, often in the DRC, can partially rescue motility by introducing so-called suppressor-mutations [Piperno et al., 1992]. These mutants are very interesting since they pave the way to finding the minimal system with the sufficient and necessary components for the axonemal beat. Cells with a mutation in the MBO gene exhibit a symmetrical waveform. They are missing the beak- like projections in The B tubules of doublet 1,5 and 6. There is also a variety of mutants with defective inter-flagellar transport (IFT), which is important for the assembly of the axonemal structure. Some of these mutants have flagella that can reach a length of 30 μm, which is approximately 3 times the length of a wild type flagellum.

Table 1.3: Table of mutants

Strain	Missing component/ Mutated gene	Phenotype	Beat frequency (Hz)/ Swimming velocity (μm/s)/ Flagellar length (μm)
wt	-		51±12/136±12/ 11.1±1.9
oda1	OAD $\alpha\beta\gamma$/ DC 2		23± 3/ 47± 6/ 11.4±2.0
ida1	IAD f/ 1α (DHC1)		45± 6/ 78± 9/ 10.9±1.6
ida3*	IAD f		45± 5/ 77± 11/ 10.2±1.8
ida7	IAD f/ IC140		
bop5	IAD f/ IC138		
ida5	IAD a,c,d,e/ Actin		42±16/ 75±11/ 12.4±1.2
ida9	IAD c/ DHC9		52±11/110± 8/ 11.8±1.8
ida10	IAD b/ DHC5	paralyzed	
pf23	IDA a,c,d,f	twitching - no beat	
mbo2	A-tubule beaks	symmetrical waveform	
fa	Fa1	impaired flagellar autotomy	
lf1		long flagella	

Table was adapted from [Witman, 2009].
*Kamiya et al. [1991]

1.3.3 The asymmetries in the axoneme and consequences for the beat

Asymmetric distribution of dyneins The arrangement of inner and outer arm dyneins in the axoneme repeats every 96 nm (see Fig. 1.3). Tomogram averaging revealed that each repeat in general contains 4 OAD's and 7 IAD's, as well as two radial spokes and one DRC-Nexin complex [Heuser et al., 2009]. Detailed studies using novel electron-tomography and sub-tomogram averaging techniques revealed asymmetries in the radial and longitudinal distribution of dyneins [Bui et al., 2012, Yagi et al., 2009] and cross-linkers [Pigino et al., 2012]. A typical arrangement of the dynein subspecies in the 96 nm repeat is shown in Fig. 1.7 B (Central). This arrangement is only found in the central part of MTD 2-8 of axoneme while the arrangement in the remaining parts is more diverse: Most noticeably there are no OAD on MTD 1. The IAD also shows asymmetric arrangement: IAD b is missing in the proximal of all MTD's and on the entire length of MTD 9, IAD c is missing on MTD1 and IAD f is absent in the proximal part of MTD1 [Bui et al., 2012] (see Fig. 1.7). In the proximal part dyneins with a low abundance, the so-called minor-dyneins $DHC3$, $DHC4$ and $DHC11$ have been identified [Yagi et al., 2009].

Asymmetric distribution of cross-linkers in the axoneme: Adjacent MTD's are connected by various structures: MTD 1 and 2 are connected by the so-called 1-2 bridge, a static cross-link with an 8 nm periodicity in the first half, the proximal part of the axoneme [Bui et al., 2012, Hoops and Witman, 1983]. The most discussed cross-linker nexin is contained in every 96 nm repeat as part of the DRC complex [Heuser et al., 2009] . It is thought to be an elastic element with nonlinear stiffness, restrict the sliding of adjacent doublets as it stretches to approximately 10 times of its equilibrium length [Lindemann et al., 2005] . Additional filamentous linkers, which could also restrict local sliding have been identified lately between MTD 9-1, MTD 5-6 and MTD 1-2 [Pigino et al., 2012] . Another asymmetry unique to the *Chlamydomonas* axoneme are beak like protein structures in the lumen of the B-tubule of MTD 1, 5 and 6 [Hoops and Witman, 1983] . It has been shown that these beaks are continuous filaments that span through the entire length of the axoneme [Pigino et al., 2012] , which makes them an interesting additional structural element. The position of the beak inside the B-tubule is almost opposite the row of OAD on the A-tubule, which could make them being a candidate for OAD regulation. A whole additional group of MIP's (microtubule internal protein) which are located in the inside of the A and B tubule have been described lately [Pigino et al., 2012] . Two of these MIP's, MIP 3A an MIP 3B have a 96 nm periodicity and are localized opposite to the row of IAD's [Nicastro et al., 2006] .

Structural determination of the beating plane *Chlamydomonas* flagella exhibit an almost planar beat, which is achieved by the conversion of sliding to bending in the presence of cross-links see Section 1.4 . The beating plane is likely to be defined by asymmetrically distributed cross-linkers. It is thought that the main contribution comes from the bridge between DMT 1 and 2 [Hoops and Witman, 1983] but filaments located between DMT 1 and 9 and DMT 5 and 6 could also contribute. The location of these asymmetries in the axoneme is illustrated in Fig. 1.8. Assuming sliding restriction by these cross-links, the resulting beating plane and motor activity related direction

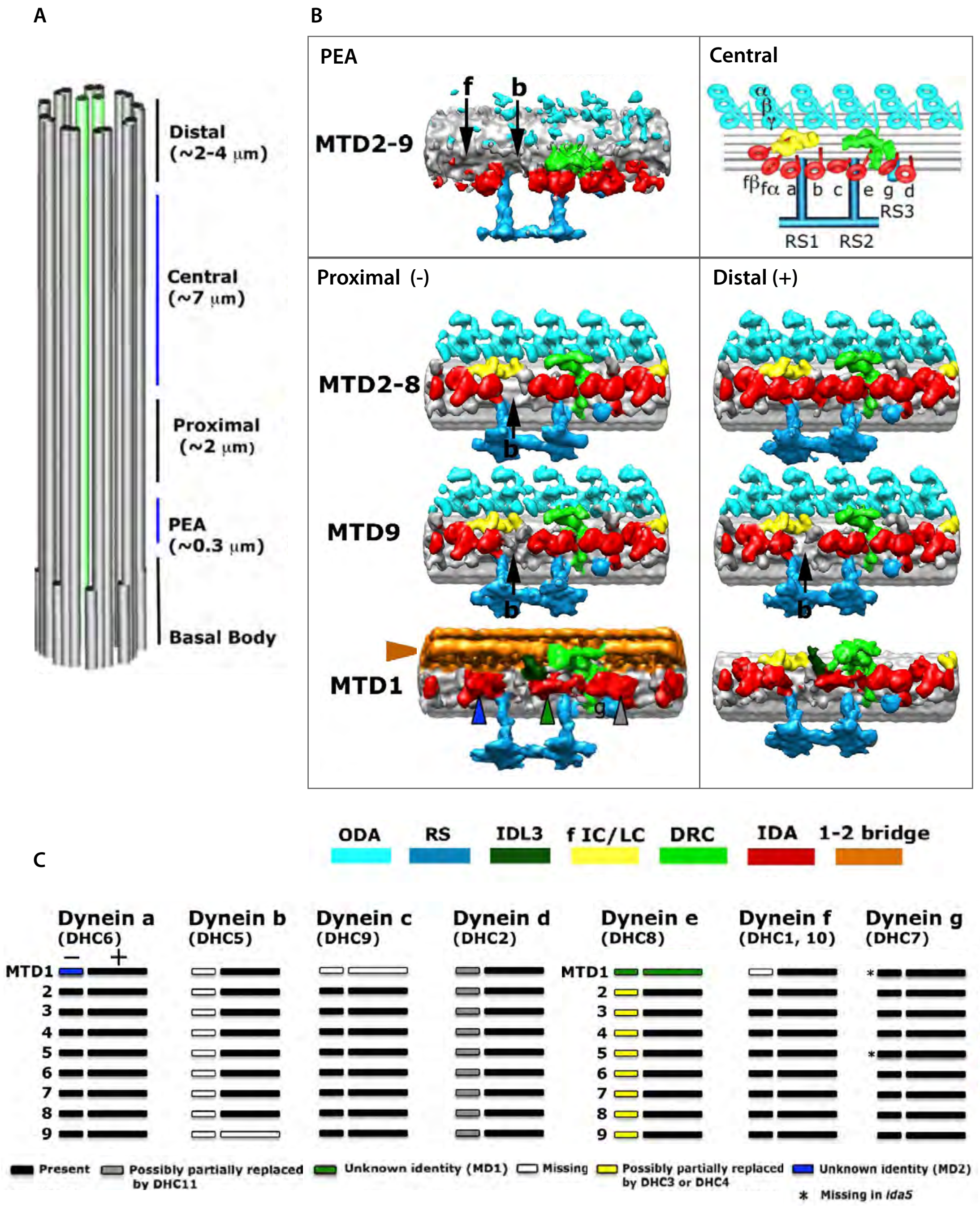

Figure 1.7: Longitudinal and radial arrangement of dyneins in the axoneme. Arrangement of dyneins in the 96-nm repeat of **Chlamydomonas** wild-type axonemes imaged by cryo-ET and evaluated using sub- tomogram averaging. **A** Axoneme cartoon with depicted sections used for averaging. The (μ) values indicate the length of the corresponding regions. **B** Densities gained from averaging over the section depicted in A. MTD defines the specific Microtubule Doublets chosen for averaging. The insert Central shows a cartoon of the general arrangement of dyneins in the central region of the axoneme. MTC1 exhibits special features depicted with colored arrows heads: (brown) the 1-2 bridge,(gray) minor dynein DHC11, (blue and green) unidentified densities. DHC4 and DHC3 is only associated to MTD2-9, distal to RS2. **C** Overview of the locations of identified dyneins on specific doublet microtubules. Adapted from [Bui et al., 2012]

of bending is depicted. The figure shows that the activity of motors between DMT 2-5 gives rise to the principle bend, which could be viewed as the breast-stroke the swimming cell uses to propel itself forward. Contributions to the bend in the opposite direction would come from DMT 6-8 and thus count responsible for the reverse bend, which would lead to the recovery-stroke.

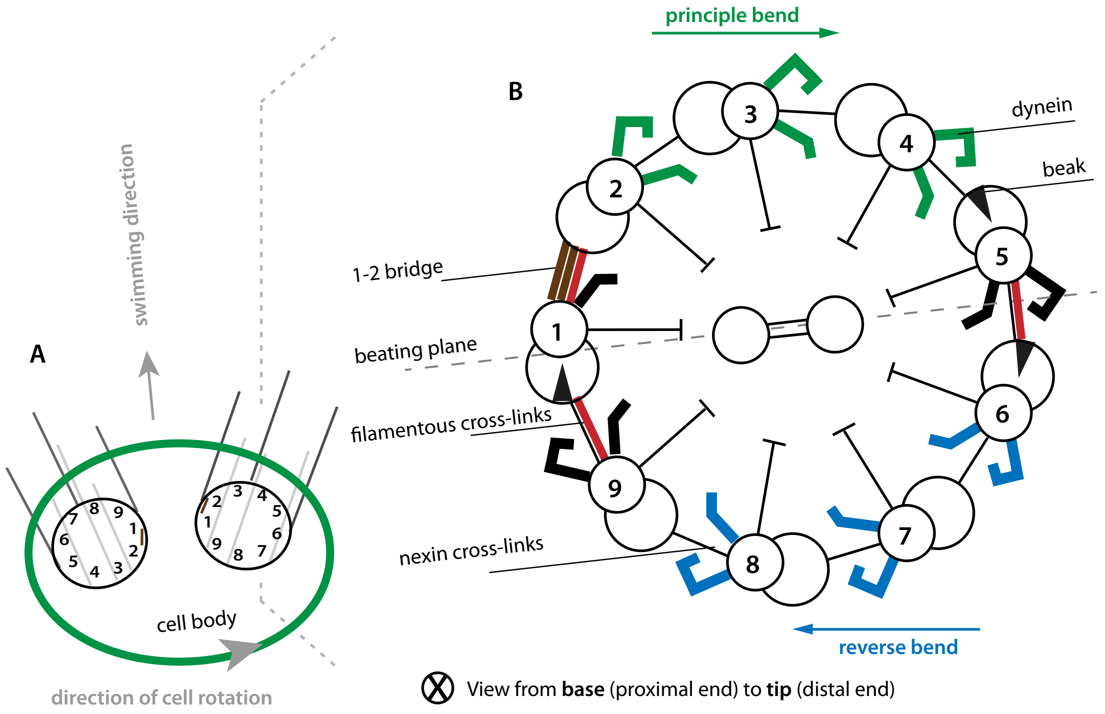

Figure 1.8: Cross-links in the axoneme. The axoneme has an asymmetric distribution of cross-links, which define the beating plane. **A** Cartoon of a swimming *Chlamydomonas* cell. The left and right flagella are the same: The left flagella is the right flagellum 180° rotated around its long axes. **B** Cartoon of the right flagellum from A. The asymmetric arrangement of internal structures is highlighted. The activity of dynein motors in the upper side of the cartoon in green (between DMT 2-5) contribute to the principle bend, the activity of dynein motors on the lower side of the cartoon in blue (between DMT 6-9) contribute to the reverse bend (recovery stroke).

Having discussed the structure and function of the mechanical elements - the microtubules and the force generating elements - the dyneins and their arrangement in the axoneme, it is now interesting to understand how both together can produce the oscillatory beat of the axoneme. This can be achieved by (1) trying to elucidate the molecular origin of the shape by comparing different mutants as discussed in Section 4.4 or by (2) by comparing waveforms gained by theoretical modeling using known axoneme properties to recorded shapes as discussed in Section 4.5.

1.4 Axonemal waveform models and mechanisms: from sliding to bending to beating

For decades scientists argue about how dynein motors produce the repetitive bends that propagate through the axoneme. Here is a general idea how beating works, probably a very simplified version of what is going on in reality:

Sliding to bending: It is well established that dynein motors are capable of sliding adjacent doublet microtubules [Summers and Gibbons, 1971] . In the axoneme this sliding is thought to be restricted by cross-links located at the basal end and along the length [Bower et al., 2013] . Sliding restriction at the base could arise from centrin or tectin fibers, that are concentrated in the stellate structure which could act as stiff shearing springs. An argument for that assumption is that partially disintegrated axonemes are still held together at the base [Aoyama and Kamiya, 2005] . Along the length nexin cross-links, structural components discussed in the Section 1.3.3 or motors themselves could restrict sliding locally. Sliding is converted into bending based on these restrictions [Lindemann et al., 2005] .

Bending to beating: Given the equal polarity of the microtubule doublets in the axoneme and the fact that all motors are statically attached to the B-tubules, motor activity on opposite sides bends the axoneme in opposite directions. Thus, to bend the axoneme, motors can only be active on one side: A simultaneous activation of motors on opposite sides would lead to a 'tug of war' situation resulting in no bending. The question that therefor arises is: What do motors sense and how is the motor action regulated? There are different ways of motor regulation that are under discussion. When sliding causes stress in the axoneme, strain is induced in various components. This strain could then trigger a mechanical or chemical switch that regulates motor activity in a sliding-displacement or curvature dependent manner. Internal stress could also lead to deformations in the axoneme, which alters doublet spacing and thus mechanically regulates motor attachment. These ideas are discussed as Curvature-, Sliding- and Geometric clutch mechanisms and are models for axoneme beating.

In the **Curvature Control** model, motor activity is directly related to the local curvature. This model has been formulated as the sliding filament model and tested in computer simulations while the results were compared to sea urchin waveforms [Brokaw, 1972a]. The model could be used to create similar waveforms although the bend initialization behavior at the base was not captured.

In the **Sliding control** model, motor regulation is proportional to the local sliding displacement. This idea has been formalized and tested with the intact bull sperm cell where a very good agreement was reported [Riedel-Kruse et al., 2007].

In the **Geometric Clutch** model, a transverse force regulates motor activity mainly by changing the inter-doublet spacing [Lindemann, 1994a]. In this model, the combination of the arrangement of the doublets and the action of the motors can act as a clutch. The idea here is that the activity of the motors is regulated by the physical separation of the dyneins from the filaments. This concept was successfully tested in computer simulations. These ideas have been further developed in the T-Force-Control model [Lindemann, 1994b].

Oscillations can be a property of multi-motor systems. While bending the axoneme in a pre-defined plane, dynein motors of one side have to work against the restoring force produced by the flexural rigidity of the elastic elements (microtubule doublets and cross-links) of the whole axonemal structure.

While the sliding displacement between adjacent doublet microtubules locally increases, the axoneme gets more bent and thus stores more elastic energy. With increasing elastic energy stored in the filaments, the likelihood for the system to exhibit its switch-like instability in increasing. This has shown to be a natural property of multi-motor systems. This concept has been proposed by C. Brokaw [Brokaw, 1975b] and studied in theoretical detail [Camalet and Jülicher, 2000]. The idea is that increasing force leads to a catastrophic detachment (force induced detachment) of motors on the load bearing side. In the flagellum, this would allow the motors on the corresponding opposite side take over and bend the structure in the other direction. This concept can lead to stable oscillations in the presence of elastic elements. A schematic of the system with motors and springs is illustrated in Fig. 1.9. In a system of symmetric motor forces, noise or the stochastic attachment of motors is needed to start the oscillations. An asymmetry of motor forces leads to a static offset of the oscillating system with respect to the steady state position of the inactive system. A system without springs will get unstable so that the oscillations are not self sustained and one group of motors wins.

To judge on the applicability of these different descriptions, they have to be compared to experimental data. Such a comparison is presented in Section 4.5 for the sliding and curvature control model applied to the isolated axoneme.

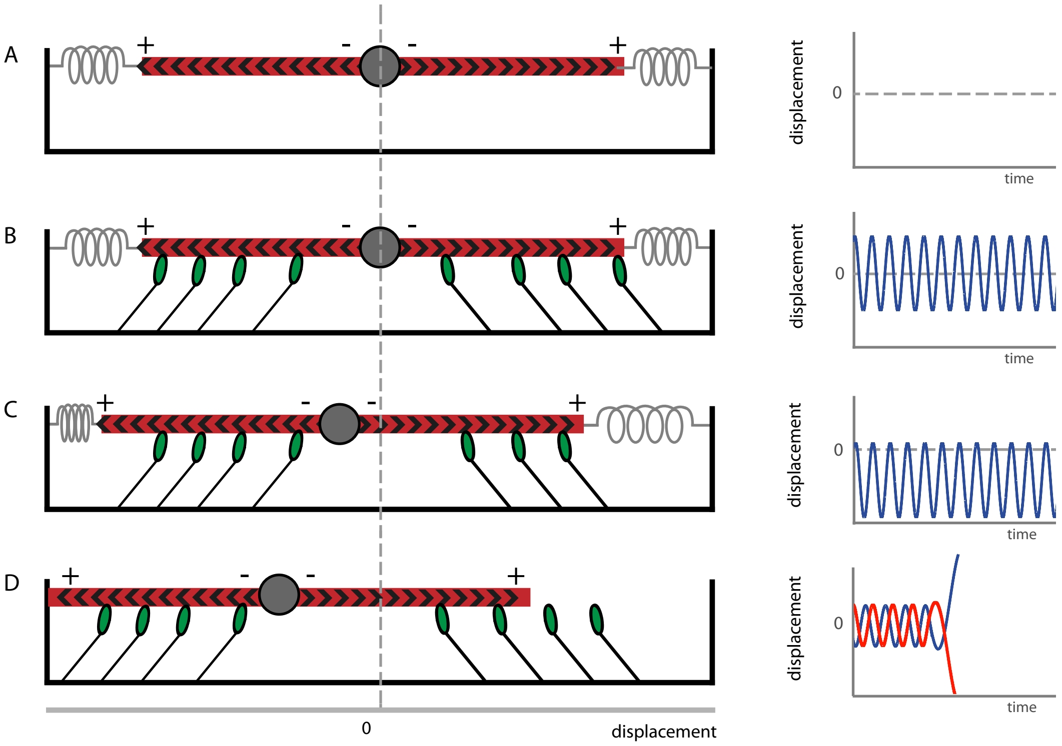

Figure 1.9: Oscillations in multi-motor systems. A system of antagonistically acting motors can exhibit stable oscillations in presence of an elastic restoring force. **A** Cartoon of two anti-parallel attached filaments held by springs of equal stiffness. **B** The action of equal number of motors leads to stable oscillations. The steady state position is 0. **C** Asymmetric motor force leads to stable oscillations around a constant offset **D** In the absence of Springs oscillations get unstable and motors on one side win the tug of war.

1.5 Geometrical representation and parameterization of the axonemal beat

In the previous sections I discussed the axonemal components and their function extensively. In the intact axoneme the concerted action of these components gives rise to repeating bending waves traveling through the axoneme that shape the flagellar waveform. The considered waveforms contain different kinds of information: Hydrodynamic information and information about the internal forces which give rise to bending. Hydrodynamic forces are balanced by the sum of internal active forces and internal passive visco-elastic forces of the flagellum. Waveforms can be presented in different ways. In some presentations specific information are lost. In the following I will show different waveform representations and introduce the concepts associated with them.

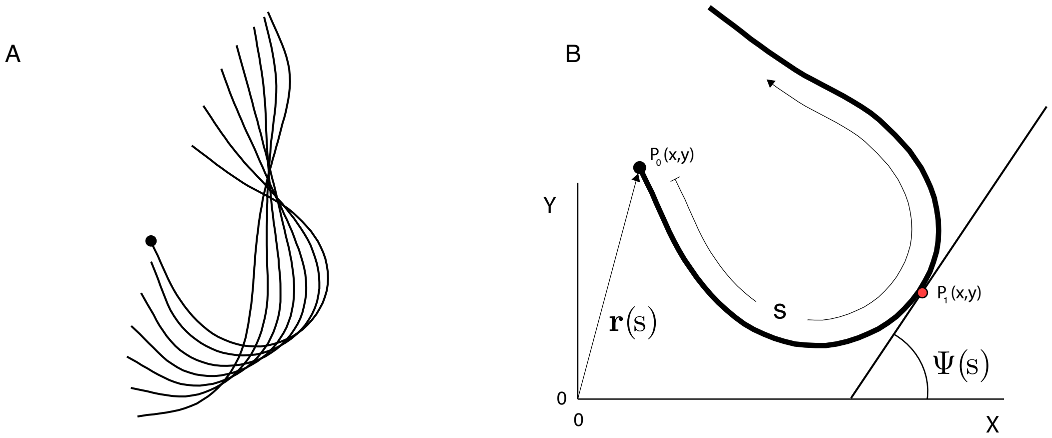

Figure 1.10: The tangent angle description of the shape. Shape parameterization by the tangent-angle with respect to a fixed frame. **A** Series of shapes of the waveform of a reactivated *Chlamydomonas* axoneme. **B** Shape with the pointing vector **r**(s) pointing to the point P_0 and the tangent angle Ψ(s) with respect to the lab frame at the point P_1.

The waveform is given by a series of shapes that change in time, see Figure 1.10 A. The shapes are observed in the image plane, a fixed coordinate system, that I will refer to as the lab frame. Thus each point on the arc-length s of the flagellum corresponds to a point in the image plane given by the **pointing vector r**(s)= $(x(s), y(s))$. Another way of looking at the shape is to parameterize it by the **tangent angle** Ψ with respect to the lab-frame, see Figure 1.10 B. This description uses an angle at every arc-length position s. Through this parameterization, the information about the trajectory of the first point is lost. The transformation from lab to axoneme frame is given by:

$$r(s) = r(0) + \int_0^s (\cos \Psi(s), \sin \Psi(s)) ds \tag{1.1}$$

with $r(0)$ being the vector pointing to the first point of the axoneme. Another commonly used way to represent shapes is by the **shear angle** $\Psi_s = \Psi(s,t) - \Psi(s = 0,t)$. This concept is based on the idea that the activity of motors slides adjacent doublets by a distance Δ. The sliding displacement between two opposing filaments in the structure is approximately proportional to the angular difference between the first and the considered point and thus relates sliding to bending. This concepts is valid up to the assumption that microtubule doublets do not slide at the first point (the basal end) of the axoneme and thus $\Delta_0 = 0$. Furthermore, it assumes that the axoneme does not undergo deformations during the beat so that the axonemal diameter a and the filament spacing is constant. Then, the internal sliding displacement Δ relates to shear angle by:

$$\Delta = \Delta_0 + \Psi_s(s)a \tag{1.2}$$

In the shear angle representation the information about the first angle is lost, thus beat amplitude and wavelength can not be reconstructed from that representation.
The shape can also be represented by **curvature** $C(s,t) = \partial\psi(s,t)/\partial s$, see Figure 1.11 C. Curvature shows how bent the axonemal structure is locally and thus represents a combination of material properties of the axoneme and local bending forces.

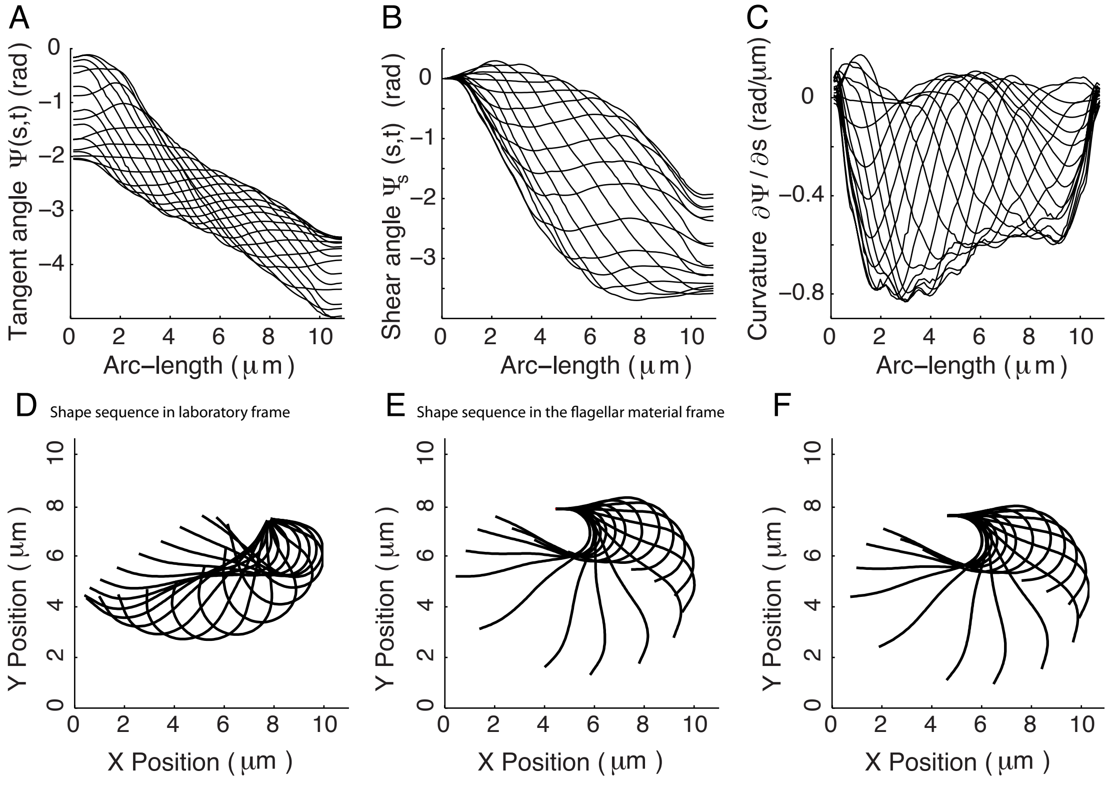

Figure 1.11: Geometrical representations of the flagellar beat. Representations of the waveform of a *Chlamydomonas* axoneme. **A** Tangent angle representation with **D** the corresponding reconstructed shape in laboratory frame. **B** Shear-angle representation $\Psi_s = \Psi(s = L,t) - \Psi(s = 0,t)$ with **E** the corresponding reconstructed shape in the material frame of the flagellum.**D** Curvature representation $C(s,t) = \partial\psi/\partial s$ with F the corresponding reconstructed shape.

The constant curvature model: Shape parameterization in time domain

To compare waveforms of different mutants and test the applicability of beating models one needs to parameterize the waveform by a minimal set of shape parameters. The parameterization that is still commonly used was presented by Charles Brokaw as the constant curvature model [Brokaw and Luck, 2005]. This model simplifies the waveform in the following way.

Parameters of the constant curvature model: The model uses the shear angle description of the beat as presented in Figure 1.11 B and breaks each shape into a principle and a reverse bend component each with a constant curvature κ_P and κ_R as depicted in Figure 1.12 C/D. In the model, both curvatures have a propagation velocity, the shear rate V_P and V_R. Together with a time constant τ, which characterizes the time for the initialization of the bending in the principle relative to the reverse bend the *Chlamydomonas* waveform can be approximated by 5 parameters using the constant curvature model. Typical parameters for the WT cell are given in Figure 1.12 .

Problems with the constant curvature model: The main problem for the constant-curvature model is that it is a discontinuous description of an oscillation. Comparing it to an analytical solution of a model for the beat is therefore difficult. The model does not capture the arc-length dependence of the shape parameters which might be important for a detailed comparison of a model to experimental data.

The constant curvature model shows that the *Chlamydomonas* beat is well approximated by 2 propagating constant curvatures which have a fixed time delay. To compare experimental data to theoretical models it would be useful to have a continuous description of the *Chlamydomonas* beat. A continuous waveform description for the symmetric beat of bull sperm that using Fourier decomposition methods has been presented [Riedel-Kruse et al., 2007]. The Fourier decomposition of the *Chlamydomonas* beat is presented in Section 4.2.1.

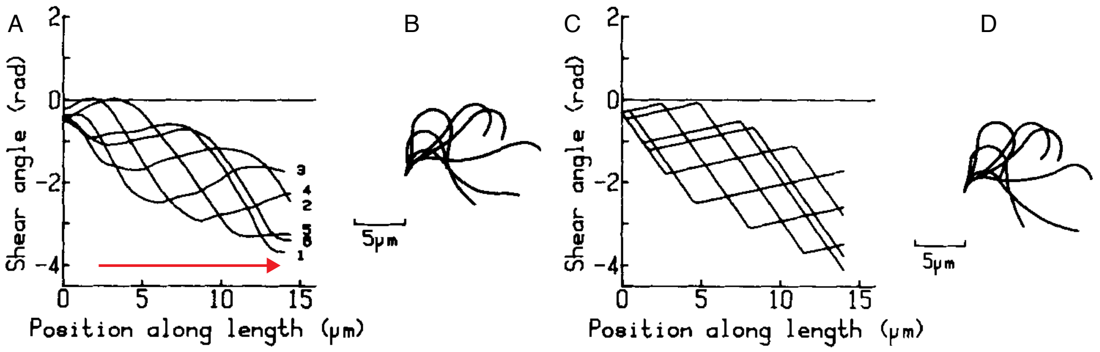

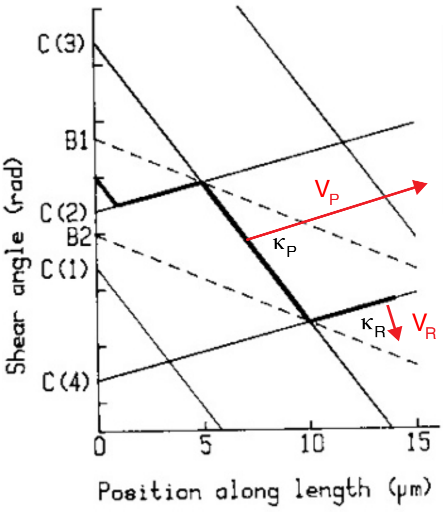

F

Typical WT parameters for the constant curvature model

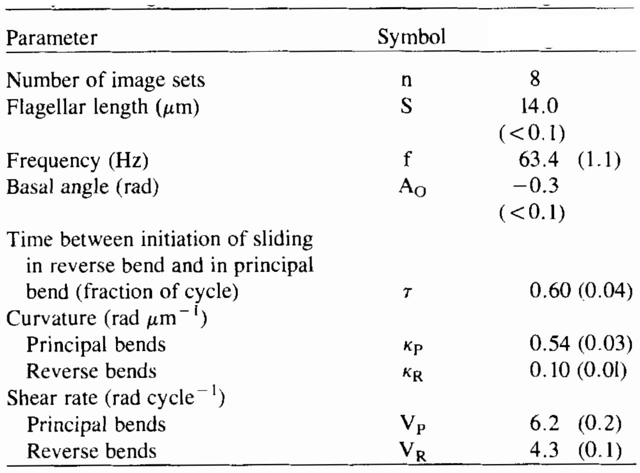

Parameter	Symbol	
Number of image sets	n	8
Flagellar length (μm)	S	14.0 (<0.1)
Frequency (Hz)	f	63.4 (1.1)
Basal angle (rad)	A_O	−0.3 (<0.1)
Time between initiation of sliding in reverse bend and in principal bend (fraction of cycle)	τ	0.60 (0.04)
Curvature (rad μm^{-1})		
Principal bends	κ_P	0.54 (0.03)
Reverse bends	κ_R	0.10 (0.01)
Shear rate (rad $cycle^{-1}$)		
Principal bends	V_P	6.2 (0.2)
Reverse bends	V_R	4.3 (0.1)

G

Alternative parameters for the constant curvature model

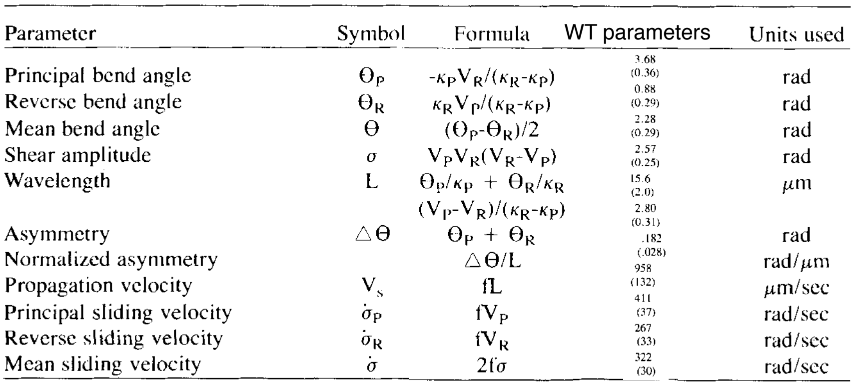

Parameter	Symbol	Formula	WT parameters	Units used
Principal bend angle	Θ_P	$-\kappa_P V_R/(\kappa_R-\kappa_P)$	3.68 (0.36)	rad
Reverse bend angle	Θ_R	$\kappa_R V_P/(\kappa_R-\kappa_P)$	0.88 (0.29)	rad
Mean bend angle	Θ	$(\Theta_P-\Theta_R)/2$	2.28 (0.29)	rad
Shear amplitude	σ	$V_P V_R(V_R-V_P)$	2.57 (0.25)	rad
Wavelength	L	$\Theta_P/\kappa_P + \Theta_R/\kappa_R$	15.6 (2.0)	μm
		$(V_P-V_R)/(\kappa_R-\kappa_P)$		
Asymmetry	$\triangle\Theta$	$\Theta_P + \Theta_R$	2.80 (0.31)	rad
Normalized asymmetry		$\triangle\Theta/L$	.182 (.028)	rad/μm
Propagation velocity	V_s	fL	958 (132)	μm/sec
Principal sliding velocity	$\dot{\sigma}_P$	fV_P	411 (37)	rad/sec
Reverse sliding velocity	$\dot{\sigma}_R$	fV_R	267 (33)	rad/sec
Mean sliding velocity	$\dot{\sigma}$	$2f\sigma$	322 (30)	rad/sec

Figure 1.12: The constant curvature model for WT bending patterns. Time-domain waveform parameterization using a model assuming the propagation of constant curvature proposed by Charles Brokaw, [Brokaw and Luck, 2005]. **A** Shear angle representation of the beat. The black numbers depict the order of shapes in time. The red arrow shows the direction of wave propagation. **B** Flagella shapes corresponding to A. **C** Shear angle approximation of A using the constant curvature model. **D** Shapes reconstructed form the parameters gained from the constant curvature model. **E** Illustration of the constant-curvature model: κ_P and κ_R depict the curvature of the principle and reversed bend. The propagation direction and the corresponding propagation velocities V_P and V_R of the corresponding curvatures is depicted by a red arrow. C(2,4) are hereby the curvatures of the reverse, C(1,3) are the curvature of the principle bend. The shear-amplitude is equal to the distance between B1 and B2 here 1.71 rad. **F** Parameters of the beat of a typical WT cell gained by the constant curvature model. **G** Alternative parameters gained from the minimal set of parameters in panel F with WT valued calculated from F. Values in parenthesis are standard deviations. Figures are adopted from [Brokaw and Luck, 2005] and [Brokaw, 1983, The constant curvature model for flagellar bending.]

Chapter 2

Questions addressed in this thesis

In this thesis I investigate the isolated and reactivated *Chlamydomonas* axoneme as an experimental model for the flagellar beat. To do this I ask the following questions:

How do I image the beating axoneme with high spatial and temporal resolution? What localization precision do I gain from shape tracking?

What shape parameterization do I use to gain a minimal set of shape parameters and a continuous description of the waveform?

Using methods for imaging and shape description I characterize the isolated axoneme system by asking:

Is the beat of the isolated axoneme different from the beat of the cell-attached flagellum?

What is the direction of wave propagation for the isolated axoneme?

How can we characterize the shape difference between the symmetric beat of sperm cells and the asymmetric beat of the *Chlamydomonas* flagellum?

How does the beat-shape relate to the swimming behavior of the axoneme?

Can we identify the molecular origin of the waveform difference between sperm and *Chlamydomonas* cell?

Which out of several theoretical description of flagellar oscillations, representing different paradigms of motor control, describes the Chlamydomonas beat best?

Chapter 3

Material and Methods

This chapter summarizes all methods used in this thesis. It starts with methods that describe the handling of *Chlamydomonas* cells in the lab, proceeds with the isolation and reactivation of flagella and details image analysis and tracking procedures. The principles of data evaluation methods are also outlined at the end of this chapter. Most of the cell related methods I present here I also published in a Methods in Enzymology volume [Alper et al., 2012].

3.1 Chlamydomonas cells: Axoneme preparation and motility assays

3.1.1 Culturing of Chlamydomonas reinhardtii cells

Preparation of growth medium: We prepare agar-plates and liquid cultures using Tris Acetate Phosphate (TAP) medium [Gorman and Levine, 1965] with 4 times the phosphate concentration used by Gorman and Levine (TAP+P). We have found that the increased phosphate content of TAP+P supports Chlamydomonas growth for a longer time than in TAP without the extra phosphate. Thus, a higher density of viable cells can be reached. We mix TAP+P following the protocol given in Table: 3.3 using pre-prepared stocks of Salt Solution, Potassium Phosphate Solution, and Hutner's Trace Elements see protocols Table: 3.1/ 3.2. All reagents are purchased from Sigma-Aldrich, unless otherwise stated.

Table 3.1: Stock solutions for Chlamydomonas culture medium 1L: All stock solutions are prepared ahead of use, autoclaved for 20 min at 121 °C and stored at 4 °C.

Salt Solution: 1L

Compound	Amount (g)	Final concentration (mM)
NH_4Cl	15.0	280
$MgSO_4 \cdot 7H_2O$	4.0	16.2
$CaCl_2 \cdot 2H_2O$	2.0	13.6

Add distilled-deionized water (ddH2O) to 1 L

Potassium Phosphate Solution: 1 L

Compound	Amount (g)	Final concentration (mM)
K_2HPO_4	288.0	1.65
$KH_2PO_4 \cdot 7H_2O$	144.0	1.06

Add ddH2O to 1 L. Note that this solution should be at pH 7.4 as mixed.

Table 3.2: Components for Huttner's trace elements 1 L The trace elements are prepared according to a protocol based on [Hutner, 1950, Hutner et al., 1950].

Compound	Amount (g)	Water (ml)	Final concentration (mM)
KOH	20.0	100	~300(based on titration)
$ZnSO_4 \cdot 7H_2O$	2.0	100	76
H_3BO_3	11.40	200	184
$MnCl_2 \cdot 4H_2O$	5.06	50	25
$CoCl_2 \cdot 6H_2O$	1.61	50	6.8
$CuSO_4 \cdot 5H_2O$	1.57	50	6.3
$(NH_4)6Mo_7O_24 \cdot 4H_2O$	1.10	50	0.9
$\mathrm{EDTA, di - sodiumsalt}$	50.0	250	134
$FeSO_4 \cdot 7H_2O$	4.99	50	18

Add ddH_2O to 1 L. Note that this solution should be at pH 7.4 as mixed. It is a good practice to use pH paper to do the pH adjustments described in the protocol.

1.Degas 50 mL of ddH_2O under vacuum for use in step 6.
2.Dissolve the first 7 chemicals in ddH_2O as indicated in the table. Note that H_3BO_3 may need to be heated slightly to get it to dissolve.
3.Warm the KOH to 70 °C.
4.Boil 250 mL of ddH_2O and add 50 g EDTA.
5.Combine the solutions prepared in step 2 in a large flask and boil.
6.While the combined solution is warming, dissolve the $FeSO_4 \cdot 7H_2O$ in 50 mL of ddH_2O degassed in step 1.
7.Add the $FeSO_4 \cdot 7H_2O$ solution to the combined solution in the boiling flask. Keep bubbles to a minimum to prevent oxidation. Note that addition of the $FeSO_4 \cdot 7H_2O$ solution changes the color to yellow-brown.
8.Boil the combined solution until it gets cloudy.
9.Add the EDTA solution prepared in step 4. The mixture should turn dark green and remain clear.
10.Decant the solution into a 2 L bottle and allow it to cool to 70 °C. While the temperature is at 70 °C, titrate the solution to pH 6.5 - 6.6 by adding 80 - 90 mL of the 70 °C 20 % KOH solution warming since step 3 with a glass pipet. Note that the solution should still be clear green. A brown precipitate forms if the solution gets to pH 6.7 - 6.8.
11. Add dd $_{H_2O}$ to the solution up to 1 L total volume. Note that a small amount of brown precipitate may form after adding the water.

12.Stopper the bottle with a cotton plug and let it stand for 1-2 weeks, shaking it once a day, until the solution turns purple and leaves a rust-brown precipitate. Note that if no precipitate forms, adjust the pH to 6.5 using either KOH or HCl, as needed.
13.Filter the solution with two layers of Whatman 1 filter paper. Repeat the filtration, if necessary, until the solution is clear.

Table 3.3: Preparation of TAP+P medium from stock solutions: 1L

Compound	Amount
TRIS	2.42 g
Salt Solution	25 mL
Potassium Phosphate Solution	1.5 mL
Hutner's Trace Elements	1.0 mL
Glacial acetic acid	~1.8 mL

1.Combine the first four chemicals and stocks listed in the table. Add ddH2O to 1 L.
2.Titrate to pH 7.0 with glacial acetic acid. The initial pH will be 8 - 9.
3.Mix vigorously and the solution will turn clear.
4.Autoclave TAP+P for 20 min at 121 °C.

The final TAP+P - buffer contains: 20 mM TRIS, 30 mM acetate, 7.7 mM Cl^-, 7 mM NH_3^+, 6.5 mM K^+, 4 mM PO_4^-, 0.4 mM Mg^{2+}, 0.4 mM SO_4^{2-}, 0.35 mM Ca^{2+}, and traces of the elements included in Hutner's Trace Elements.

Growing cells: *Chlamydomonas* strains were grown and stored on 6 cm agar plates [Witman, 1986] . To grow the quantities of cells necessary to do biophysical measurements with purified components, liquid culturing of *Chlamydomonas* cells was used [King et al., 1986]. For liquid culturing, we set up a specific 3 port valve system that allows to aerate the culture and to take samples without introducing contaminants. A cartoon of this system is shown in Figure 3.1.

Protocol for making Agar plates:
1.Add 1.5% (w/v) agar to TAP+P and autoclave for 20 min at 121 °C and store sealed in 300 mL aliquots.
2.Melt small volumes (300 mL) of agar containing TAP+P in the microwave and pour plates in a cell culture hood. To avoid condensation on the lid of the plates, keep the plates unsealed in the hood while they cool to room temperature.
3.Seal plates with Parafilm M (Pechiney Plastic Packaging) and store at room temperature until used.
4.In the cell culture hood, plate cells in thin stripes 5 mm apart using a standard inoculation loop.
5.Seal with Parafilm, and keep at room temperature (22-24 °C) under the illumination of a 15 W fluorescent bulb. Re-plate cells every 2-3 months.

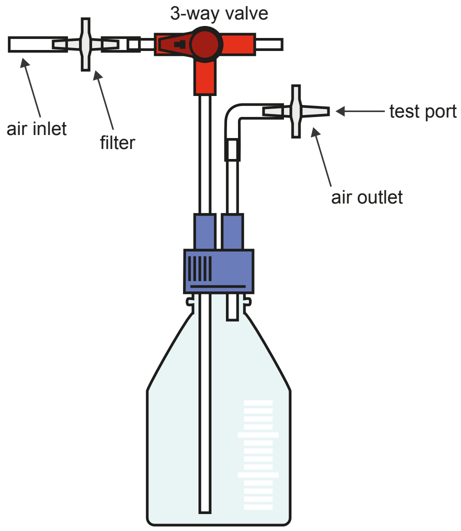

Figure 3.1: Cartoon of Chlamydomonas culture system. Culture bottles enable extraction of samples without introducing contaminants. The culture medium is constantly mixed by the flow of air, which is supplied through the air inlet via a 0.22 μm filter and glass tubing directly into the culture. There is a switchable 3-way valve between the air inlet and glass tube with a test port. The air outlet is sealed with another filter. To monitor the growth of the culture without any contamination, extract a sample through the test port by attaching a syringe to the test port, turning the valve to stop the airflow, and sucking up a sample of cell culture into a syringe. By closing the valve, airflow is re-established, and the apparatus prevents back-flow of the culture, which maintains it's sterility. Cartoon is a courtesy of Joshua Alper [Alper et al., 2012].

Protocol for setting up a Liquid culture:

1.Inoculate a pre-culture (300 mL) of growth medium with a pea-sized volume of cells scraped off an agar plate in the cell culture hood. We use glass bottles (Fischer Scientific, GL45, 0.5, 1, 2, or 10 L) equipped with 2-port lids (Figure 2).

2.Place the bottles between two 1.20 m long, 75 W fluorescent bulbs, which are mounted at a height of 15 cm above the bench and 15 cm from the bottles. We keep the cell culturing apparatus in an air conditioned room at a constant temperature of 22 °C and use a fan to keep the temperature of the growth medium constant at 24 °C during continuous illumination.

3.Bubble air through the culture to ensure proper mixing. Ensure the bubbling is not too vigorously or the culture will evaporate. This balance is particularly important with small ($<$ 1 L) volumes. An air flow rate of 2 L/min is sufficient in large culture bottles ($>$ 2 L), and 0.3 L/min is sufficient for pre-culture bottles (0.5 L).

4.Monitor the cell density by extracting a sample from the culture and measuring the absorbance of the sample at 750 nm (A750) using an Agilent 8453 spectrophotometer. The extinction coefficient of wild type cells is $4.7 \pm 0.5 \times 10^6$ cells/(OD·mL·cm). Note that we use A750 because it is proportional to the number of cells. This takes advantage of the light scattering property of cells at 750 nm as opposed to using the absorbance peaks, which are proportional to the amount of chlorophyll [Sager and Granick, 1953] and may not be directly proportional to the number of cells. We calibrated this spectrophotometric method with an Invitrogen Countess Automated Cell Counter and verified the calibration with a high-precision blood counting chamber (Bad Blankenburg, GDR) as shown in Figure 3.2.

5.Allow cells to grow to the late log-phase, up to a density of $3 - 7 \times 10^6$ cells/mL. This is reached in 2 - 2.5 days (Figure 3 B). As cells metabolize the acetate during growth, the pH increases.

6.Inoculate a growth culture by diluting the pre-culture in a larger volume of TAP+P to about 2×10^5 cells/mL in the cell culture hood.

7.Allow cells to grow up to a density of $3 - 7 \times 10^6$ cells/mL.

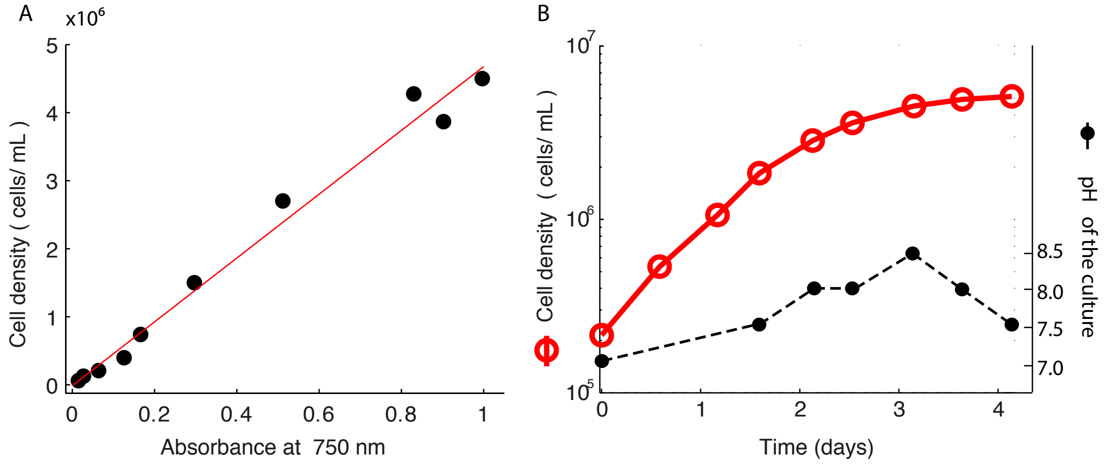

Figure 3.2: Growth curve of Chlamydomonas cells. *Chlamydomonas* wt cells have been grown in liquid culture **A** Calibration curve for the measurement of cell density using optical density at 750 nm (see text: liquid culture (4)). The calibration constant of $4.7 \pm 0.5 \times 10^6$ cells/(OD·mL·cm) (slope ± 95% confidence interval of the least square fit) is used to determine the cell density of a Chlamydomonas culture. **B** Typical growth curve of wild-type *Chlamydomonas* cells in TAP+P showing both the cell density (red data points, left y-axis) and pH of the culture (black data points, right y-axis.

I use total number of 10^9 cells to purify axonemes for reactivation experiments that have not been growing for longer than 2.5 days.

3.1.2 Isolation, demembranation and storage of axonemes

Axonemes were purified by deflagellating *Chlamydomonas* cells using the dibucaine procedure and demembranating the flagella using nonionic detergent [Witman, 1986]. In the following, I present protocols used to perform these procedures. Buffers and stock solutions should be made well ahead of time and stored at 4°C.

Table 3.4: Axoneme Buffer Solutions

Buffer	HEPES (mM)	MgSO2 (mM)	DTT* (mM)	EGTA (mM)	K-Acetate (mM)	PEG (%)	Sucrose (%)
HE	10	-	-	1	-	-	-
HMDS-4	30	5	1	-	-	-	4
HMDS-25	30	5	1	1	-	-	25
HMDEK	30	5	1	1	50	-	-
HMDEKP	30	5	1	1	50	1	-

Titrate these buffers to pH 7.4 with KOH. * Add just before use.

Stock solutions:
Dibucaine-HCl :(25 mM in ddH_2O, pH 5.0 using HCl), a local anesthetic, which is used to induce deflagellation. Store at 4 °C.
IGEPAL CA-630: (dilute 10% in ddH_2O), a nonionic detergent, which is used to demembranate the axonemes. Store at 4 °C. We use IGEPAL as a substitute for Nonidet P-40 (BDH Chemicals, Ltd., Poole, England), used in earlier assays (Bessen et al., 1980) but no longer available.
Pefabloc SC:(100 mM Pefabloc SC in ddH_2O), a protease inhibitor. Use at a final concentration of 0.2 mM. Store at 4 °C.

Protocol: Cell harvesting and deflagellation
1. Prior to the preparation, measure the density of the culture and check for flagellation under the microscope. If less than 50% of the cells are flagellated, induce flagellation by pelleting the cells by centrifugation at 800 × g for 5 min and re-suspending them in ddH_2O. Cells are then put back into the growth conditions as described above and allowed to grow for 90 min to ensure the complete outgrowth of the axoneme [Lefebvre et al., 1978].
2. Centrifuge flagellated cells at 800 × g (for 10^9 cells: pellet cells in 250 mL tubes for 5 min. Use a total of 10^9 cells.
3. Wash cells by re-suspending in HE buffer and centrifuging cells at 800 × g for 5 min.
4. Re-suspend cells in 10 mL of ice cold HMDS-4, add Pefabloc, and work on ice from this point on.
5. Deflagellate cells by adding 2 mL of dibucaine solution to each tube containing 10 mL of resuspended cells and rapidly pipet the solution up and down until cells are deflagellated. This step takes about 1.5 min. Longer incubation leads to cell death, release of proteases and decreased purity of the axoneme sample. Monitor deflagellation under the microscope.
6. Add 28 ml of ice cold HMDES-4 + Pefabloc to each tube containing the deflagellated cells
7. Distribute 35 mL of the supernatant into 50 mL conical polycarbonate tubes. Underlay each with 10 mL cold HMDES-25 + Pefabloc solution using a 10 mL pipet mounted on a 10 mL plastic syringe.
8. Centrifuge at 2400 × g using a swinging bucket rotor at 4 °C. Set the acceleration and deceleration low so the cushion does not mix with the cell suspension. 9. Collect the upper layer and ensure no cell bodies remain in this supernatant. Repeat steps 8 and 9 if necessary.
10. Centrifuge the supernatant at 31,000 × g for 20 min at 4 °C in 50 mL round-bottom polycarbonate tubes. Pour off and discard the supernatant. The pellet should be white-yellowish at that point since it contains isolated flagella.

The isolated flagella may be kept at 4 °C over night.

Protocol: Demembranation and isolation of axonemes
Axonemes should be handled gently during the re-suspension steps: avoid foaming and minimize the mechanical damage by pipetting slowly or using a large tip. In general, the exposure of axonemes to surfaces should be minimized during the isolation procedure.

1. To remove flagellar membranes, re-suspend the isolated flagella in 5 mL of ice-cold

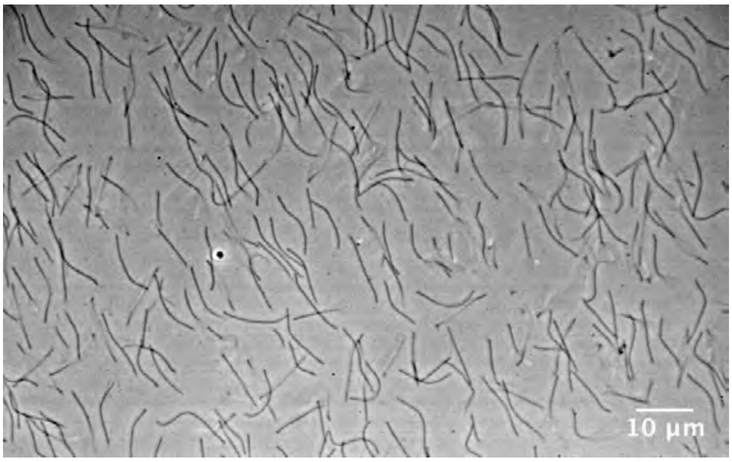

Figure 3.3: Isolated and demembranated Chlamydomonas axonemes. Phase-contrast micro-graph of isolated and demembranated axonemes from the *Chlamydomonas* mutant ODA1, non-specifically absorbed to a glass slide.

HMDEK + 1% IGEPAL+Pefabloc.

2. Centrifuge the axonemes at 31,000 × g in 50 mL round bottom polycarbonate tubes for 20 min at 4°C and discard the supernatant.

3. Re-suspend the axonemes in 500μL ice-cold HMDEKP and repeat steps 2 and 3.

4. Re-suspend in 100 μL HMDEKP+Pefabloc and use axonemes for reactivation assays. A typical axoneme preparation is shown in Figure 3.3.

Storage of Axonemes:
After the purification, axonemes can be resuspended in HMDEKP containing 10 - 30% saturated sucrose or glycerol -80°C for at least 2 years. In all following studies 30% saturated sucrose was used. After thawing in a room temperature water bath, axonemes can be reactivated and exhibit waveforms indistinguishable from those that were not frozen. In the presence of protease inhibitors, purified axonemes can also be kept in the cold room and used for 2 days.

3.1.3 Reactivation of axonemes in controlled conditions

All experiments described in the following sections were carried out in flow chambers made from easy-cleaned cover glasses (Corning, No. $1\frac{1}{2}$, size: 18 × 18 mm, thickness: 0.16 to 0.19 mm) and microscopy slides (Fisher Scientific, 3" × 1" × 1mm), which were cleaned by the easy clean procedure prior to use.

Protocol: "Easy-clean" slides and coverslips
1. Place cover-glasses and microscopy slides in holders to facilitate the handling.
2. Place holders in a glass-container, and cover the glass with detergent (Mucasol).
3. Sonicate in a bath for 15 minutes.
4. Rinse the glass with deionized water.
5. Cover the glass with ethanol and sonicate in a bath for 15 minutes.
6. Rinse the glass with deionized water.
7. Rinse the glass with ddH_2O.
8. Dry the glass with either pressurized air or nitrogen and store in an air-tight container.

Building the flow-chamber Flow chambers are built using ”easy-cleaned” glass and double sided-sticky tape and prepared in the following steps:

Cut double sided sticky tape (3M) into 3 mm thick stripes. Use tweezers to place the tape strips on a microscope slide 3 mm apart. Close the chambers by firmly attaching a 18× 18 mm cover-slip to the tape. The tape produces a 100 μm space between the two glass surfaces, which leads to an approximate chamber volume of 5 μL.

Protocol: Standard reactivation conditions for isolated-Axonemes:
Reactivation of isolated axonemes has been describes in previous studies [Bessen et al., 1980, Hyams and Borisy, 1975, Kamiya, 2009]. I reactivate isolated axonemes in the following steps:

1. Prepare a flow chamber as described previously.
2. Incubate the flow chamber with a 2 mg/ml casein solution (Sigma, C7078) in HMEKP for 10 minutes. Casein effectively prevents demembranated axonemes from sticking to the chamber surfaces and allows one to wash out nearly 100% of the introduced axonemes.
3. Mix 1-2 μL of demembranated axonemes with 20 μL HMDEKP + 1 mM ATP and perfuse the solution into the flow chamber.
4. Seal the chamber using Valap to prevent evaporation and minimize flows (optional).
5. Control the sample temperature using a objective heater (Chromaphore, Oberhausen, Germany). If not stated otherwise the temperature was kept constant at 24 °C, which was at least 2 °C above the ambient temperature.
5. Observe axoneme reactivation on the lower surface of the chamber. For WT axonemes, I usually find >80 % of the axonemes to be reactivated.

This is what I will refer to as the **standard reactivation conditions.** In experiments where ATP concentration was a parameter, the concentration was verified using the absorbance at 280 nm. During the assay, the ATP concentration was kept constant using an ATP-regenerating system composed of creatine kinase (1-10 units/ml) and creatine phosphate (6 mM). This is especially useful for ATP concentrations below 100 μM. The usage of the ATP-regenerating system had no detectable impact on the observed waveforms. In my assays a 1:10 to 1:20 dilution of the purified axonemes usually results in a density where single, non interacting axonemes can be observed. Furthermore, I find that more diluted axonemes reactivate poorly.

3.1.4 Axoneme gliding assay using kinesin 1

In a gliding assay purified molecular motors are attached to a surface and filaments are introduced. Unlike in the cell, where motors work along filaments here filaments are propelled over the surface by the concerted action of motors. In general, gliding motility assay can be used to probe the molecular properties and behavior of single and groups of molecular motors [Alper et al., 2013, Howard et al., 1989, Leduc et al., 2007]. This section details the steps to perform a kinesin 1 gliding assay with purified *Chlamydomonas* axonemes.

Prepare buffer solutions:

Table 3.5: BRB80 1x

Concentration [mM]	Substance
80	Pipes
1	$MgCl_2$
1	EGTA

Use adjust to pH 6.9 using KOH.

Table 3.6: Kinesin motility buffer

Volume [μL]	Reagent	[Stock]	[Final]
180.4	BRB80	1x	1x
4	D-glucose	2M	40 mM
4	glucose oxidase	2 mg/mL	0.04 mg/mL
4	catalase	0.8 mg/mL	0.0016 mg/mL
2	ATP	100 mM	1 mM
2	DDT	100 mM	1 mM
1.6	Vanadate	10 mM	80 μM
2*	Taxol (in DMSO)	1 mM	10 μM
200	Final Volume		

* Only use Taxol if working with Taxol stabilized filaments.

Kinesin gliding assay:
1. Prepare a flow chamber using double sided sticky tape as described 2. Block the surface using a 1 mg/mL Casein solution in BRB80 for 5 min.
3. Introduce kinesin 1 motor (Full length protein from Drosophila) 0.004 μg/mL in kinesin motility buffer for 5 min.
4. Introduce purified axonemes in kinesin-motility buffer.
5. Observe gliding using dark-field or phase contrast-microscopy.

In Section 4.1.2 , I perform a gliding assay using polarity marked axonemes. Please find the details for microtubule polymerization there.

3.2 Imaging and image processing

In this chapter I describe how I image *Chlamydomonas* cells and reactivated axonemes. I also describe how I use image analysis to precisely determine the shape of the flagella and axonemes and comment on the accuracy of the used tracking algorithms. Finally, I introduce a method I developed for the analysis of beat frequencies in a standard reactivation assay.

3.2.1 High-speed imaging of the flagella and axonemes

Microscope: I imaged reactivated axonemes and flagella on a Zeiss Axiovert 100 TV inverted microscope using phase-contrast or dark-field microscopy. Phase-contrast was set up using a Zeiss 63 × Plan-Apochromat NA1.4 PH3 oil lens in combination with a Zeiss oil phase-contrast condenser NA 1.4 and a 1.6× Optovar lens and was used for imaging flagella on cells as well as isolated axonemes. Dark-field was set up using a Zeiss 100× Plan-Neofluar NA 0.7-1.3 oil iris lens in combination with a Zeiss cardioid oil dark-field condenser NA1.4. The specimen was illuminated using a 100 W tungsten lamp for phase-contrast and an e-beam driven luminescent light pipe (Lumencor, Beaverton, USA, white light mode 200 mW per color, ~1 W total light output) for dark-field.

Camera: High-speed imaging I performed using the CMOS-high-speed camera (EoSens, CL) with a resolution of 1280 ×1024 pixels and a pixel-size of 14 × 14 $\mu\mathrm{m}^2$, that was mounted to the bottom port of the microscope. The camera is equipped with a dual-camera link, which allows for data streaming into the computer RAM at rates of 700 MB/s (equivalent to 500 fps at full-frame resolution, Images are in 8 bit - 256 gray levels). I used a Dell T-5000 workstation computer equipped with a NI PCIe-1429 image acquisition card controlled by home made LabView software to acquired movies. Movies of 3 s at a frame rate of 1000 fps with an exposure time of 0.5 - 1 ms on a field of view of 400-600 pixels^2 can be handled by the system and saved in 15-20 s. These are the standard imaging conditions used in the following studies. Using this camera, the effective pixel size was: (1) for a 63 × lens, Optovar(1/1.6) (222, 138.8) nm/pixel and (2) for a 100 × lens, Optovar(1/1.6) (140, 87.5) nm/pixel. For frequency measurements, a stable acquisition rate is crucial that only can by verified by an image time-stamp. Since direct times-stamping in the sub-ms range does not work with the computer clock I was using a alternative frame counting method: The internal camera frame counter counts the camera exposures and encodes the number in the intensity information in 4 selected pixels on the chip see Figure 3.4 A.

The comparison of the number of taken images to the number of saved images I use as a verification for the successful frame transfer. To test the acquisition trigger, I recorded image time-series of the intensity of a pulsed LED. The LED (Thorlabs, M625L2) was TTL triggered using a function generator (Arbitrary, AFG3102) at a rate of (200 Hz). The input frequency could be recovered from the movie Figure 3.4 B(ii) verifying the preservation of frequency information in the recorded time series.

Sampling in space and time. When recording images I want to capture the dynamics of the observed process so I want a sufficient temporal resolution. I also want

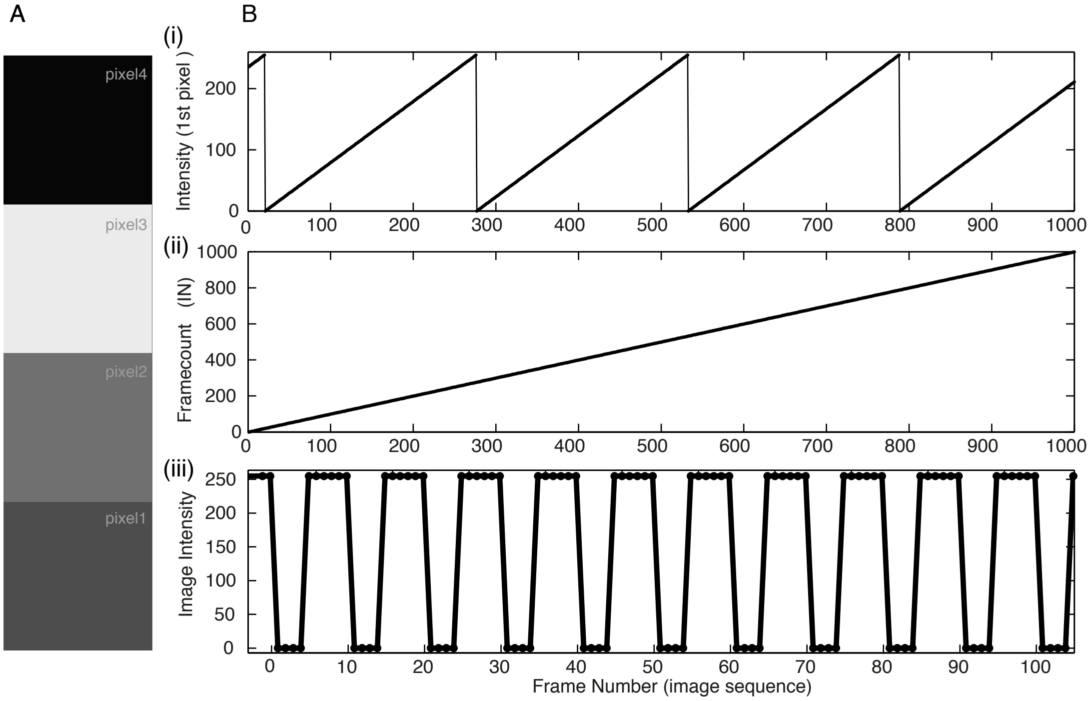

Figure 3.4: Frame counter in EoSens CI-Camera. A frame counter counts the pulses that trigger image acquisition, encodes this number in pixel gray values using 4 image pixels and writes it into each image. Comparing this number to the actual frame number elucidates missing frames. **A** Example of the 4 encoding pixels. Since the image is a 8bit image (256 gray levels) the Image-Number (IN) is given by: $IN = \sum_{i=1}^{4} pixel(i) \cdot 256^{i-1}$ **B** Evaluation of a time-series taken at 2000 fps of intensities of an LED puled with 200 Hz. **(i)** Change of intensity of the first pixel as a function of the frame number. **(ii)** Image-Number (IN) as a function of the frame number. The continuous increase of frame number verifies that acquired frames are transfered from the camera chip and saved. **(iii)** Integrated image intensity as a function of the frame number.

to resolve the fine details in the images so I want a sufficient spatial sampling.
Knowing the range of frequencies one wants to sample, a lower limit on the sampling rate is set by the Nyquist-Shannon sampling theorem, after Harry Nyquist and Claude Shannon. The theorem states that if a function $x(t)$ contains no frequencies higher than W Hertz, it is completely determined by giving its ordinates at a series of points spaced $1/(2W)$ seconds apart [Shannon, 1949]. For this problem, I have to consider spatial and temporal frequencies.

Spatial sampling: When imaging with a light microscope the resolution is limited by diffraction described by the Abbe formula $\delta = \lambda/2{\cdot}\mathrm{NA}$ with $\mathrm{NA} = 2 \times \mathrm{n} \cdot \sin\alpha$, with n being the refractive index of the medium and α being the half-cone angle of the light collected by the objective. For bright field systems, where a condenser is used for illumination the NA of the objective and the illumination angles are considered and the resolution limit is given by $\delta = \lambda/\ (\mathrm{NA}_{illumination}{+}\mathrm{NA}_{detection})$ [Heintzmann and Ficz, 2007] When imaging with green light and the described lenses we get $\delta \simeq 200\,\mathrm{nm}$, which is our highest spatial frequency resolvable. According to the Nyquist theorem, I need to sample with less than 100 nm to gain the best resolution possible. With the chosen pixel sizes I achieve this limit with the 100x lens or and still get close to it with the 63x lens.

Temporal sampling: To resolve the beat of the axoneme, I am interested in processes which are happening on the timescale of the beat frequency, which is not higher that 100 Hz. According to the Nyquist theorem, I therefore need to sample with at least 200 Hz. As we will see later the characterization of fine details of the shape and important properties of the dynamics require the resolution of the higher modes. In order to be able to resolve the 1st, 2nd and 3rd mode of the oscillation we need to sample with at least 600 Hz. Choosing an acquisition rate of 1000 Hz I am technically able to resolve the first 5 modes of the oscillation.

Integration time: The integration time is the time, in which the camera collects photons that form one image of the time-series. The maximal integration time is given by the rate of acquisition, which in our case is 1 ms. Longer integration times allow for the collection of more light, which results in an increased localization precision as discussed below. However, to select an exposure time one also has to consider the object velocity to minimize motion blur. The tip of a beating flagellum or axoneme reaches peak velocities of approximately 1 mm/s, which is 1μm/ms. This means that integrating over 1 ms during the fastest periods of the beat the axoneme signal will be smeared out over 1μm ($\sim$7 pixels using a 63x lens). To keep the motion blur on the level of the spacial resolution ($\sim$200 nm), I need to decrease the integration time to 200 μs on the cost of signal. The loss of signal can be accounted for by using a brighter light source.

Signal, noise and localization precision: When imaging with a camera, one always faces different sources of noise: Optical noise and detector noise. Optical noise, or shot-noise arises from the stochastic arrival of photons at the detector. It's contribution to the localization error Δx is $\Delta x \sim 1/\sqrt{N}$ with N being the number of photons coming from the specimen. The main contributions to the detector noise are pixel read out noise and noise coming from the dark current of the camera. It's contributions to the localization error are $\Delta x \sim 1/N$. The localization precision of an object can be greater than the optical resolution. Therefore, the number of photons collected from the specimen and the signal to nose ratio have to be considered. Bright field imaging techniques provide enough photons scattered from the specimen that this specific case can be considered shot noise limited. Then the localization error is approximated by $\langle(\mathit{\Delta}\mathrm{x})^2\rangle = \sigma^2/\mathrm{N}$ with $\mathit{\Delta}$x-localization error, σ-standard deviation of the point spread function (PSF) of the microscope and N-number of photons. The relation between the standard deviation of the PSF and the full width of half maximum of a Gaussian intensity profile is given by $\mathrm{FWHM} = 2\sqrt{2\ln 2}\,\sigma \approx 2.3548\,\sigma$ [Thompson et al., 2002]. In the considered case a rough approximation of the localization precision for phase-contrast can be made with: $\mathrm{s} = 0.44\mu\mathrm{m}/2.3548 = 0.19\mu\mathrm{m}$, $\mathrm{N} = \sqrt{\mathrm{SN}}$, which gives $\mathit{\Delta}\mathrm{x} = 12\,\mathrm{nm}$ for dark-field I would expect values of about 2 nm see Figure 3.5 . In my case this localization error applies to the position of the centerline.

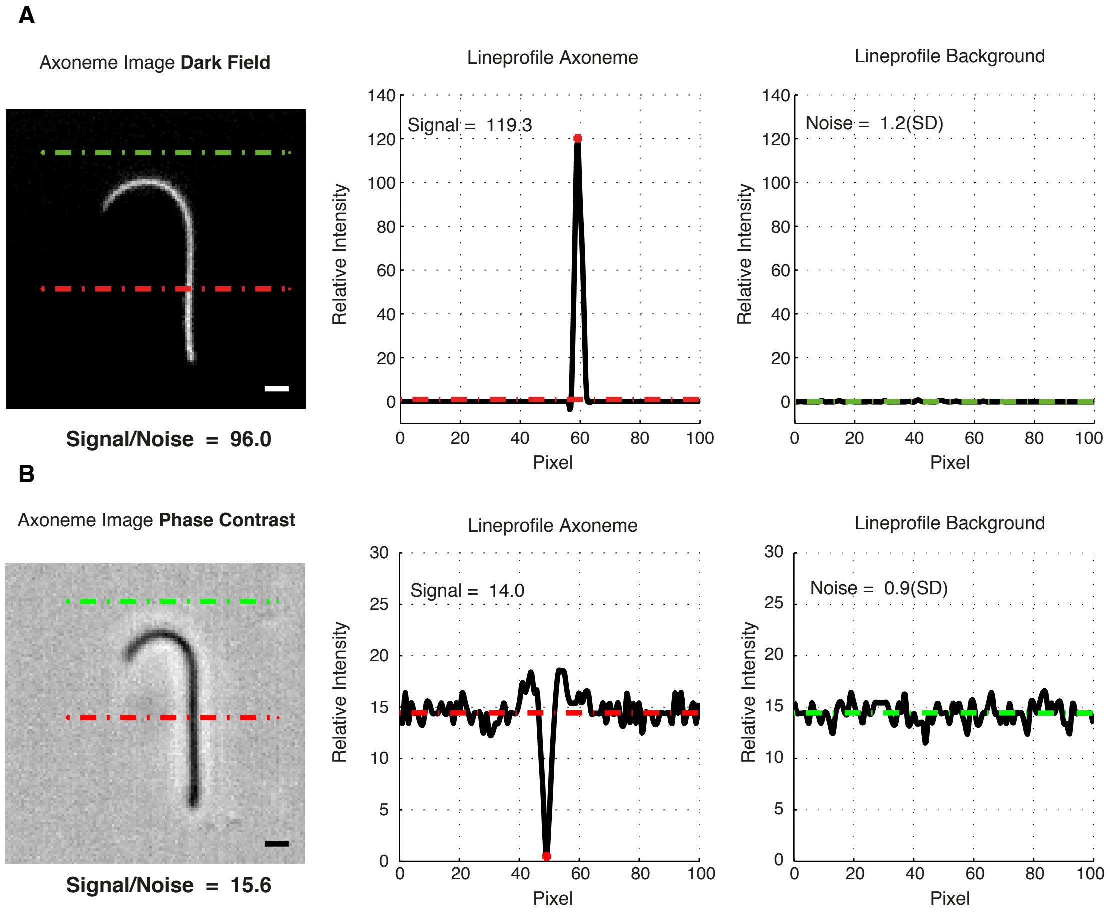

Figure 3.5: Comparison of imaging techniques for reactivated axonemes. Reactivated axonemes have been imaged using Dark-Field and Phase-Contrast microscopy using comparable dynamic range of the camera. The signal to noise ratio was calculated for both techniques after subtraction of the mean-intensity of the time series. This background-subtraction method increased the S/N by a factor of 3 in both cases. **A** Reactivated axoneme imaged using dark-field microscopy (100x lens, Opt 1.6,spectra light engine, 500μs exposure). The signal to noise was SN$\sim$96, the FWHM = 0.44 μm. **B** Reactivated axoneme imaged using phase-contrast microscopy (63x NA1.4 lens, Opt 1.6, Tungsten lamb, 1000μs exposure). The signal to noise was SN$\sim$16, the FWHM = 0.43 μm. Using a brighter light source (Spectra light engine) the exposure time was reduced by a factor of 10 without effecting the signal to noise ratio. Scale bar 1μm.

3.2.2 Precise tracking of isolated axonemes and the flagella of cells

In this study I am tracking flagella and isolated axonemes, which are slender filaments with a length of $\sim 10\mu$m and a width of ~ 200 nm [Bui et al., 2012]. For the tracking of isolated axonemes I use a Matlab based filament-tracking software developed by David Zwicker and Felix Ruhnow [Ruhnow et al., 2011] . For the tracking of cell-attached flagella I use a Matlab-based tracking algorithm developed by Ingmar Riedel and Benjamin Friedrich [Geyer et al., 2013].

Tracking the reactivated axoneme. I recorded movies of reactivated axonemes using dark-field and phase-contrast microscopy with the standard imaging conditions described in Section 3.2.1 . I post-processed the movies by the subtraction of the mean intensity of the image (averaged over the whole movie) from every frame to remove the static background (inhomogeneities arising from uneven illumination and any remaining dirt). This procedure increased the signal to noise ratio by a factor of 3, see Figure 3.5. Before using the filament tracking software [Ruhnow et al., 2011] to precisely determine the shape of the axoneme in every frame I inverted the movie.

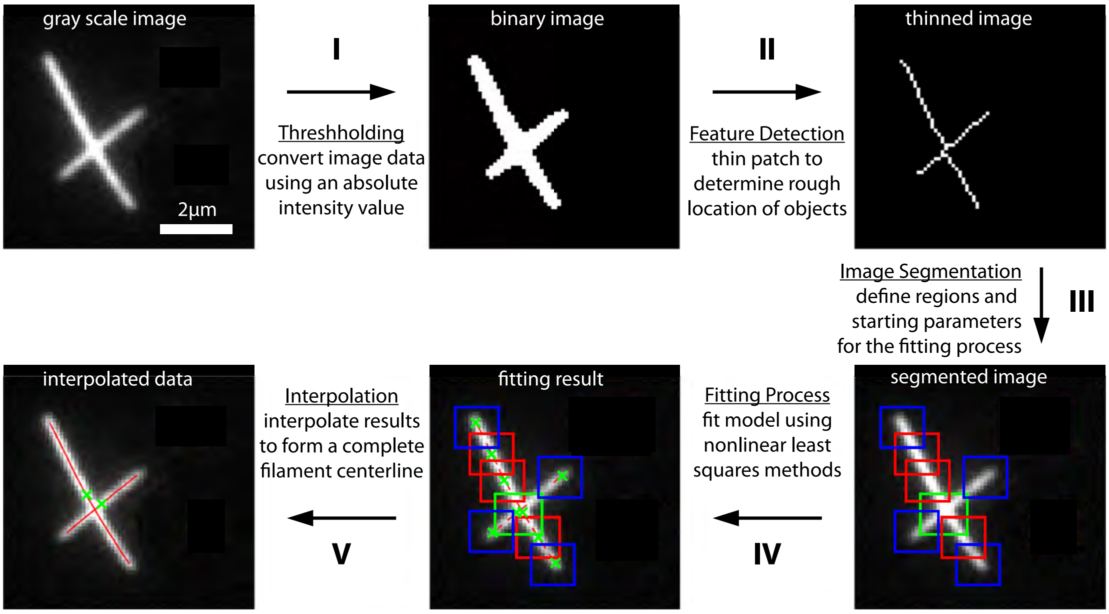

Figure 3.6: Filament tracking using FIESTA. Steps the filament tracking software FIESTA performs to track filament are depicted. The Figure has been adapted from [Ruhnow et al., 2011]

Tracking software: The tracking algorithm performs 5 sequential steps to gain the centerline of the filament. The steps are illustrated in Figure 3.6: 1) Thresholding: Starting from the gray scale image global thresholding preselects the objects of interest. The thresholded image is then converted to a gray-scale image. 2) Feature detection: Gray-scale image is skeletonized using the matlab 'thinning' function. 3) Segmentation: In this step the filament segments are defined. The software differentiates between filament edges, contour regions and crossings. 4) Fitting: For each type of segment a specific 2D gaussian model is fitted. For details on the model and fitting [Ruhnow et al., 2011]. 5) Interpolation: The centerline is found by interpolation of the center-points of each segment. While the model used for fitting segments along the filament considers curvature, the model for the end points does not. The maximal segment size is determined by the full width at half maximum estimate set in the tracking program and calculates as Segment-Size = $8 \cdot$ (FWHM estimate/2.73). Typical settings for the for the tracked axonemes are FWHM = 500 nm, which results in a segment size of 1.5 μm. For tracking curved filaments like the axoneme, I reduce this segment size by 1/4 by default, which results in a segment size of 375 nm. This means that the algorithm can not resolve the filament curvature as close as ~400 nm to each end. The tracking software outputs the positions of points along the centerline of the filament as well as the 95% confident bounds of the position, the sigma of the gaussian 2D fit and intensity information. To test the tracking accuracy, I recorded phase-contrast movies of immobilized axonemes and tracked the shapes. I calculated the transversal tracking accuracy as the mean of the 95% confident bounds of the supporting points of the centerline and the axial tracking-accuracy as the standard deviation of the arc-length of the filament. The tracking-accuracy was 25 ± 2.5nm ($mean \pm SD$,N=10) in transversal and 20 ± 3.5nm in axial direction, which is in the expected range. To characterize the tracking accuracy for in plane beating axonemes, I recorded and tracked dark-field and phase-contrast movies. A series of tracked phase-contrast images as well as the corresponding trajectories of the middle and end points is presented in Figure 3.7.

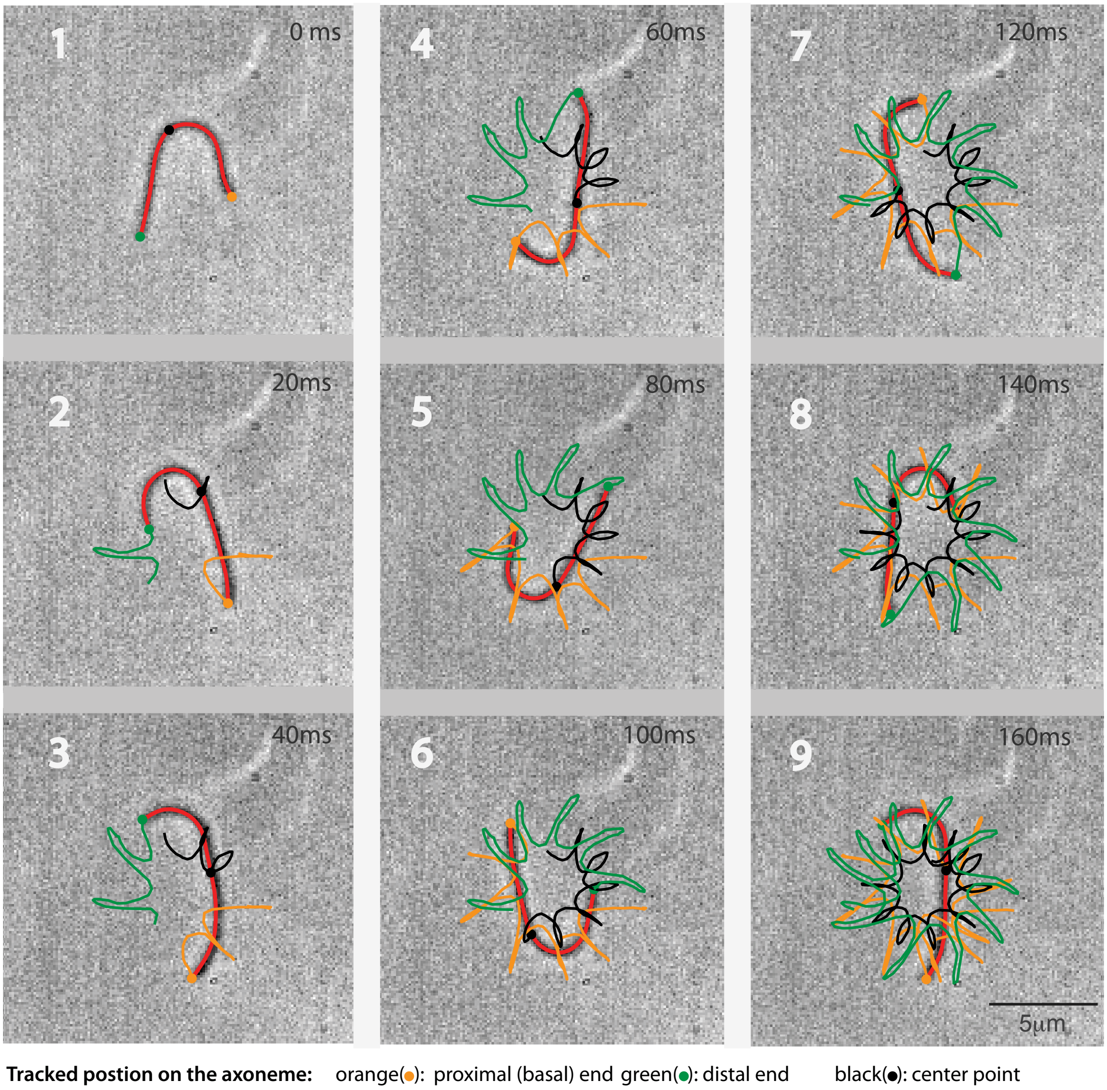

Figure 3.7: Shape tracking of reactivated axonemes. Selected frames from a movie of a reactivated wild type axoneme, were imaged using phase-contrast microscopy, post-processed, and tracked using a filament tracking software [Ruhnow et al., 2011]. The tracked shape of the axoneme (red) is overlaid on the mean-subtracted phase contrast image. The orange, black and green dot as well as the corresponding trajectories depicts the positions of the basal, middle and distal position, respectively, of the axoneme at 0 ms (left panel), from 0 - 60 ms (middle panel), and from 0 - 120 ms (right panel).

I found a tracking-accuracy of 180 nm / 146 nm in transversal and 39 nm / 65 nm in axial direction (dark-field/phase-contrast). When tracking the moving axonemes the standard deviation of the axoneme length averaged over one beat cycle increased by a factor of ~10, much stronger than the standard deviation of the width of the axoneme. Possible explanations for this decrease of localization precision can be (1) tracking problems caused by curvature and changing pixel-interpolation conditions, (2) motion blur, (3) defocussing of the axoneme end during a part of the beat cycle or (4) actual sliding at the end of the structure.

Identification of sources of tracking errors: To rule out the possibility that tracking curved shapes changes the length and increases the standard deviation of the axoneme length I simulated and tracked an axoneme with constant length. If the length would be shape dependent, one would expect a length-variation over the beat cycle, which would produce a periodic signal in time that could be picked up by power-spectral analysis of the length. Figure 3.8 shows the length evolvement over the beat cycle for the simulation and the original data. I find that for the simulation the length as well as the variance of the length is constant throughout the beat cycle. No periodic length change is picked up by power spectral analysis. The original data shows beat cycle dependent variations in the detected length, which are also picked up by power spectral analysis. Possible explanations for the limit of the axial tracking accuracy are mentioned above and are further investigated in a later chapter. This comparison verifies the functionality of the tracking algorithm and shows that for the given imaging conditions the tracking-accuracy is $\sim 170\,\mathrm{nm}$ in the first half of the beat cycle and $\sim 86\,\mathrm{nm}$ in the second half.

Tracking the flagella of the swimming *Chlamydomonas* cell. Imaging and tracking the flagella of swimming cells is much more demanding compared to the isolated axoneme. I image cells using phase-contrast microscopy since in the case of dark-field the scattering of the cell body dominates the image. In phase-contrast the out of focus regions of the cell body contribute to a bright halo around the cell, still the flagella can be tracked from the distal tip to the basal body since the signal of the membranated flagellum is much grater than the signal of the demembranated axoneme. Freely swimming cells usually follow a helical path. To keep the flagella in the image plane, I prevent cell rotation by constraining the cell between two glass surfaces. Constraining the cell in this way slows down the swimming velocity up to a factor of 5, depending on the spacing of the glass surfaces. In this configuration, flagella beat in the focal plane. Nevertheless, a small, but perceivable out-of-plane component of the flagellar beat caused the tip of the flagella to leave the focal plane during the end of the breast stroke, during the recovery stroke the flagellum is close to the cell body which hinders high-precision tracking during the whole beat cycle.

Tracking algorithm: The used tracking algorithm was developed by Benjamin Friedrich and is published in [Geyer et al., 2013] . The tracking of the *Chlamydomonas* flagella is depicted in Figure 3.9 and performed in the following steps:

0. Take a typical (first frame shown)
1. Rotate the template image used for a cross-correlation analysis to estimate the cell position and orientation in every frame of the movie.
2. Track the cell body outline by detecting intensity maxima (green) of line scans along rays (shown in blue) emanating from the putative cell body center and obtain refined estimates for cell position and orientation.
3. Determine the position of the flagellar base using a collection of line-scans (blue lines), followed by a line-scan (green) in a direction perpendicular to the maximal intensity direction (red).
4. Track flagellar shapes in a successive manner using similar combinations of line-scans as described in step 3.
5. The final tracking result. Cell body outline (green), the flagella (blue) and the cell

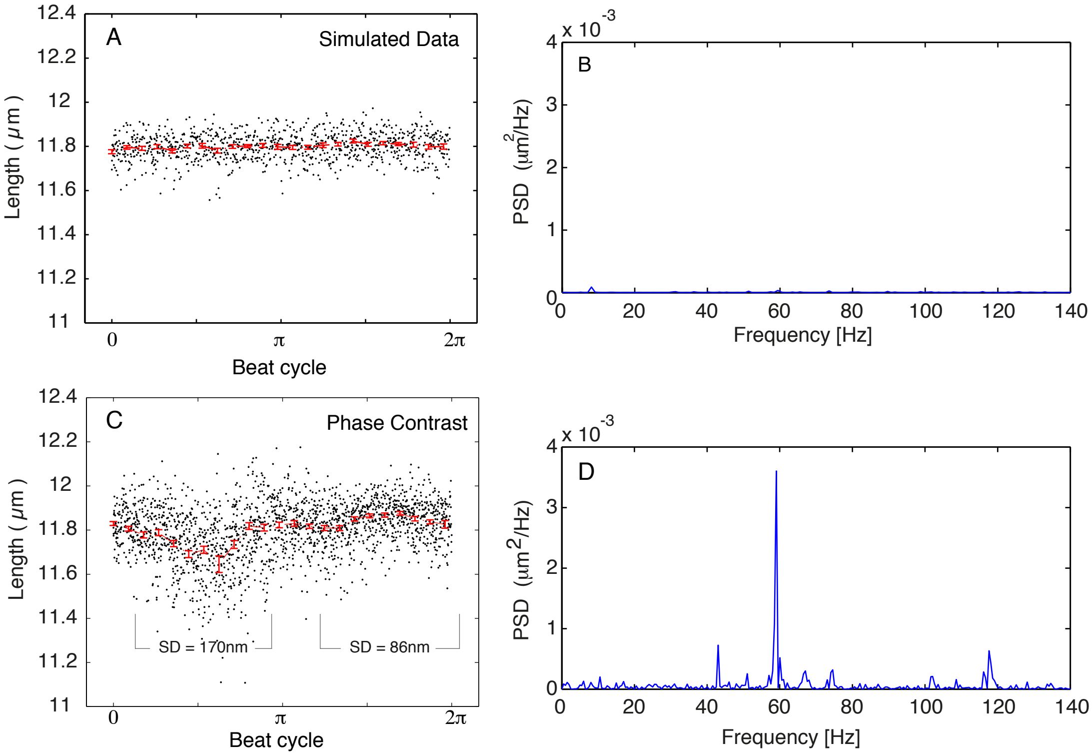

Figure 3.8: Axial tracking accuracy of the axoneme. Reactivated **Chlamydomonas** wt-axonemes have been tracked using filament tracking software [Ruhnow et al., 2011] and beat cycle dependent length variations have been found. Tracking simulated data localizes these variations to be inherent in the experimental data. **A** The length fluctuations of simulated axoneme. Data are presented as a function of the beat cycle. Red points are (mean±SEM) of the data points (black dots). A Tracked axoneme waveform was used to simulate a time series of a noisy axoneme with constant length and a Gaussian intensity profile. The signal to noise and the FWHM of the profile was chosen to match the experimental data. **B** The power spectral density (PSD) of the length shows no detectable periodic changes in the signal. **C** Length fluctuations of the tracked axoneme data as a function of the beat cycle. The red points are (mean±SEM) of the data of one representative axoneme. The dependence of the axoneme length as well as the variance of the length on the beat cycle is generic and was observed in all tested wt examples (N=30). **D** Periodic changes are picked up by power spectral analysis and give an entry at the beat frequency, which is 59 Hz. These changes most likely originate in motion blur and the slight 3 dimensional component of the beat.

center (red dot) and cell orientation arrows.

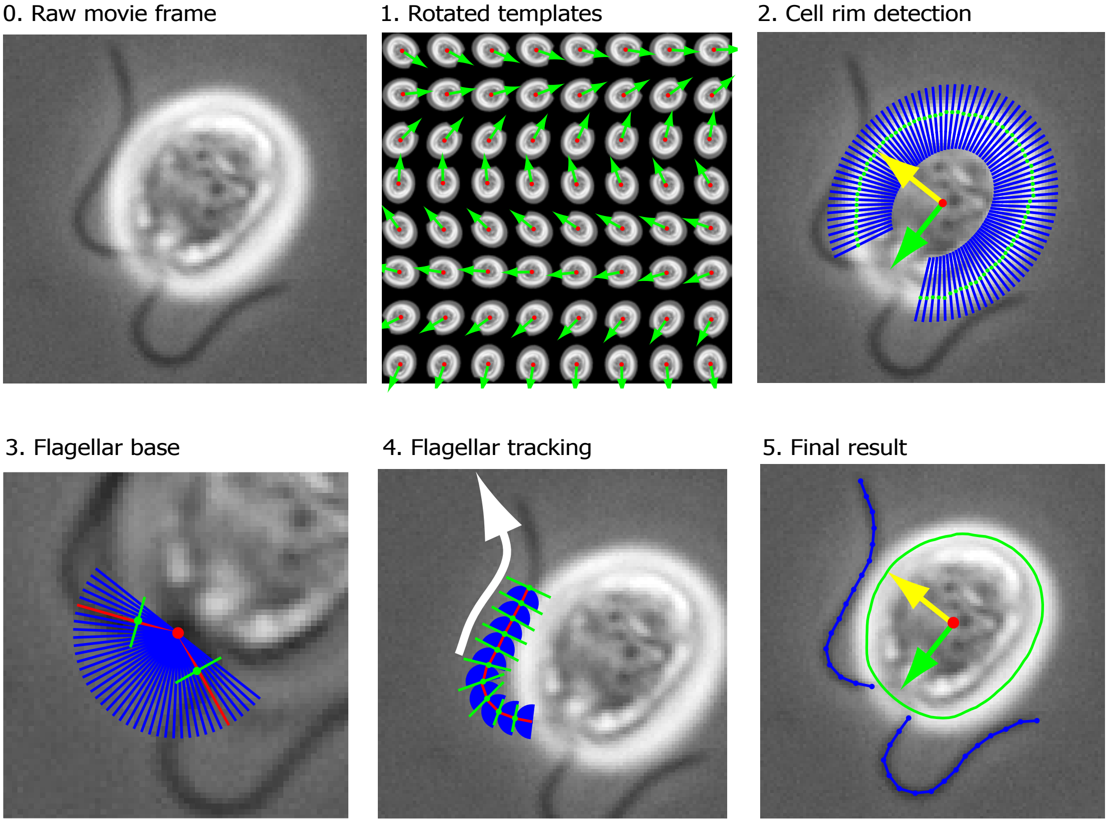

Figure 3.9: Tracking of the flagella of a Chlamydomonas cell. The flagella of **Chlamydomonas** cells are tracked in the following steps: 0. Take a typical (first frame shown) 1. Rotate the template image used for a cross-correlation analysis to estimate the cell position and orientation in every frame of the movie. 2. Track the cell body outline by detecting intensity maxima (green) of line scans along rays (shown in blue) emanating from the putative cell body center and obtain refined estimates for cell position and orientation. 3. Determine the position of the flagellar base using a collection of line-scans (blue lines), followed by a line-scan (green) in a direction perpendicular to the maximal intensity direction (red). 4. Track flagellar shapes in a successive manner using similar combinations of line-scans as described in step 3. 5. The final tracking result. Cell body outline (green), the flagella (blue) and the cell center (red dot) and cell orientation arrows. Images adopted from [Geyer et al., 2013]. Software development by B.M.Friedrich.

3.2.3 High throughput frequency evaluation of isolated axonemes

While precise shape tracking of the axoneme can be used to perform a detailed shape analysis of individual axonemes, the beat frequency alone already contains useful information that can be used to characterize mutants and reaction conditions. Here I present a simple method to determine the beat frequency of multiple reactivated axonemes in a field of view. Similar to the analysis of the body vibration of swimming cells (Kamiya, 2000), I use the Fourier-transform of intensity plots from movies of beating axonemes to determine the beat frequencies of individual axonemes or the distribution of beat frequencies of a large population of axonemes in the bulk.

To determine the beat frequency of individual axonemes, I calculate the standard deviation of the movie and define pixels, which belong to the swimming path of one axoneme by a line that cuts through the center of rotation as shown in Figure 3.10 A. The time evolution of the intensity of all pixels along the selected line for the three different axonemes are shown in Figure 3.10 B. I use the intensity information of the time-distance plots to calculate the mean power-spectral density (PSD) of all pixels along the line Figure 3.10 C.

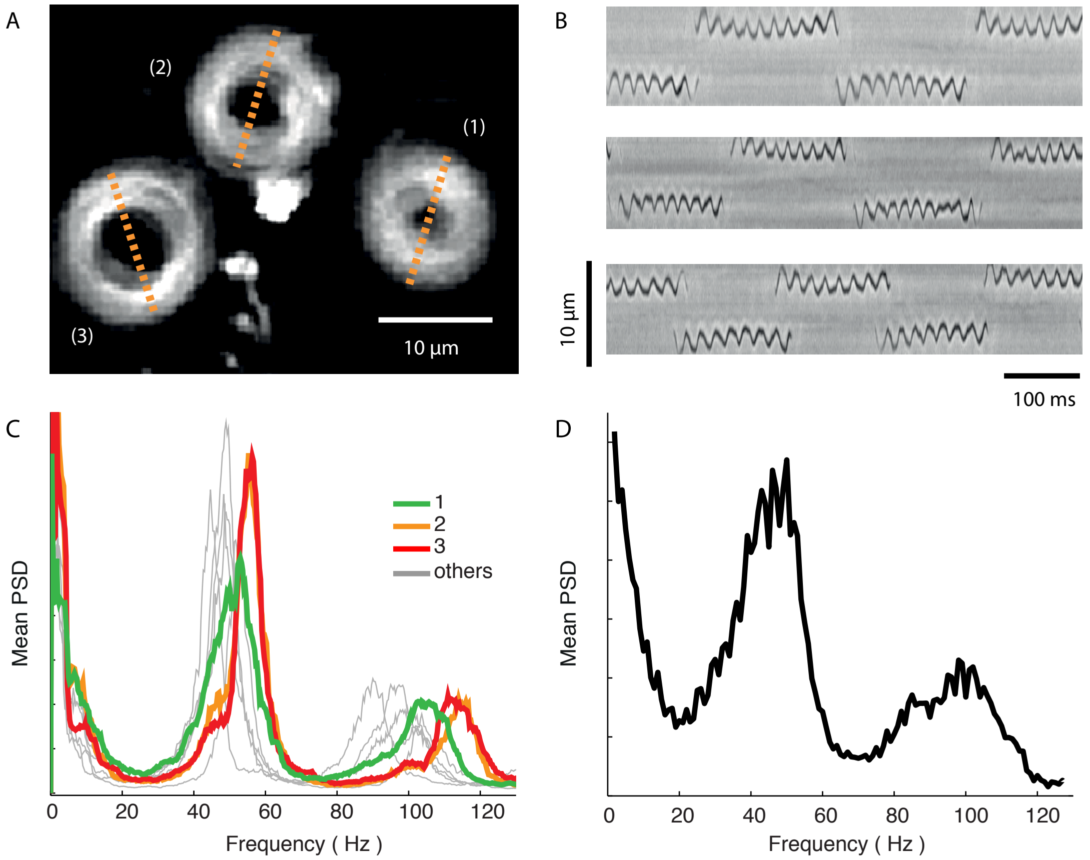

Figure 3.10: Rapid determination of the beat frequency of isolated axonemes. This is a power-spectral analysis method used to rapidly determine the beat frequency of reactivated axonemes. **A** Standard-deviation plot of a 3000 frame phase-contrast movie of reactivated wild type axonemes recorded at 1000 fps. The dotted-yellow lines depict line-scan regions through the center of rotation of the reactivated axonemes. **B** Kymographs (time-distance plots) of the line-scans in (A). Oscillations in the pixel-intensity represent the beat frequency of the axonemes. **C** Mean of the power spectral density of all pixels of each kymograph in panel (B) as well as the data of 6 other axonemes of the same field of view plotted individually. **D** Mean power spectral density of all pixels with standard deviation above the background of the movie containing 9 axonemes. The mean beat frequency is 50±7 Hz. Adopted from [Alper et al., 2012]

The frequency of the 1st mode of the mean PSD was extracted by Gaussian fitting and represents the beat frequency of the selected axoneme. To determine the mean-beat frequency of a large population of axonemes, I calculate the mean power-spectral-density of all pixels with a standard deviation value above the background level and gain the beat frequency from the 1st mode of the PSD as shown in Figure 3.10 D. This is the mean beat frequency of all axonemes in the field of view.

Besides the first mode, one finds higher modes - multiples of the beat frequency in the spectra as well as satellite peaks left and right to the main peak. In Figure 3.11 , I explain the origin of these peaks. The time evolvement of the intensity can be decomposed into 2 frequencies: (1) a low frequency that represents the rotational frequency as the axoneme swims in a circle Figure 3.11 B and (2) the beat frequency with which the axoneme encounters the corresponding pixel Figure 3.11 A. The time evolving intensity signal corresponds to the rotational frequency modulated with the beat frequency Figure 3.11 C. When the rotational frequency is large compared to the SD of the main peak, satellites peaks are appearing. The frequency difference Δf between the satellite and the main peak represents the rotational frequency of the axoneme see Figure 3.11 C(right panel).

The 2nd mode of the oscillation appears because each pixel samples a different part of the amplitude of the oscillation as shown in the Kymographs of Figure 3.10 B , thus it will contribute a different frequency to the mean of the PSD. While pixels that sample low amplitude values contribute to entries at the beat frequency, pixels around the turning point contribute to both the 1st and the higher modes in the PSD. In Figure 3.11 D, this difference is presented by power-spectra of low amplitude values D (i) and high amplitude values D (ii).

3.2.4 Beat frequency characterization of the reactivated WT axoneme

The beat frequency evaluation method described above can now be used to characterize the beat frequency distribution of WT axoneme preparation.

Reactivation time and ATP regenerating system: Here I consider a typical wt-axoneme preparation reactivated with 1 mM ATP at a temperature of 25.1°C. I use a typical 1:10 dilution of the axoneme stock where single, non-interacting axonemes are observed. I find the axonemes being reactivated for 25 minutes with a decreasing beat frequency over time, which allows for the approximation of an averaged rate of ATP consumption ~ of 0.22 n mol/min in a 5.4 μl channel, see Figure 3.12 . To keep the ATP concentration constant for a longer time I use an ATP-regenerating system composed of creatin kinase and creatine phosphate. One unit of creatine kinase transfers ~1.0 μ mole of phosphate from creatine phosphate to ADP per min. To ensure that ADP can be regenerated rapidly, I used 1 Unit/mL, which leads to a regeneration rate exceeding the consumption rate ~25 fold. The reactivation time can now be tuned by the Creatine Phosphate concentration. Assuming that the creatine phosphate consumption rate is equal to the ATP hydrolysis rate, I expect that 5 mM Creatine Phosphate are used up in ~125 min. I find that the beat frequency drops to zero in ~65 min. To be not limited by substrate for the kinase, I use a 10 fold higher creatine phosphate concentration in my assays. At the total consumption rate of 0.42 n mol/min measured for the use-up of 5 mM creatine phosphate, I expect the ATP regeneration capacity of the solution to last for 115 min, where 90% of the creatine phosphate is used up and the remaining concentration is 1 mM. This calculation is supported by the measurement in Figure 3.12.

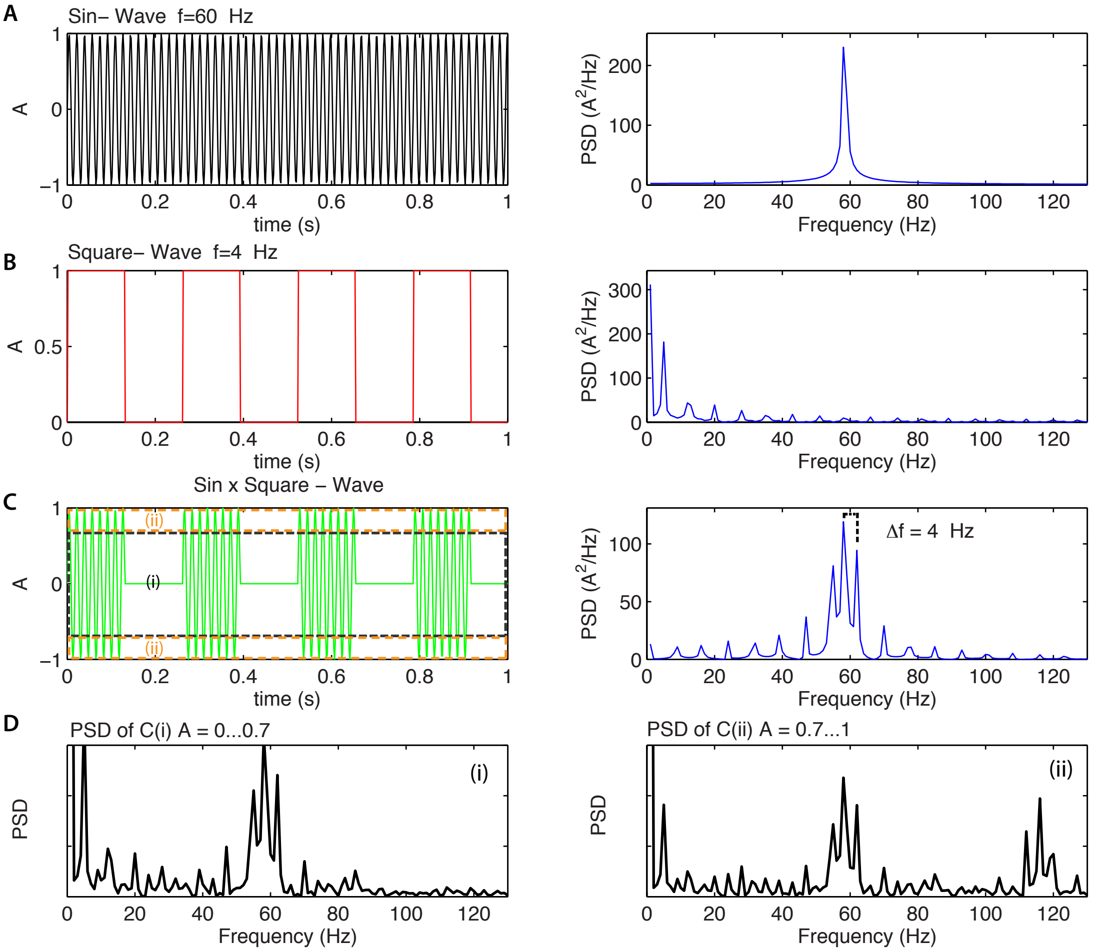

Figure 3.11: Simulation of the Power Spectrum of the pixel intensity of a beating axoneme movie. The PSD gained in Figure 3.10 C/D is modeled in this figure. **A** Time and frequency domain representation of a sin wave f=60 Hz. **B** Time and frequency domain representation of a square wave f=4 Hz **C** Time and frequency domain representation of the product of A and B. Two different amplitude regions are depicted with (i) and (ii) in the left panel. Note that the frequency difference Δf between the main and satellite peak represent the frequency of the square wave in the right panel. **D** PSD of different amplitude regions shown in C. (i) Region A = -0.7...0.7, (ii) Region A = -1...-0.7 and 0.7...1

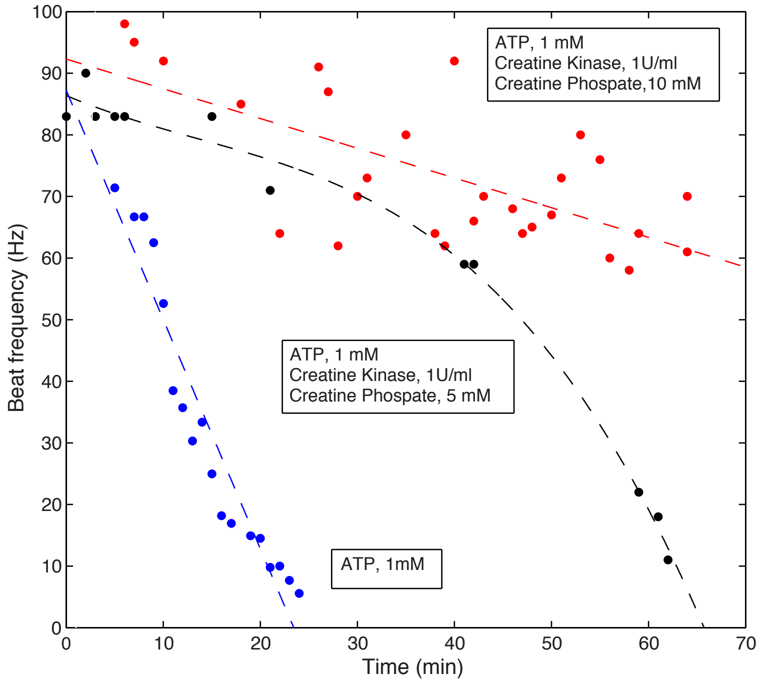

Figure 3.12: Beat frequency as a function of time for different conditions. The beat frequency over time was recorded for different reactivation conditions: no ATP-regeneration system (blue dots), ATP-regeneration system with 5 mM Creatine Phosphate (black dots),ATP-regeneration system with 10 mM Creatine Phosphate (read dots). To characterize the ATP consumption without sampling the whole distribution, only the fastest axonemes have been considered to estimate the beat frequencies. The temperature during the experiment was 25.1 ° C. The dashed lines are linear (blue and red) and polynomial (black) fits to guide the eye.

An interesting feature of the reactivation with regenerating system is that the initial beat frequency is 10-20% higher than the mean beat-frequency after 10 minutes then the beat frequency stays constant for at least 40 minutes. This is the time-window I will use for my experiments.

Beat frequency distribution of reactivated WT axonemes: To characterize the actual spread of beat frequencies during the reactivation period I measured a wt-beat-frequency distribution using the frequency evaluation method described in Section 3.2.3. The gained distribution is shown in Figure 3.13. I find the mean beat-frequency to be 50 ± 13 Hz (mean $\pm$ SD,N=328).

Creatin/ creatine phosphate ATP regenerating system can be used to prolong the reactivation time of isolated axonemes. Interestingly, the regenerating system uses up it's substrate Creatine Phosphate twice as fast as it produces ATP. The assumed ratio of phosphate to ATP is a 1:1 ratio. An explanation for this finding could be a basal consumption rate of Creatine Phosphate even in absence of ADP. A degradation of enzyme over the course of the experiment can be excluded since a higher creatine phosphate concentration leads to longer reactivation. I use a reactivation time-window of 40 minutes, which is a reasonable time to perform extensive data acquisition. To characterize the reactivated axoneme system, I investigated the beat frequency distribution for standard reactivation conditions. The mean beat frequency was 50 ± 13 Hz (mean $\pm$ SD,N=328), which is similar to what has been reported for intact wt cells [Witman, 2009]. This shows that the isolation does not alter the beat frequency. In previous studies performed on

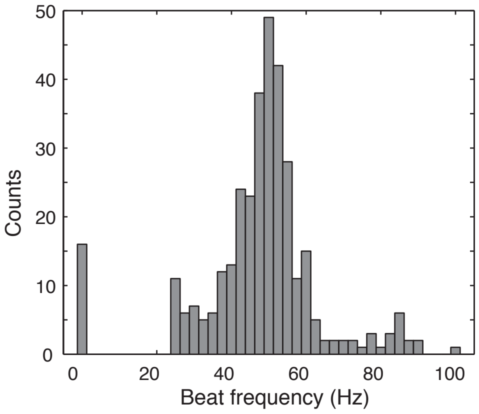

Figure 3.13: Beat frequency distribution of reactivated wt axonemes. The beat frequency distribution of reactivated WT-axonemes was measured in the presence of 1 mM ATP, 1U/ml creatine kinase and 10 mM creatine phosphate at 24 °C. Beat frequencies were evaluated using the Fourier analysis methods described in Section 3.2.3. The mean beat frequency was 50 ± 13 Hz (mean ± SD,N=328). Reactivation of 95% of the axonemes was observed. Non reactivated axonemes were counted with zero beat frequency and not included in the calculation of mean and SD.

reactivated cell models a bimodal frequency distribution with a frequency difference of 30% [Kamiya, 2000] was reported. Based on this observation, the authors claimed that the cis- and trans-flagellum could be differentiated. For the reactivated axoneme, I can not detect such a difference in beat frequencies although I find minor populations that beat significantly slower or faster. This could suggest that the left and right flagellum are anchored differently and this anchorage is giving rise to the to the difference in beat frequency.

Chapter 4

Results and Discussion

4.1 The beat of the axoneme propagates from base to tip

When axonemes are isolated by the dibucaine-procedure described in Section 3.1.2 they are severed from the basal body in the transitional region as shown in Figure 1.4 . Although we can observe their beat after reactivation, we have no direct information about their integrity (particularly at the ends), their polarity or their original orientation with respect to the cell body. Knowing these properties is important to identify sources of variability of the shape parameters, define the boundary conditions for the beat and the direction of wave propagation as well as tying swimming behavior of the cells and beat shape of isolated axonemes together.

4.1.1 TEM study reveals no sliding at the base of a bend axoneme

To visualize the integrity of demembranated axonemes I performed electron microscopy on reactivatable sample of a standard WT axoneme purification. I found that more than 95% of the axonemes were intact, meaning that they did not exhibit any sign of disintegration. All axonemes showed no remains of membrane. Membranated axonemes do not exhibit the ultrastructure seen here and patches of membrane on the axoneme appear as white sparkles or spheres (Examples are not shown here). Another sign for a preparation of intact axonemes is that no axonemal fragments like outer dynein arms or radial spokes can be seen in the background (personal communication Gaia Pigino). Typical examples of intact axonemes are shown in the middle panel of Figure 4.1. Since the considered axonemes were bent during the sample preparation, one can clearly distinguish a blunt end from a more splayed end. The blunt end most likely represents the basal end, whereas the splayed end represents the distal tip. Both ends are shown at a increased magnification in the left and right panel of the figure. The distal-end exhibits single doublet microtubules, which seem to be slid out to different length and thus end at different arc-length positions. When one considers the axoneme to be a composed of filaments with a cylindrical arrangement, a cross-sectional diameter a and length L then the sliding displacement at the end $\Delta(L)$ between filaments on opposite sides is given by $\Delta = a \cdot \Psi(L) - \Psi(0) + \Delta(0)$ with Ψ being the tangent angle and $\Delta(0)$ being the sliding displacement at the base. Based on the assumption that the there is no sliding at the base, I can approximate the sliding displacement for the example axoneme A with $\Delta_A = 220\,\mathrm{nm} \cdot 1.7\,\mathrm{rad} \backsimeq 375\,\mathrm{nm}$ and for the example axoneme B with $\Delta_B = 220\,\mathrm{nm} \cdot 1.0\,\mathrm{rad} \backsimeq 220\,\mathrm{nm}$. To test if the width of the tip and base is dis-

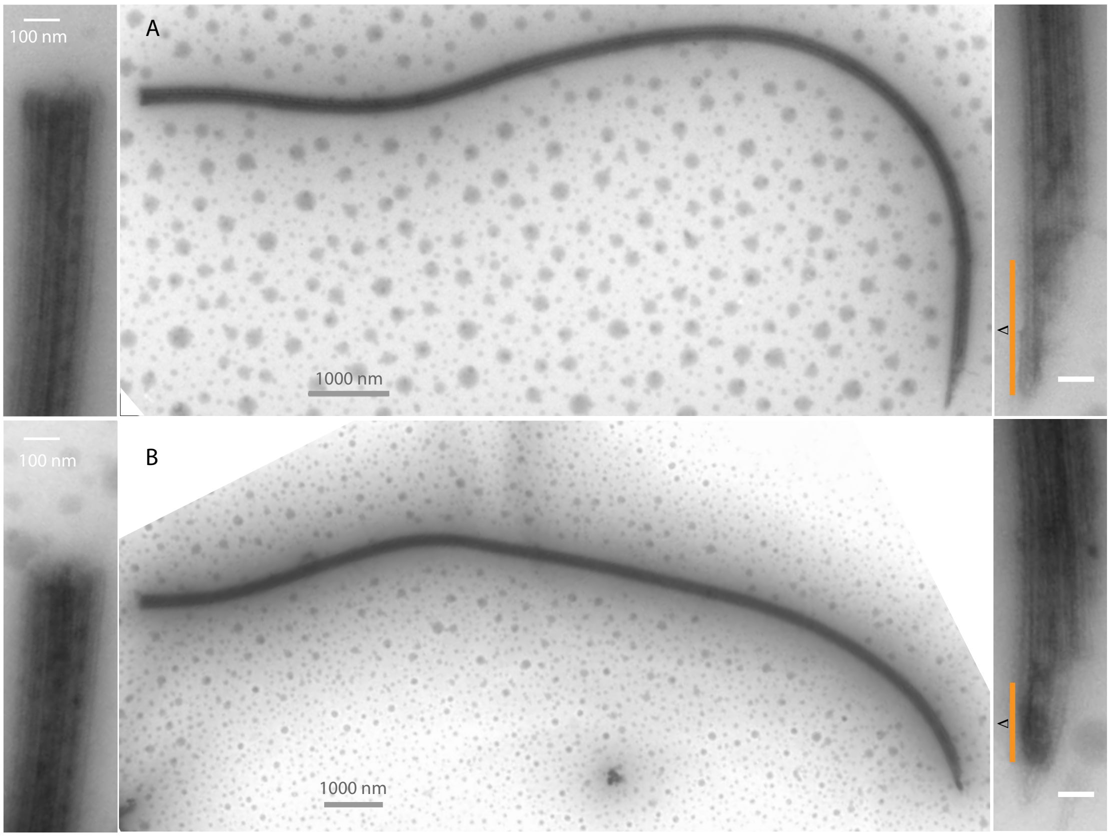

Figure 4.1: TEM images of demembranated axonemes. Demembranated axonemes were stained with in Uranyl Acetate for 1 minute, transfered to a carbon support and imaged using transmission electron microscopy. The middle panel shows images of two whole axoneme (A/B). The used TEM-magnification was 1900 x. The left and right panel show the proximal (base) and distal (tip) end, respectively. The used TEM-magnification was 23000 x. The orange line in the right panel show the expected sliding displacement Δ for an axonemal diameter $a = 220\,nm$ calculated based on the differences of the tangent angles at the ends $\Delta = a \cdot \Delta\psi_{l-0}$, which was $\Delta\psi_A = 1.7$ rad and $\Delta\psi_B = 1.0$ rad resulting in a $\Delta_A = 375$ nm and $\Delta_B = 220$ nm. The mean width of the axoneme is 212±18 nm (mean±SD,N=36), measured with 6 measurements on each of 6 considered axonemes. The width was measured from a line-scan perpendicular to the axoneme using the FWHM distance. The measurement error for a single measurement was ≤ 5 nm. The difference in width between base and tip is 10±6 % with the base being widest (mean±SD, N=6). The width was measured within the 2nd micron from the respective end. In each case, the width of base and tip was significantly different from each other using a t-test (p<0.05, N=6). Images were acquired in the EM-facility at the MPI-CBG with help of Andrzej Mleczak, Pigino group. The scale bar in the side-panels is 100 nm, in the middle panel 1000 nm.

tinguishable, I performed perpendicular line-scans within the 2nd micrometer from the respective end to measure the width. I found the considered axonemes to have a mean-width of 212±18 nm (mean±, N=36), whereas the basal end was always significantly wider than the distal end. The difference is in the order of 10% of the total width and thus ∼5 times larger than the measurement uncertainty of a single measurement which was <5 nm.

Discussion: I used electron microscopy to verify the applicability of the used isolation and demembranation method. I find the percentage of as intact classified axonemes to be ∼ 95%, which is the same percentage of axonemes that were reactivatable. The fact that bend axonemes in the preparation exhibit one blunt end suggests that sliding at this end is strongly restricted. I calculate an expected sliding displacement at the end of the axoneme based on the shear angle. The approximation for the sliding displacement seems reasonable (see,Figure 4.1 as orange line) I therefore conclude that (1) the blunt end is the base of the axoneme and (2) sliding is more strongly restricted at the base than on the distal tip. From the literature we know that unlike bull sperm-tails, which have tapering additional fibers on their outside, the *chlamydomonas* axoneme is more homogeneous along its length. Measuring the diameter in the first and last 2μm separately, I find the basal end to be 10% wider than the distal end. Since we know, that in the basal region additional structures and cross-links like the 1-2 bridge are located (see Section 1.3.3) one could imagine that these structures introduce additional spacing between the adjacent doublets. Additionally, dyneins, which are filament bound in absence of ATP, could apply compressive forces to the axonemal structure. Due to additional structures in the proximal portion of the axoneme, its compressibility could be lower in that region compared to the distal end resulting in a difference in width. These suggestions could be tested in follow-up experiments in which the width and the sliding properties at the ends could be investigated in conditions of low ATP where motor activity bends the axoneme and in ATP-Vanadate where motors are completely detached.

4.1.2 The direction of wave propagation is directly determined from the reactivation of polarity marked axonemes

Chlamydomonas flagella are growing out from the centriol of the cell, which is termed the basal body see, Section 1.2. The microtubules in the structure are pointing with their minus-ends towards the base while plus-end always builds the distal tip. As the flagellum beats, the bending wave propagates from the base to the tip. After isolation of the flagella, this polarity mark is lost and thus the direction of bend propagation in the reactivated axoneme is unknown. To elucidate the direction of wave propagation in the isolated axonemes, I specifically labeled the plus-end using fluorescent tubulin. I incubated purified and demembranated axonemes with TRITC labeled tubulin under growth promoting conditions and stabilized the outgrown microtubules using taxol. Since the rate of polymerization at the plus end is ~ 2 timed higher compared to the minus end [Walker et al., 1988], the comparison of the intensities at the axoneme ends can be used to show the polarity of the axoneme. Panel A in Figure 4.2 shows a typical axoneme imaged in phase-contrast that exhibits fluorescently labeled ends by polymerization of microtubules.

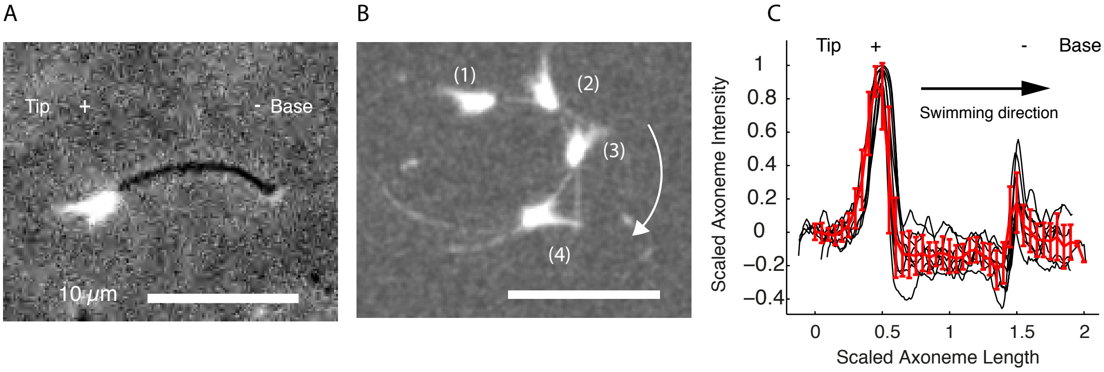

Figure 4.2: Reactivation of polarity-marked axonemes. Demembranated WT-axonemes were incubated with 10 μM porcine tubulin, a (1:3) mixture of rhodamine-labeld and unlabeled tubulin and incubated in presence of 1mM GTP and 1mM $MgCl_2$ at 28°C for 10 minutes. Fluorescent microtubules polymerized at the ends of the axoneme were then stabilized using 10μM of taxol. The end-labeled axonemes were separated from the free fluorescent dimers by airfuge-centrifugation at 30 psi for 5 min. Axonemes were then reactivated in BRB80 + 1 mM ATP. **A** Typical snapshot of a reactivated axoneme: The bright end in the fast-growing (+) end the dim end the slow-growing (-) end. Axonemes were imaged using a combination of phase-contrast (black axoneme) and TRITC-fluoresence (white microtubule extensions at the ends) **B** Standard deviation plot of 4 consecutive snapshots with a Δt=55 ms. The swimming direction is indicated by the white arrow. The reactivated axoneme swims minus-end in front, which indicates that the direction of wave propagation is from - to + end reminiscent of base and tip of the axoneme. **C** Axial intensity-profiles of 8 axonemes were rescaled to the (1) maximal intensity in y and (2) the axoneme length in x and aligned by their direction of swimming. The (mean and SD, N=8) was calculated for bins of 0,02.

This image shows an appreciable difference of intensities between its ends, with the bright end being the + and the dim end being the - end as proven later. To relate the polarization to the direction of wave propagation, I reactivated polarity labeled axonemes. Figure 4.2 B shows the standard deviation plot of selected snapshots of a movie of a reactivated axoneme, presenting polarity and swimming direction simultaneously. For the axoneme to swim forward, the traveling wave must propagate opposite to the swimming direction. I find that in 100% of the observed cases (N=25) the reactivated axonemes swims with the dim end first. Since the dim end is the minus end, the traveling-wave propagates from the minus to the plus end. In Figure 4.2 C, I aligned the intensity profiles of 8 reactivated axonemes with respect to their swimming direction. The ratio of the mean intensities between both ends is ∼4.5, and thus significantly discriminating the two ends from each other. To exclude the possibility that polymerization at the plus end of the axoneme is not governed or altered by end-attached growth regulating maps, and to directly relate the intensity at the end to the axoneme polarity I performed a kinesin-1 gliding assay using polarity-marked axonemes. Figure 4.3 A shows the kymograph of such an assay where I imaged the axoneme using dark-field and the extension using fluorescent microscopy. Kinesin-1 is a plus end directed motor, thus transporting filaments leading with their minus ends. The assay shows that the axoneme is transported leading with its dim (-)end. The direction of gliding verifies the polarity mark generated by the polymerization of fluorescent tubulin. In panel B of Figure 4.3 , the intensity profiles of the dark-field and the TRITC signal from panel A are plotted.

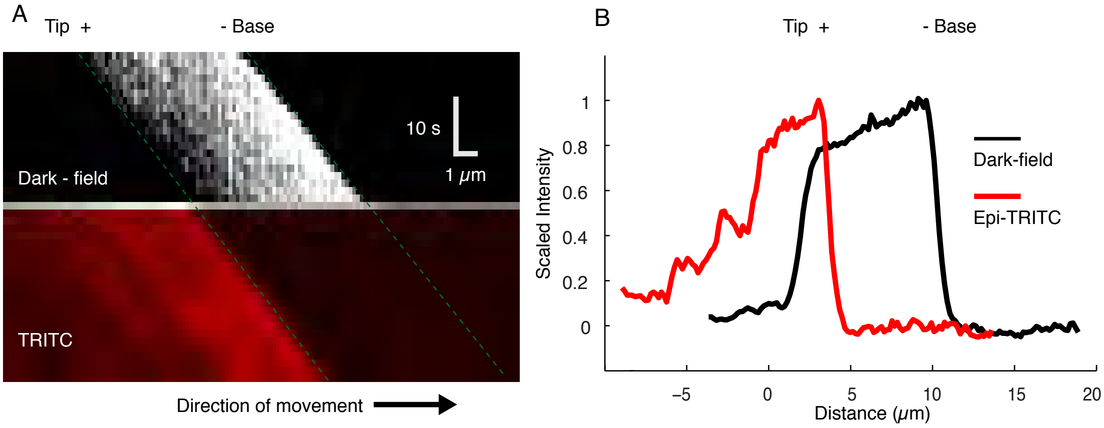

Figure 4.3: Kinesin-1 gliding assay of polarity-marked axonemes. Axonemes were labeled with fluorescent tubulin as described in Figure 4.2. Labeled axonemes were introduced to a kinesin-1 coated surfaces and the gliding motility in presence of 1mM ATP and 80μM of vanadate was observed with both dark-field and TRITC-fluorescence. **A** Kymograph of a gliding axoneme imaged in dark-field (upper panel) and fluorescence (lower panel). Kinesin-1 moves towards the plus-end of microtubules, thus the axoneme is transported minus end first. This verifies the polarity deduced from the fluorescent end-labeling with the dim-end being the (-) end of the axoneme. Note: The fluorescent microtubules at the axoneme ends showed a low dark-field signal only. Due to thresholding, this signal is not visible in the figure. The same applies to the TRITC signal on the - end of the axoneme. The uneven TRITC intensity on the plus end originates from the frayed axoneme ends as visible in Figure 4.2 . The green-dashed lines depict the ends of the axoneme. **B** Intensity profiles from panel A with the dark-field channel showing the axoneme (black) and the TRITC channel showing the fluorescent microtubule-extensions.

The dark-field signal shows an intensity gradient along the length of the axoneme. Analysis of 15 end-labeled axonemes consistently showed the same intensity gradient. For illustration I color-coded the dark-field intensity in a kymograph of a gliding axoneme, see Figure 4.4 A and plotted the mean intensity-profile of this gliding and a beating, non-labeled axoneme in Figure 4.4 B C. This profile shows that the intensity is ∼20 % increased at the basal end and decays over half of the length of the axoneme. Similar to the gliding assay I investigated the mean intensity of the beating axoneme. I found a similar intensity decrease in 100 % of the 10 investigated cases. A representative example is given in Figure 4.4 C showing a intensity difference of ∼30 % between the ends.

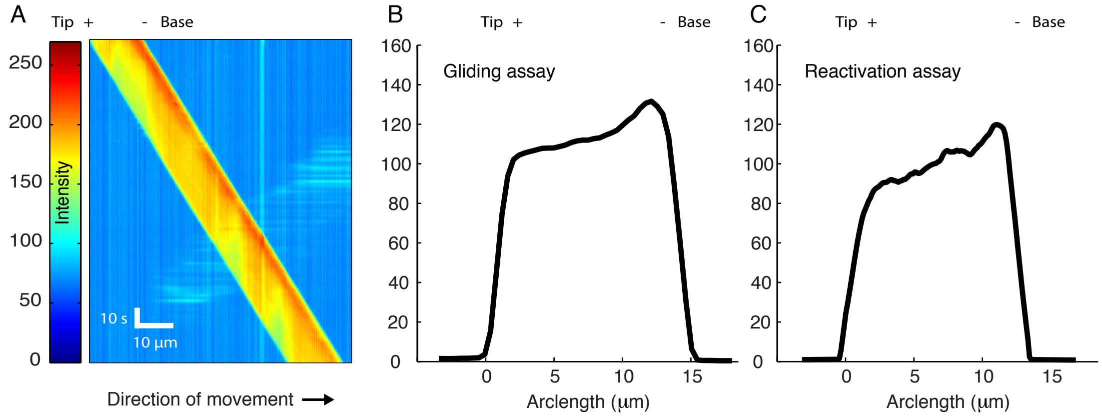

Figure 4.4: Dark-field intensity profile of the beating and gliding axoneme. In the beating and non-beating case, the dark-field intensity along the length of the axoneme decreases from plus to minus end and thus can be used for a label free determination of the polarity. **A** Kymograph of a gliding axoneme. The intensity is color coded. **B** Mean intensity-profile of the gliding axoneme in A with the background set to zero. The intensity difference between base and tip is ~25%. **C** Mean intensity profile of a reactivated axoneme. The intensity difference between base and tip is ~30%.

Discussion: Determining the polarity of the axoneme is important to define the direction of wave propagation for the isolated axoneme. Theoretical studies suggested that in the axoneme the direction of wave-propagation may be set by the boundary conditions [Riedel-Kruse et al., 2007] , which are greatly altered when the axoneme is isolated from the cell. I find that in the case of a reactivated wt axoneme the traveling wave propagates from the base (-end) to the distal tip (+end), which is the same for intact cell attached flagella. This shows that the direction of wave propagation is not altered by the isolation from the cell. To discriminate the two ends, I make use of the enhanced polymerization of fluorescent tubulin on the plus end of the axoneme. Another way of marking the polarity of the reactivated and non-reactivated axoneme is to use dark-field microscopy to observe an intensity gradient along the length of the axoneme. The intensity difference between base and tip is ~ 25% of the total intensity and is greatest in the basal half of the axoneme. While the structural origin of this difference is unknown, we know the dark-field intensity strongly depends on the scattering diameter of a rod (DF-Signal $\propto r^4$) and relates the amount of mass contained inside the structure. Both effects could contribute: (1) We know that the basal half of the axoneme contains the 1-2 bridge, which has a different consistency than the dynein motors which are missing along the occupied stretch (see, Section 1.2). (2) Using TEM, I showed that the diameter is increased at the base, which could also result in a increased signal assuming constant protein density. Hereby a 25% intensity difference that I detected in the non-beating case would suggest a difference in diameter of 6 %. This is in the range of what I measure using electron microscopy where I observe a difference in width between tip and base of about 10±6 %. To elucidate the origin of the intensity gradient, it would be interesting to investigate the axonemal density by kryo-electron tomography and to model the dark-field image formation for this object. In a next step it would be interesting to determine the direction of wave propagation for different isolated mutant axonemes and reactivation conditions. An interesting reactivation condition could be the presence of calcium as it has been shown to change the direction of wave propagation in trypanosoma flagella, where the wave propagates from the distal tip to the base.

In addition to the EM studied the successful polymerization of microtubules from the axonemal ends is an additional prove of the successful demembranation of the structure.

4.1.3 Summary

In this section I have shown that the isolated and demembranated axoneme is lacking the membrane while the axonemal structure is still intact. Electron microscopy furthermore allows to clearly distinguish the distal tip from the base, with the basal-end being the blunt-end and the distal-tip being the splayed-end. In the EM preparations, bend axonemes exhibited a blunt base. This suggests that sliding at the base is efficiently restricted in the axoneme. I find that the diameter at the distal-end is smaller than at the basal-end.

While the ends of the isolated axoneme can be distinguished using EM, they have not clearly been distinguished in light microscopy. I show that the dark-field intensity decreases from base to tip and therefore can be used to identify the axonemal polarity. Using fluorescent labeling of the plus end of the axoneme I furthermore show that the traveling bending-wave during the beat propagates from base to tip. This is the same direction the wave propagates in the cell, which shows that the change in boundary conditions after isolation does not alter the direction of wave-propagation.

4.2 The asymmetric beat is the superposition of a static circular arc and a sinusoidal beat

4.2.1 The waveform is parameterized by Fourier decomposition in time

The axonemal or flagellar waveform is given by sets of xy coordinates with respect to the laboratory, which describes the shape in time. Here I consider the beat to be planar, strictly speaking I am characterizing a 2D projection of a 3D beat. Each shape is parameterized by the tangent angle $\Psi(s,t)$ with s being arc length and t being time. In this representation the shape is given by the position vector $\mathbf{r}(s,t)$ where $\mathbf{r}(0,t)$ denotes the trajectory of the basal end of the axoneme, see Equation 1.1. Plots of the tangent angle over time for different arc-length positions as well as the shapes are shown in Figure 4.5 D/A. Since the tangent angle representation switches the reference coordinate system from the lab frame to the axoneme frame, the information about the trajectory of the first point is lost in that step.

Axoneme rotation: Since the axoneme swims on a circular path, the angular representation contains information about the global rotation of the axoneme which is represented by the rotational frequency f_{rot} in units of (rotations/s). I calculate the rotational frequency f_{rot} from the slope k of a linear fit of the tangent angle over time as depicted in Figure 4.5 D by the red dashed line. Since the axoneme performs a global rotation, f_{rot} is the same at each arc-length position s and given by $f_{\text{rot}} = k/2\pi$. To reveal the periodic nature of the flagellar beat, we express flagellar shapes with respect to a reference frame that rotates at a rate f_rot. With respect to this co-moving frame, the shapes are given by the tangent angle with subtracted global rotation:

$$\psi(s,t) = \Psi(s,t) - f_{\text{rot}}\, t \tag{4.1}$$

The gained representation, which I term the shape-angle representation presents the waveform as viewed by an observer that swims on the trajectory of the first point as shown in Figure 4.5 B.

Unlike the shear-angle representation, the shape-angle representation preserves the first angle and thus the information about the amplitude of the beat. A time-series of arc-length dependent shape angles is shown in Figure 4.5 E. It shows the preservation of the first angle as well as a static, length dependent offset at each point. This time independent offset is the 0th Fourier mode and I subtract is for further evaluation of the shape dynamics as shown in Figure 4.5 F. The corresponding shape of the dynamic component of the beat that we gain from Equation 1.1 is shown in Figure 4.5 C. To characterize the oscillatory shape changes with respect to the arc-length s, I perform a Fourier decomposition of $\psi(s,t)$ at each arc-length position in time. It is legitimate to use this method because the oscillations are stable on the time-scale of the observation.

$$\psi(s,t) = \sum_{n=-\infty}^{\infty} \widetilde{\psi}^{(n)}(s)\, e^{i\omega n t} \tag{4.2}$$

This decomposition represents the shape dynamics by the temporal-Fourier coefficients $\widetilde{\psi}^{(n)}(s)$ from which I extract the arc-length dependent shape parameters amplitude $A_n(s)$ and phase $\phi_{(n)}(s)$:

$$A_n(s) = |\widetilde{\psi}^n(s)| \qquad \phi_{(n)}(s) = Arg\, \widetilde{\psi}^{(n)}(s). \tag{4.3}$$

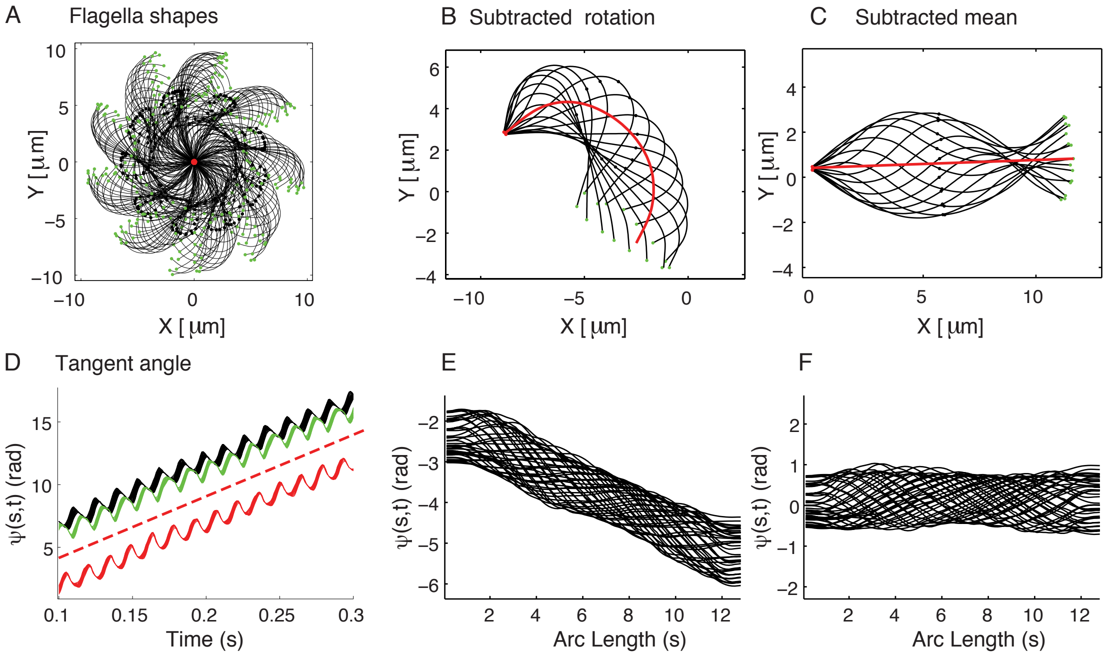

Figure 4.5: Tangent Angle description of the waveform. **A** Superposition of flagellar shapes calculated from the tangent angle. In the angular representation, the information about the trajectory of the first point is lost. **B** Shapes after subtraction of rotation. The mean-shape is depicted in red. **C** Shapes after subtraction of the mean shape (read line in B) **D** Tangent angle as a function of time, plotted at the basal (red), middle (black) and distal (green) position of the axoneme. The corresponding colors show the trajectories of angles over 3 μm over the arc-length. The dashed red line represents a linear fit with the slope k, which represents the angular velocity. The rotational frequency of axoneme f_{rot} is given by $f_{\mathrm{rot}} = k/2\pi$. **E** Time-series of tangent angles with respect to arc-length. **F** Time-series of mean-subtracted tangent angles with respect to arc-length.

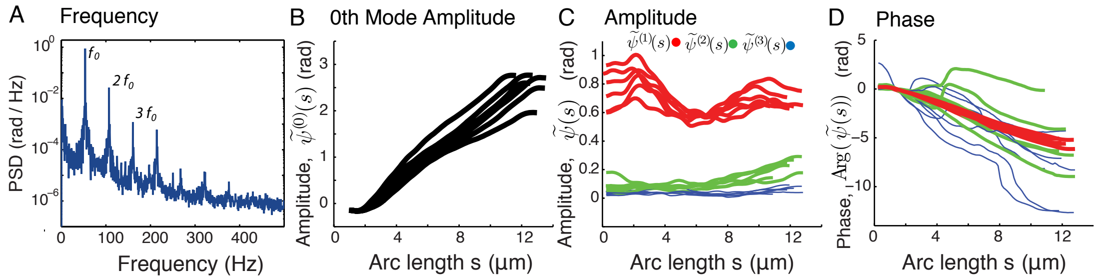

Figure 4.6: Fourier decomposition of the tangent Angle in time. The tangent angle of reactivated wt- axoneme was decomposed in time at each arc-length position. **A** Averaged power-spectral density (PSD) for all arc-length positions of one axoneme. Note that more than 95% of the total power is in the 1st mode. **B** Amplitude of the 0th mode of 6 different axonemes, the mean shape (depicted with red line in Figure 4.5 B **C** Amplitude of the 1st, 2nd and 3rd Forier mode of 6 different axonemes **D** Phase of the 1st, 2nd and 3rd Fourier mode of 6 different axonemes.

Technically, this is done by a home-made Matlab-routine, which performs this evaluation based on the tracking data by: (0) calculating the tangent angle from the shape (1) calculating and subtracting the mean-shape $\widetilde{\psi}^0(s)$ (2) calculating the power spectrum at 100 equidistant points along the arc-length of the axoneme, (3) fitting the 1st, 2nd and 3rd Fourier-modes using a Gaussian and determining frequencies and SD of the frequency peaks, (4) numerically integrating over $6 \cdot SD$ of the Gaussian to calculate the amplitudes (5) calculating the phase at the beat-frequency and its harmonics. The results of this evaluation are presented in Figure 4.6 .

The decomposition of the waveform into arc-length dependent shape-parameters reveals general properties of the beat:

Frequency: The mean-PSD of all arc-length positions is presented in Figure 4.6 A. I find that more than 95% of the total power contributes to the fundamental mode. The higher modes can be resolved but have a minor contribution, which is are <5%. This leads to the conclusion that the oscillation of each point along the arc-length is well approximated by the first temporal Fourier mode.
Mean-shape: A major contribution to the shape has the zeroth mode describing the time independent mean-shape of the beating axoneme. In angular representation it exhibits a linear increase, which describes a shape with constant curvature.
Amplitude: The amplitude of the bend angle is approximately 20% higher at the ends than in the middle, see Figure 4.6 C.
Phase: The phase profile shows a linear decrease with arc-length. The wavelength λ is then given by $\lambda_1 = (2\pi \cdot L)/Arg\psi_{(1)}(L) - Arg\psi_{(1)}(0)$. Then the velocity of wave propagation $v_p = f \cdot \lambda_1$ is a constant. The sign of the slope of the phase or the sign of the wavelength defines the direction of wave propagation that is from the base (s=0) to the distal tip (s=L).

Discussion: The arc-length dependent shape parameters can now be compared to data gained for bull-sperm see, [Riedel-Kruse et al., 2007]. Bull sperm has approximately 6 times the length of a *Chlamydomonas*, axoneme and beats at 1/3 of the beat frequency. The mean curvature is ∼ 50 times lower. Due to the low mean curvature, the shear amplitude is ∼5 times lower while the beat amplitude is similar. In both cases, the wavelength equals approximately the axonemal length. This rough comparison suggests that the main difference between these two waveforms is the circular mean-shape in the case of *Chlamydomonas* which has a much higher curvature.

4.2.2 The 0th and 1st Fourier modes describe the axonemal waveform

Power spectral analysis as performed in Section 4.2.1 shows that the waveform of the reactivated axoneme can be described by the 0th mode $\widetilde{\psi}^{(0)}(s)$ and by the 1st temporal Fourier mode $\widetilde{\psi}^{(1)}(s)$, the fundamental mode of the oscillation. The mean shape $\widetilde{\psi}^{(0)}(s)$ (see Figure 4.5 B/C), shows a constantly increasing angle as evaluated in Figure 4.6 B that describes a circular-arc with a curvature of ~0.25 rad/μm. In Figure 4.7 , I show how a sin-wave with constant amplitude and a wavenumber of 1 superimposed on a circular arc produces a waveform as observed in *Chlamydomonas* WT axonemes. This highlights the fundamental properties of the waveform.

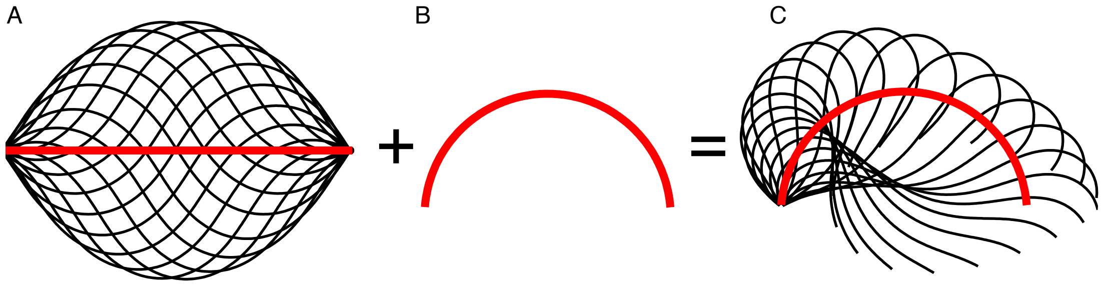

Figure 4.7: Fundamental components of the Chlamydomonas waveform The *Chlamydomonas* waveform is described by the mean-curvature $\widetilde{\psi}^{(0)}(s)$, which has the shape of an circular-arc and by the 1st temporal Fourier mode $\widetilde{\psi}^{(1)}(s)$. The figure shows the shapes gained from Equation 1.1 with ψ being **A** one period of a sin-wave with λ = L, **B** a circular arc with mean-curvature C = 3/L, **C** the sin-wave superimposed onto the circular arc in B. The used values are: amplitude A = 1, wavelength λ = L, mean-curvature C = 3/L.

Averaged shape parameters:
The amplitude of the shape angle, although lower in the middle of the axoneme, can considered to be constant to a first approximation, see Figure 4.6 C. The phase and the 0th mode amplitude are well approximated by a linear function. To define a minimal set of shape parameters, I compute arc-length averaged shape parameters considering the 0th and fundamental mode. The higher modes as well as noise was not considered. The shape parameters are:

(1) mean curvature $C_0 = \partial\widetilde{\psi}^{(0)}(s)/\partial s$.
(2) amplitude $A_1 = \langle|\widetilde{\psi}^{(1)}(s)|\rangle_L$
(3) wavelength $\lambda_1 = (2\pi \cdot L)/(\phi_{(1)}(L) - \phi_{(1)}(0))$,
with L being the length of the axoneme.

Together the shape parameters describe a traveling wave with a constant amplitude over arc-length. Its tangent angle representation is then given by:

$$\psi(s,t) = C_0 \cdot s + A_1 \cos(2\pi f t + s/\lambda_1) \tag{4.4}$$

The xy coordinates of the shapes are then given by Equation 1.1. The set of shape parameters is summarized in Table 4.1.

Table 4.1: Shape Parameters of the reactivated WT axoneme.

WT Units	Length L μm	Frequency f Hz	0th Mode C_1 rad/μm	Amplitude A_1 rad	Wavelength λ_1 μm	N
	11.1±0.7	65±8	0.26±0.02	0.64±0.05	-11±1	13

Shape parameters of WT axonemes reactivated in standard reactivation conditions The values are averages of the data presented in Figure 4.6 . The individual values for the 0th mode and the phase were determined by least square fitting of the data.

Shape reconstruction:
To compare the original and reconstructed shapes for a specific example I calculated the shapes using the arc-length averaged shape parameters in Equation 4.4. The comparison is presented in Figure 4.8.

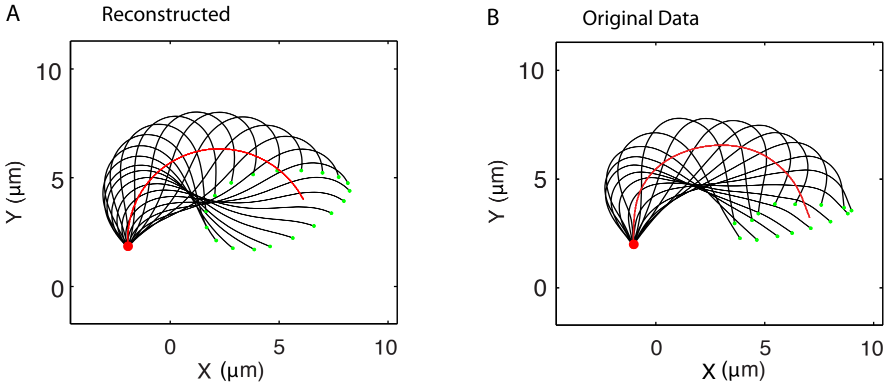

Figure 4.8: Waveform reconstruction using averaged shape parameters. Averaged shape parameters gained by Fourier decomposition were used to reconstruct the waveform of a reactivated wt-axoneme. **A** Waveform reconstruction using averaged shape parameters of a single axoneme: the 0th mode curvature C_0, the first temporal Fourier mode frequency f_1 and amplitude A_1, and the wavelength of the first temporal Fourier mode λ_1, **B** Tracked shapes. The red point depicts the basal end the green points the distal end. The red line represents the mean curvature.

Discussion:
The difference between the symmetric and asymmetric waveform: I have shown that the asymmetric-axonemal waveform can be described by a symmetric wave superimposed on a circular-arc. This property, the underlaying circular arc, gives rise to the breast and recovery stroke-like beat of the *Chlamydomonas* axoneme (compare to Figure 4.7). This shows that although apparently very different the beat of a bull sperm is actually very similar to the beat of a *Chlamydomonas* flagellum with the main difference in a increased mean curvature along with the property that it is constant along the arc-length.

Averaged shape parameters: Figure 4.8 illustrates that the waveform is well approximated by the simplified, arc-length independent shape parameters. Using these parameters I present a waveform parameterization in frequency domain that uses 4 parameters that are, fundamental frequency f_1, 0th mode curvature C_1, 1st mode amplitude A_1 and wavelength λ_1. For further waveform description, I will only consider the 0th and 1st mode.

Comparison of Fourier decomposition to constant curvature model: Compared to the shape description by the constant curvature model by C.Brokaw [Brokaw and Luck, 2005] discussed in the introduction see, Figure 1.12, I present a continuous description with 3 parameters less. The parameters of the two different parameterizations can be compared by the following relations listed in Table 4.2 .

Table 4.2: Shape parameter comparison: Fourier decomposition and constant curvature model.

Parameter	Fourier decomposition	Constant curvature model
Frequency (Hz)	f	f
Mean curvature (rad/μm)	C	$(\kappa_{\mathrm{P}} + \kappa_{\mathrm{R}})/2$ *
Amplitude (rad)	A	$\sigma/2+\mathrm{A}_0$ **
Wavelength (μm)	λ	$\Theta_P/\kappa_P + \Theta_R/\kappa_R$

The constant curvature model was introduced by C. Brokaw and applied to WT cells [Brokaw and Luck, 2005]. A summary of the model is given in Section 1.5 and in Figure 1.12.

*Note that κ_{P} and κ_R have opposite signs.

**Another way of approximating the shear amplitude is by measuring the difference between B2 and B1 as shown Figure 1.12 E. Then, A is given by A=((B2-B1)/2+A_0)

Comparison of averaged shape parameters to literature values: To my knowledge there is no waveform characterization of the isolated *Chlamydomonas* axoneme thus I will compare the gained values to the beat of the flagellum of the intact cell. The shape parameters gained from the constant curvature model for the swimming cell are summarized in Figure 1.12 F and G, the parameters for the isolated axonemes are listed in Table 4.1 .

In the following comparison, the cell data is presented in parenthesis. The beating frequency f of axoneme and (cell) is equivalent, 65±8 Hz, (63.4±1.1 Hz). The length of the specific cell attached axoneme is larger 11.1±0.7 μm, (14 μm). As I will show in Section 4.2.3 4.4.1 , 4.4.2 the normalized wavelength v is a constant for the WT axoneme with $v= \lambda/\mathrm{L} \sim 1$. Since the length L of the cell bound flagellum is greater, we expect it to have a larger wavelength λ with the same ratio v. This is what we find for the wavelength λ -11±1 μm, (-15.6±2 μm). The mean curvature C of the cell is slightly lower than the axonemal with 0.26±0.2 rad/μm, (0.22±0.02 rad/μm). In the considered case the beating amplitude of the wave is larger than for the isolated axoneme 0.64±0.05 rad, (1.0±0.2 rad). In this definition the beat amplitude is highly dependent on the measurement of the maximal basal angle, which is difficult to measure for the cell.

In summary, the shape parameters of the two different descriptions are comparable, which means that (1) the presented Fourier description is applicable and comparable to previous work and (2) that the waveform of the isolated axoneme is very similar to the waveform of the flagellum attached to the cell. In both cases, the shape-determining feature is the constant mean-curvature. The question that herewith arises is: What axonemal component is actually responsible for the mean shape. Among others, I will discuss this question in the Section 4.4.

4.2.3 General dependence of shape parameters on axoneme length and beat frequency.

Axoneme length and beat frequency are characteristic parameters that define the beat of the axoneme in different ways: Consider the axoneme to be an actively bending rod with distributed force generators that act according to a force velocity relationship. The dimensions of the structure and the motor activity are correlated because a longer and faster moving structure experiences a higher drag that then reflects back on the motors by slowing them down. Here I test for correlation between the shape parameters to see if these general ideas apply.

Since I find a quite considerable variability in beat frequency and axoneme length, I present the dependence of the shape parameters as a function of these parameters in Figure 4.9. I use data of 130 axonemes and perform a linear least square fit on the different dependencies. To test for correlation, I ask whether the slope of the fit is significantly different from zero by performing a t-test on a 95% confidence level on the slope of the fitted line considering its standard deviation.

Beat frequency: I find that longer axonemes beat at lower frequencies, see Figure 4.9 A. The faster an axoneme beats, the lower is its beating amplitude, see Figure 4.9 F. The mean curvature and the wavelength of the axoneme do not show frequency dependence as shown in Figure 4.9 E and G.

Axoneme length: The mean curvature decreases with axoneme length, see Figure 4.9 B. The dependence is linear implying that the average shear angle at the end $\langle\Psi_s(L)\rangle = \langle\psi(L) - \psi(0)\rangle$ is a constant irrespective of length. For the reactivated WT axoneme, I find values of $\langle\Psi_s(L)\rangle$ = 2.4±0.4 rad (mean±SD, N=130), which shows that the mean-shape is a circular arc with $\sim$ 2.4 rad. The wavelength shows a linear dependence on the length, see Figure 4.9 D. This means that the normalized wavelength v, the number of waves per axoneme length, is a constant v = λ/L = const. For the reactivated WT axoneme, I find v = 1.02±0.06 (mean±SD, N=130).

Discussion: The relations between shape parameters reveal general properties of the oscillator: A longer axoneme experiences a higher drag force at its end. An explanation for this could be that increased hydrodynamic load slows motors down and hence leads to a slower beat. The same idea could apply to the amplitude. When an axoneme beads faster, its beating amplitude could be limited by the counteracting hydrodynamic forces. An interesting result is the linear decrease of the mean curvature with axoneme length.

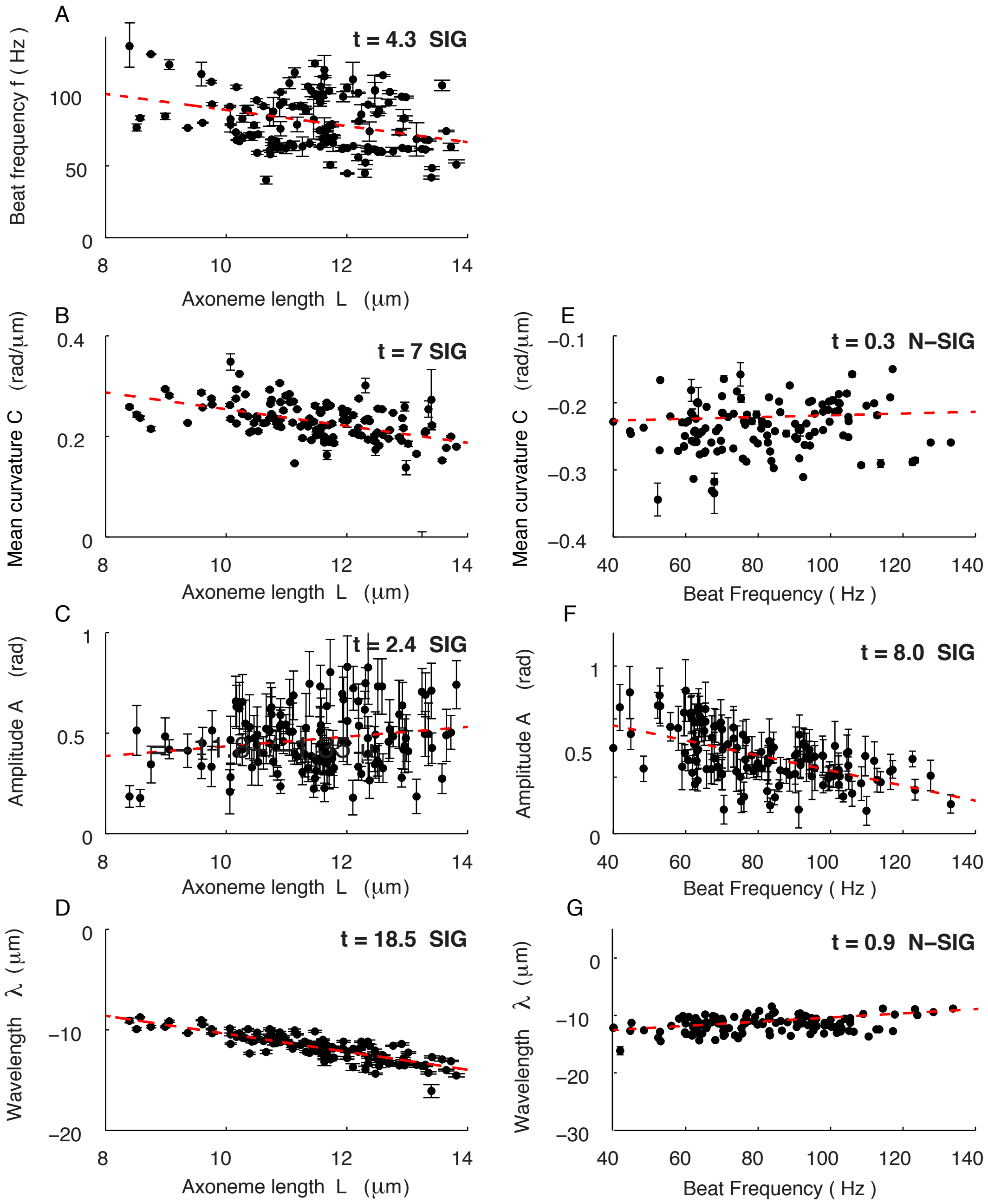

Figure 4.9: Beat frequency and axoneme length dependence of averaged shape parameters of wt axonemes. The averaged shape parameters are extracted from 130 wt axonemes reactivated in standard reactivation conditions in the presence of 0.5-1mM ATP. Parameters are presented as a function of beat frequency and axoneme length. The dashed red line represents a weighted least square fit of the data. A statistical test (students-t test on a 95 % confidence level ($p<0.05$)) was performed to ask if the slope of the fit is significantly different from zero. The result of this analysis is shown in the right-upper corner of each panel A-G (t-value and the test result: SIG/N-SIG for significant and non-significant from zero).

This means that the mean shear angle at the end is a constant. Since the shear angle is proportional to the amount of sliding in the structure, this implies that the mean-sliding displacement at the end of the axoneme is a constant $\langle\Delta(L)\rangle = a\,\langle\psi(L)-\psi(0)\rangle = a\,Cl = const.$ If the sliding displacement is a measure for how many motors contribute to the sliding this could mean that the number of activated motors, which contribute to the mean curvature is a constant. It could also mean that the balance of motor forces is stable giving rise to a constant offset.

4.2.4 The isolated axoneme is a good model for the intact flagellum

In this section I analyze the waveform of the intact *Chlamydomonas* wt-cell using the shape analysis presented in Section 4.2.1 and compare it to the waveform of the isolated axoneme. I discuss how the waveform determines the swimming behavior of the cell. The *Chlamydomonas* cell uses the coordinated beat of its two flagella to swim. Freely swimming cells usually swim with mean velocities of ∼150 μm/s. During forward movement the cells rotate counterclockwise about their long axis with a frequency of 1.4-2 Hz (maximum 2.5 Hz)[Rüffer and Nultsch, 2005]. The cell rotation makes it extremely difficult to observe multiple beats in the image plane. To circumvent this problem, I use chambers with a hight of 5-10 μm, which is comparable to the diameter of the cell. Cells that swim in these thin chambers exhibit an up to 20x lower swimming velocity and a reduced beat frequency of ∼30 Hz, most likely due to wall effects. In this assay cells do not rotate allowing for precise shape tracking [Geyer et al., 2013].

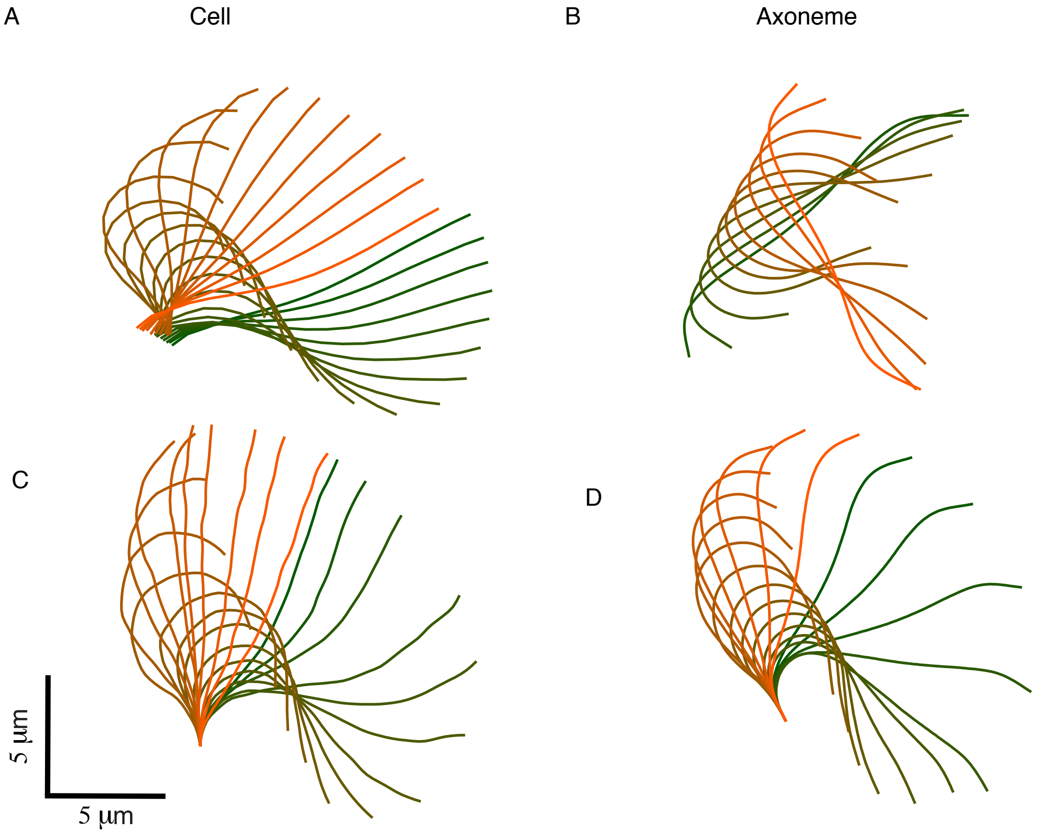

Figure 4.10: Flagella and axonemal waveforms. Sequence of flagella and axonemal shapes during one beat cycle. **A** Flagellar waveform of a swimming *Chlamydomonas* cell. Cells were imaged in shallow chambers using Phase-Contrast microscopy. The last 2 μm of the flagella was discarded. In most cases the discarded part was a straight continuation of the presented shape. **B** Waveform of a free swimming axoneme reactivated in standard conditions. **C** Shapes of A aligned to the 1st angle. **D** Shapes of B aligned to the 1st angle. The time interval between adjacent shapes is 2 ms. The progression of shape in time is color-coded from green to orange.

Although the main part of the flagellum is in focus, the distal tip (last 2 distal microns) often leaves the focal plane which hints towards a slight 3 dimensional component of the beat. In Figure 4.10 A and B the waveforms of a cell attached flagellum and a reactivated axoneme are presented.

Waveform Comparison: The beat of the cell bound flagellum and the isolated axoneme is characterized by a breast-stroke like phase in which the cell swims forward and recovery-stroke in which the cell is slightly pushed backwards. Shapes of the breast stroke phase have low mean curvature while the mean curvature during the recovery strike is high. Figure 4.10 A shows this behavior on the example of the cell bound flagellum, in Figure 4.11 A 1-3 breast and recovery stroke are depicted separately.
Although both the axoneme and the flagellum go through a similar series of shapes during the beat cycle, their movement is different since both experience different hydrodynamic forces due to the different boundary conditions, see Figure 4.10 A and B. The cell bound flagellum is strongly attached to the basal body, which is comparable to a clamped end. The synchronized 2nd flagellum produced a counteracting force and prevents cell body rocking. The reactivated axoneme has free ends and thus rotated during the beat. Hydrodynamic forces counteract the motor forces in the flagellum either (1) alter the shape of the axoneme or (2) slow down the beat. To separate the swimming path from the shape, I present a time-series of a cell attached flagellum and an axoneme aligned to the first angle $\psi(0)$ in Figure 4.10 C and D. In this representation the waveform of the cell and the axoneme is comparable and appears to be very similar.

One of the apparent differences between cell and isolated axoneme is the shape of the distal end: In the cell-bound case the distal end is straightened out throughout the whole breast stroke and even counter-bends. However, the isolated axoneme stays curved throughout the whole breast-stroke. Compared to the isolated axoneme the cell bound flagellum experiences a higher drag force at the distal tip as it is displaced with the higher velocity with respect to the fluid.

The typical flagellar speed during the beat-cycle:
To characterize the progression of shapes during the beat I define a proxy for the phase of the beat cycle using the tangent angle in the middle position of the flagellum $\psi(L/2)$. I also define the typical flagellar speed with $\partial\psi(L/2)/\partial t$. The flagellar speed over one beat cycle is presented in Figure 4.11. I observe 2 phases of maximal velocity: one in the recovery stroke, the period of highest flagella curvature, see Figure 4.11 (1-2) and one during the breast stroke during the period of lowest flagellar curvature, see Figure 4.11 (1-2).

Recovery stroke: The maximal flagellar speed during the recovery stroke is twice as high as during the breast stroke. Although the beat frequencies of cell and axoneme differ by a factor of 2, the cell bound flagellum and the axoneme have comparable maximal speeds during the recovery stroke shown in Figure 4.11 (1-2). The cell spends a smaller portion of the beat cycle in the recovery stroke compared to the axoneme. The average flagellar speed of the axoneme or the rate at which it changes shape, is therefore higher.

Breast stroke: The maximal flagellar speed during the breast stroke is higher for the isolated axoneme, see Figure 4.11 (3). At the onset of the breast stroke, where the cell bound flagellum experiences the highest hydrodynamic force, the flagellar speed of the isolated axoneme is >4 times higher compared to the cell bound flagellum. Here, the cell spends a larger portion of the beat cycle in the breast stroke compared to the isolated axoneme. The average flagellar speed of the axoneme or the rate at which it changes shape, is also higher during the breast stroke.

Taken together this shows that the cell bound flagellum spends a greater portion of its cycle time for performing the breast stroke. The reason for this is most likely the higher drag, which the flagellum experiences at its tip. As shown in Figure 4.10 C, the distal tip of the flagellum is bend backward, most likely by the fluid forces. This is not the case for the isolated axoneme in Figure 4.10 D. If in the case of a clamped cell fluid forces mainly slow down the breast stroke of the beat, the axoneme spends more time in a low curvature shape. This should effectively decrease the mean curvature.

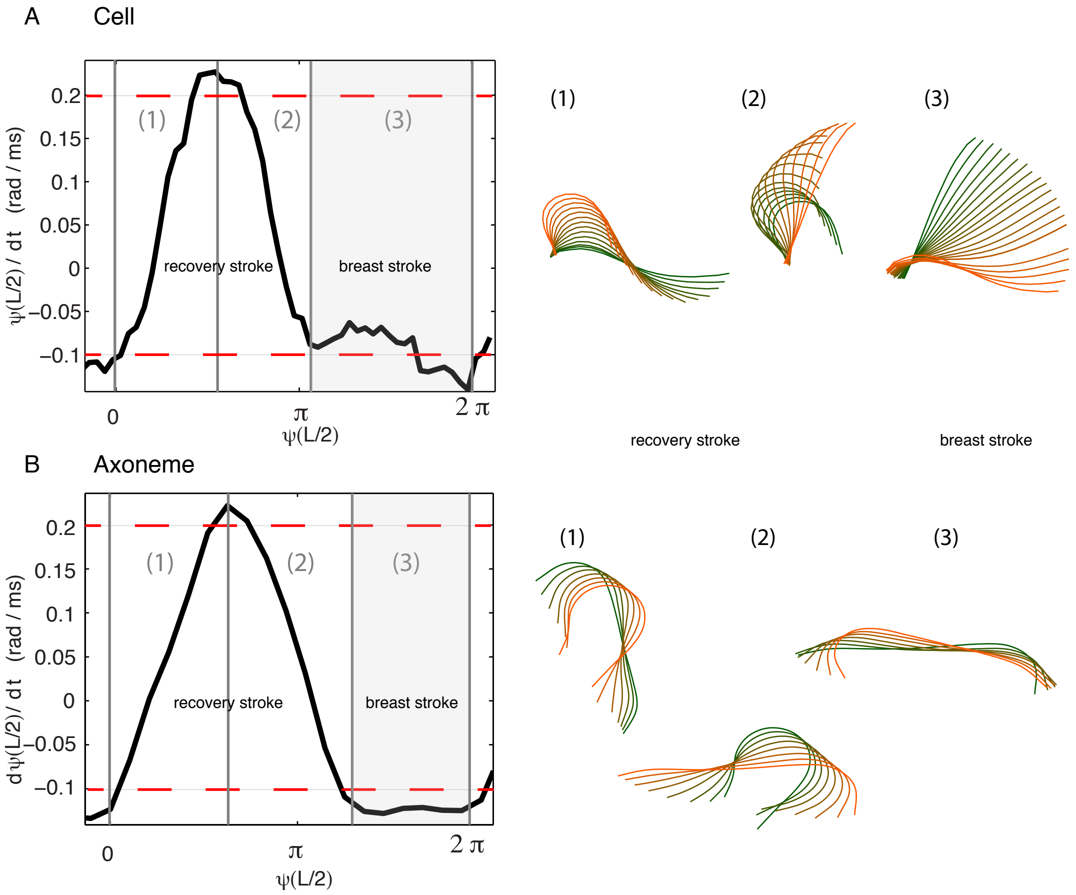

Figure 4.11: Typical axonemal and flagellar speed during the beat cycle. I define a proxy for the phase of the beat cycle using $\psi(L/2)$ and define the typical flagellar speed as $\partial\psi(L/2)/\partial t$. Phases of the beat are divided into breast (number 1-2) and recovery stroke (number 3). **A** Cycle-speed of a cell bound flagellum. The beat frequency was 30 Hz. The cell was swimming in a shallow observation chamber. **B** Cycle-speed of a reactivated axoneme. The beat frequency was 60 Hz. The time interval between adjacent shapes is 1 ms. The progression of shape in time is color-coded from green to orange.

Waveform parameterization of the cell attached flagellum: To compare the waveforms of cell and axoneme I analyze the beat of WT cells swimming in shallow observation chambers. In Figure 4.12 I present the shape analysis of the WT-cell and isolated axoneme and in Table 4.2.4 I show the averaged arc-length dependent shape parameters.

I find that the following characteristics:

0th mode: In both cases, cell and axoneme the 0th mode $\widetilde{\psi}^{(0)}(s)$ describes a circular arc. The mean curvature of the beat is smaller for the cell.

Frequency: I compare the integrated power of the mean PSD for the 1st and 2nd Fourier modes. I find that in the case of the cell bound flagellum 10-15% of the total power accumulates in the second mode while in the isolated axoneme the second mode contains only <3% of the total power.

Amplitudes of dynamic Fourier modes: In both cases the spatial mean of the amplitudes is very similar although cell and axoneme exhibit a different arc-length dependence: While the amplitude of the fundamental mode $\widetilde{\psi}^{(1)}(s)$ of the freely swimming axoneme is highest at the base, the amplitude of the cell-bound flagellum is lowest at the base where its amplitude is decreased by the attachment to the cell body. The amplitude of the second mode $\widetilde{\psi}^{(2)}(s)$ is significantly increased in the cell. While it increases on the most distal 5μm in the axoneme, it is 2-3x increased in the cell throughout the entire arc-length.

Phase: The arc-length dependent phase of the 1st mode $Arg\,\widetilde{\psi}^{(1)}(s)$ is monotonically decreasing with arc-length in both cases. The negative slope shows that in both cases the wave propagates from base to tip, see Section 4.2.1. The wavelength is 2 times larger for the cell.

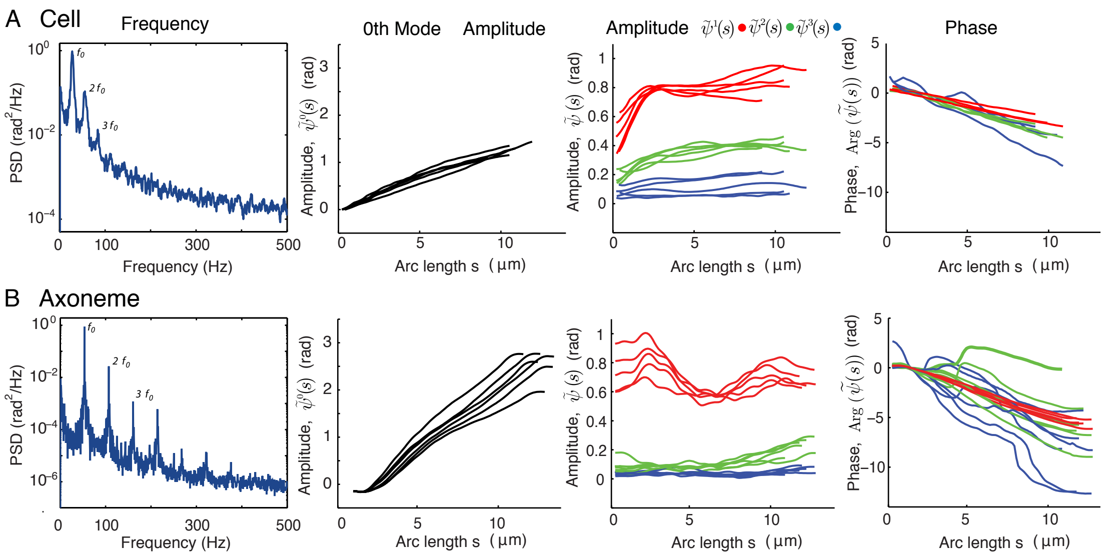

Figure 4.12: Shape Analysis of cell attached flagella. The waveform of cell attached flagella was recorded in shallow observation chambers and analyzed using Fourier methods as described in Section 4.2.1. **A** Waveform analysis of the cell-attached flagellum. In the assay I did not distinguish between the cis /trans flagellum since the eye-spot could not be identified. **B** Waveform analysis of the isolated axoneme.

Table 4.3: Shape Parameters of the reactivated WT axoneme.

	Length L μm	Frequency f Hz	0th Mode C rad/μm	Amplitude A rad	Wavelength λ μm	N
Axoneme	11.1±0.7	65±8	0.26±0.02	0.64±0.05	-11±1	13
Cell	11±1	30±7	0.14±0.01	0.74±0.1	-19±4	6

Shape parameters are averages of the data presented in Figure 4.12Ṫhe data describes WT axonemes reactivated in standard reactivation conditions and WT cells observed in shallow observation chambers. The individual values for the 0th mode and the phase were determined by least square fitting of the data Values are (mean±SD).

Discussion: I analyzed the waveform of flagella of cells, which are trapped in shallow observation chambers and compared them to those of isolated axonemes. Here the movement of the cell body is strongly attenuated since it is squeezed between two glass surfaces. In this situation, one end of the flagellum can be considered to be clamped and thus the boundary conditions are greatly different compared to the free moving isolated axoneme. These conditions cause different hydrodynamic loading situations for the axoneme during the beat. Consequences of this loading are likely to give rise to waveform differences I find by comparing the isolated axoneme to the cell bound flagellum. There are two major differences: The cell bound flagellum spends a larger portion of the beat cycle in the breast stroke where the flagellar speed is low. During this phase of the beat, the distal end of the flagellum is straightened out and even counter-bended which could be an indication for the high viscous drag force. These differences in shape and timing of the beat also reflect back onto the shape parameters. The cell bound flagellum shows a decreased mean-curvature. This can be understood as the flagellum spends a larger portion of the beat cycle performing the breast stoke, where the flagellar speed is low and the shape has a low mean curvature. Additionally, the increased viscous forces on the distal tip counteract the motors, which perform the principle bend and thus reduce the mean curvature even further. This can be observed at the described counter-bend at the distal tip. This change in shape might also count responsible for the increased wavelength that I detect for the cell bound flagellum. The slow down during the breast-stroke introduces an asymmetry in timing of the beat and thus could be responsible for the increased 2nd mode that I detect. These possibilities are investigated in detail in ongoing studies. As discussed in Section 4.8 the shape parameters gained from axonemes of freely swimming cells [Brokaw and Luck, 2005] are very similar to the parameters gained for the isolated axoneme. Consistently with this study I find that the cell bound flagellum exhibits an increased beat amplitude and a decreased mean curvature. It would be interesting to investigate these trends using theoretical modeling, which is part of ongoing work.

Comparing the beat-amplitudes of the cell and axoneme is difficult due to the different boundary conditions. However, comparable is the shear amplitude, which is shown in Figure 4.13 and is here represented as the amount of local sliding. The maximal amount of shear as a function of arc-length is calculated by summing the 0th and 1st mode amplitude and multiplying it by the diameter of the axoneme . This calculation assumes no sliding at the base. I find that there is less sliding along the cell bound

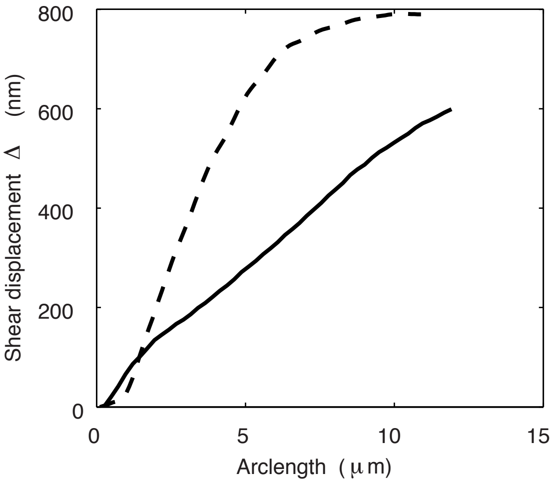

Figure 4.13: Maximal shear displacement. The maximal shear displacement Δ was calculated for a representative reactivated axoneme (dashed line) and for typical cell attached flagellum (solid line) by the following formula: $\Delta = \widetilde{\psi}^{(0)}(s) + \widetilde{\psi}^{(1)}(s) \cdot a$ with a = 200 nm being the diameter of the axoneme. This calculation assumes that there is no sliding at the base.

flagellum compared to the isolated axoneme as given by Equation 1.2 . This fits into the picture that increased hydrodynamic loading counteracts bending and thus sliding inside the axoneme.

The mean shape of the flagellum determents the direction of swimming of the cell In Section 4.3.1 I have shown that the asymmetry of the beat that is described by the mean-shape determines the path curvature of a isolated axoneme. This implies that the direction of the propulsive force depends on the mean curvature. This has implications for the propulsion of the micro-swimmers: Although the direction of wave propagation is the same for sperm cells and *Chlamydomonas* cells, they swim in different directions. The sperm swims head in front, *Chlamydomonas* is dragging its cell body. Responsible for this swimming behavior is the asymmetry in the beat of the two synchronized flagella. The mirror symmetric arrangement of the two flagella and the synchronized beat drags the cell body through the fluid. *Chlamydomonas* has a second mode of swimming: the photo-trophic response or escape mode. In this mode the direction of swimming is reversed. The mean curvature in this case of the beat is very small [Brokaw and Luck, 2005] . The flagellar beat pushes the cell body forward. This shows that the cell regulates its mean-curvature to reverse it's swimming direction. It also implies that the there must be some intermediate curvature where the forward swimming of the cell is strongly attenuated. In this respect it would be worthwhile to revisit motility defective mutants, which potentially could exhibit a normal beat with an intermediate mean-curvature.

4.2.5 Summary:

In this section I showed that Fourier decomposition in time is a good tool to parameterize the *Chlamydomonas* waveform. I show that the shape is well described by the 0th and the 1st Fourier modes. I find that the 0th mode is a semi-circular arc of 4/5 π rad. This property is not dependent on the total length of the axoneme. I furthermore show that a constant 1st mode amplitude, a constant wavelength and a constant curvature of the 0th mode define a set of shape parameters. I compare these shape parameters to literature values gained with an alternative shape parameterization and find good agreement between the waveform of isolated axoneme and cell bound flagellum. I use the introduced shape parameterization to compare the waveform of the isolated axoneme to the cell-bound flagellum. I find that the beat shows the same properties although the boundary conditions alter the amplitude and the wavelength.

4.3 The circular motion is a consequence of the axonemal waveform

4.3.1 Hydrodynamic relations for small amplitude waves explain the relation between swimming and shape of axonemes

When the axoneme beats it hydro dynamically interacts with its surrounding. This interaction influences the axonemal shape and the resulting waveform that determines the swimming path. To illustrate how the waveform of the axoneme is tied to its swimming I consider a set of simplified hydrodynamic relations, which characterize the propulsive effect of small amplitude waves and have been derived by J. Gray and G.J. Hancock [Gray and Hancock, 1955]. This simplification of the hydrodynamics assumes that (1) the amplitude of the wave is small and (2) the length of the axoneme L is approximately equal to the wavelength λ of the traveling wave $L = \lambda$. The relation between swimming velocity v and the characteristic wave-parameters frequency f, amplitude A and wavelength λ is then given by:

$$v = c_0 \lambda f A^2 \tag{4.5}$$

The proportionality constant c_0 relates to the ratio between the normal and tangential friction coefficients $\xi_{n/t}$:

$$c_0 = \frac{1}{2(\frac{\xi_n}{\xi_t} - 1)} \tag{4.6}$$

The ratio of drag coefficients $\frac{\xi_n}{\xi_t}$ for a cylinder near a plane surface has shown to be 2 [Howard, 2001, Hunt et al., 1994] and has been determined experimentally to be 1.8 for bull sperm cells swimming close to a boundary [Friedrich et al., 2010]. Using similar considerations the relation between the rotational frequency f_{rot} and the characteristic wave-parameters frequency f, amplitude A, wavelength λ and mean-curvature C is then given by:

$$f_{rot} = c_1 C \lambda f A^2 \tag{4.7}$$

The radius of the swimming path r_0 and the path curvature k is then given by:

$$r_0 = v/2\pi f_{rot} \qquad k = 1/r_0 \tag{4.8}$$

By plugging in Equation 4.7 into Equation 4.5 one finds that the ratio of the path curvature k and the mean-flagellar curvature C is given by:

$$\frac{k}{C} = \frac{2\pi c_1}{c_0} \tag{4.9}$$

Testing the hydrodynamic relations with experimental data: In this study I use a standard reactivation assay to test the relations stated in Equation 4.5 and Equation 4.7. A standard reactivation assay provides enough variability so that the parameter space is sampled sufficiently (see beat frequency distribution figure 3.13 for comparison). Equation 4.5 and Equation 4.7 consider the specific case where the length of the axoneme L is approximately equal to the wavelength λ. This is a valid assumption in our case as shown in Section 4.2.3. To calculate the swimming velocity I assume that the reactivated axoneme swims on a circular path. I determine the path radius r_0 from the averaged trajectory of the basal end of the axoneme as shown in Figure 4.14 by least-square fitting of a circle. The path curvature k is then given by the radius r_0 and

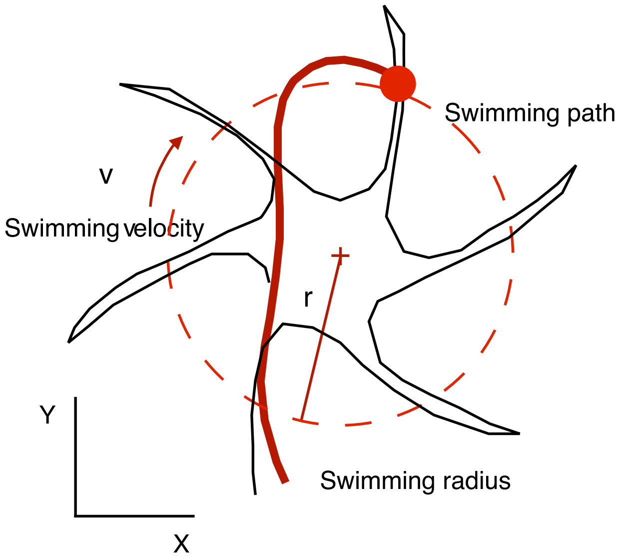

Figure 4.14: Swimming path of the axoneme. The average swimming path (pink dashed line) was calculated from the trajectory of the basal end of the axoneme depicted with a red dot (axoneme, red solid line). The path-radius r was calculated from a circular least square fit of one rotation averaged over 120-180 rotations. The path curvature is given by $k = 1/r$, the swimming velocity is given by $v = 2\,\pi\,r\,f_{rot}$ with f_{rot} being the rotational frequency as defined in Equation 4.1.

the swimming velocity v is given by Equation 4.8. Note: The selection of the swimming path is arbitrary and was defined similar to [Friedrich et al., 2010]. Choosing another definition e.g. the center of mass of the shape, a different path radius will be gained.

The simplified hydrodynamic equations can now be tested with experimental data extracted from a standard reactivation assay. To determine the proportionality coefficients between the different parameters, I perform a linear regression for the various dependencies as shown in Figure 4.15. I find that the experimental data can indeed be described by the simplified hydrodynamic relations. I determine the proportionality coefficients with $c_0 = 0.58 \pm 0.1$ and $c_1 = 0.1 \pm 0.02$. These coefficients determine two important properties of the swimming axoneme: (1) the ratio of drag coefficients for the isolated axoneme is given by c_0 with $\frac{\xi_n}{\xi_t} = 2.17 \pm 0.19$, (2) the ratio of path to mean-flagellar curvature is given by the ratio of c_0 and c_1 with $\frac{k}{C} = 1.07 \pm 0.04$.

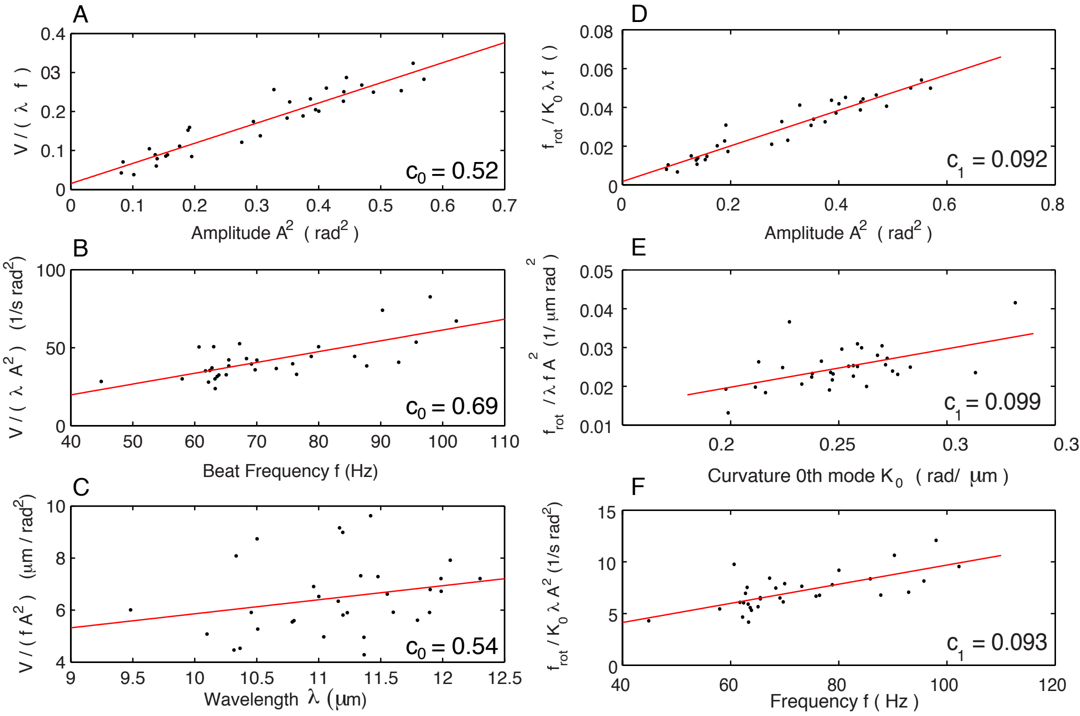

Figure 4.15: Test of hydrodynamic relations for small amplitude waves. The proportionality coefficients have been determined by a least-square fit of Equation 4.5 (A-C) and Equation 4.7 (D-F). **A** Dependence of swimming velocity on the beating amplitude. **B** Dependence of swimming velocity on the beat frequency. **C** Dependence of swimming velocity on the wavelength. **D** Dependence of the rotational frequency on the beating amplitude. **E** Dependence of the rotational frequency on the mean curvature. **F**. Dependence of the rotational frequency on the beat frequency. The mean values of the coefficients are $c_0 = 0.58 \pm 0.1$ and $c_1 = 0.1 \pm 0.02$ (mean±maximal error) considereng the uncertainties of the slopes of the linear fits. The coefficients characterize the ratio of normal to tangential friction coefficients with $\frac{\xi_n}{\xi_t} = 2.17 \pm 0.19$ calculated using Equation 4.6 and the ratio of path to mean-flagellar curvature with $\frac{k}{C} = 1.07 \pm 0.04$ calculated using Equation 4.9.

Discussion: I have shown that the simplified hydrodynamic relations for small amplitude waves can be applied to characterize the dependence of the shape parameters and the swimming behavior of the axoneme. In essence these equations show that: (1) propulsion needs non-isotropic drag coefficients since for isotropic drag coefficients $\xi_n = \xi_t$ the translational speed is zero. (2) the translational and the rotational speeds scale linearly with the beat frequency and are proportional to the square of the amplitude of the beat. (3) the rotation is bound to a non-zero mean curvature: Zero mean curvature causes straight swimming. The radius of the swimming path is determined by the mean-shape of the axoneme as shown in the Equations 4.7/4.5. In Figure 4.16 I show that this assumption is well supported by the experimental data from which I consistently determine the proportionality coefficient by least square fitting with $\frac{k}{C} = 1.07 \pm 0.04$. A nearly linear dependence between path and flagellar mean curvature has also been predicted theoretically using resistive force theory (RFT) [Friedrich et al., 2010]. In experiments, the authors analyzed bull sperm cells swimming close to a surface and found a proportionality factor of 2.2. Using predictions from RFT the authors showed that friction of the sperm head increases this proportionality factor in general. This explains a lower value for the isolated axoneme where no friction

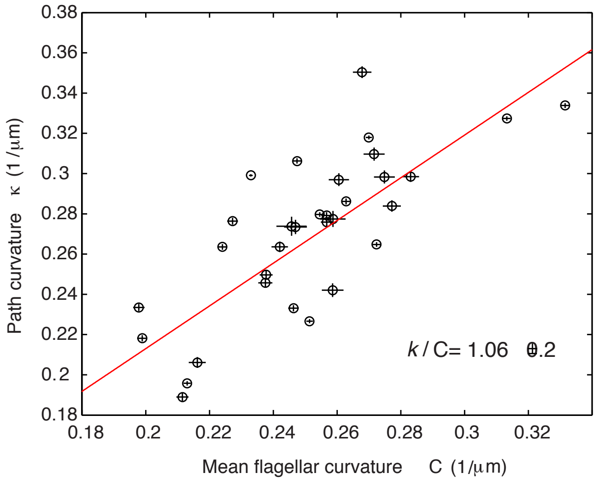

Figure 4.16: The mean flagellar curvature determines the swimming path. Linear fit of the path curvature over the mean flagellar curvature through the origin. The path curvature k scales approximately linearly with the mean flagellar curvature C, with a proportionality factor $k/C =$ 1.06±0.2 (Least square fit ± 95% conf.bounds). For this study wt axonemes in standard reactivation conditions were considered (N=32)

producing head is present.

Using Equation 4.6 I find that the ration of friction coefficients $\frac{\xi_n}{\xi_t} = 2.17 \pm 0.19$. Theoretically, its expected that this ratio is smaller than 2, which is the limit value for an infinitely thin cylinder [Howard, 2001, Hunt et al., 1994]. My calculated value is consistent with that.

4.3.2 The swimming path can be reconstructed using shape information and a hydrodynamic model

In Section 4.2.2 I present a waveform-simplification that I will now use to reconstruct the swimming path. The hydrodynamic model I use is Resistive Force Theory (RFT), which was introduced by [Gray and Hancock, 1955]. This model neglects long-range hydrodynamic interactions and therefore is suitable to describe swimming in close proximity to surfaces, where such long-range hydroydnamic interactions between different parts of the flagellum are partially screened. The agreement of the data with the reconstructed swimming path is a measure for (1) how well the shape simplification describes the waveform and (2) how good the hydrodynamic model works. The implementation of RFT was done by Pablo Sartori.

The first consideration we make is that the sum of all forces the axoneme exerts on the fluid has to be zero, since no external forces are acting on a freely swimming object [Gray and Hancock, 1955, Jülicher and Prost, 2009].

$$\int_0^L f_{fluid}\ \ ds = 0 \tag{4.10}$$

To calculate the forces on the fluid exerted by a moving slender rod we use RFT and treat tangential and normal velocities $v_{n/t}$ and friction coefficients $\xi_{n/t}$ separately:

$$f_{fluid} = \mathbf{v}_n \xi_n + \mathbf{v}_t \xi_t \tag{4.11}$$

To calculate the tangential velocity field $\mathbf{v}_t$ we calculate the tangential vector-field $\mathbf{t}(s,t)$ from the pointing vector $\mathbf{r}(s,t)$ as its arc-length derivative $\mathbf{t}(s,t) = \partial_s \mathbf{r}(s,t)$. The tangential velocity field is then given by $\mathbf{v}_t = \mathbf{t} \cdot \partial_t \mathbf{r}$, the normal velocity field is gained in an analogous manner. The velocity $\mathbf{v}_0(t)$ with respect to the lab frame is gained from solving the force balance equation at every instant in time. Therefore, I use the ratio of friction coefficients $\frac{\xi_n}{\xi_t} = 2$, which I obtained in Section 4.3.1. The swimming path is then calculated by integrating the velocity using an Euler step $\mathbf{r}(0,t+dt) = \mathbf{r}(0,t) + \mathbf{v}_0(t)dt$. The path reconstructions and experimental data are shown side by side in Figure 4.17.
Note: The path is a pure reconstruction using the fluid model RFT, the simplified shape described by the averaged shape parameters and the ratio of friction coefficients determined in Section 4.3.1.

Discussion: The comparison of the experimentally gained data to the reconstructed swimming path of reactivated axonemes shows very good agreement. This shows that the shape description by the averaged shape parameters is reasonable simplification of the axonemal beat. It also implies that the fluid model RFT captures the fluid properties in the considered situation.

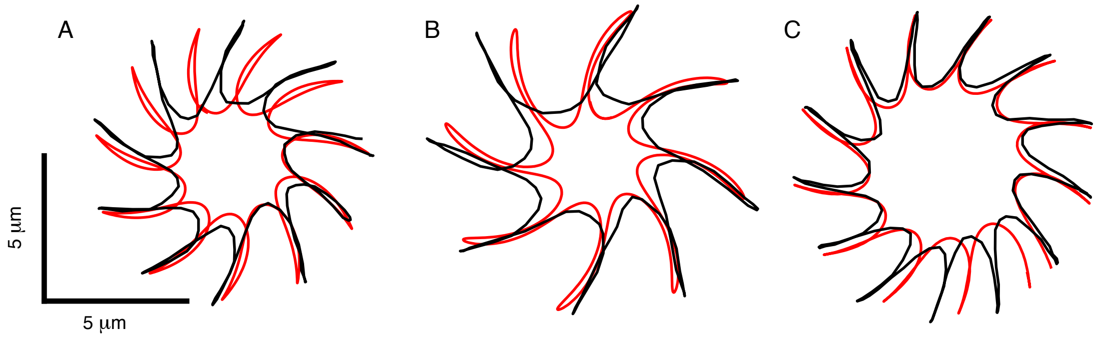

Figure 4.17: Reconstruction of the swimming path using RFT. Using Resistive Force Theory the swimming path of wt axonemes reactivated in standard reactivation conditions was reconstructed using the shape parameters gained as described in Section 4.2.2 and the ratio of friction coefficients $\frac{\xi_n}{\xi_t} = 2.0$ estimated in Section 4.3.1. The lines depict the trajectories of the first point of the axoneme. Black is the original data, Red is the trajectory reconstructed from frequency domain parameters. Presented are 3 example-axonemes with the following waveform parameters: **A** f=62.5 Hz, C_0=0.26 rad/μm, A=0.67 rad, λ=-11.2 μm, L=12 μm, f_{rot}=7.7 Hz **B** f=62.7 Hz, C_0=0.22 rad/μm, A=0.54 rad, λ=-11.0 μm, L=11 μm, f_{rot}=5.0 Hz **C** f=65.1 Hz, C_0=0.28 rad/μm, A=0.66 rad, λ=-10.1 μm, L=11 μm, f_{rot}=5.9 Hz.

4.3.3 Motor mutations alter the direction of rotation of reactivated axonemes

Isolated WT axonemes reactivated in a flow chamber approach at the surface as they rotate. Over time the number of axonemes in a field of view increases and reaches a maximum. The reason for that observation is the 3 dimensional component in the beat that causes the axonemes to swim on a helical path, which eventually directs them to one or the other surface.

Since the beat of the reactivated axoneme appears to be planar as observed in the light microscope, the out of plane component has to be in the order of the depth of field. An approximation for the depth of field d is $\sim 1\mu$m where $d = 2\lambda n/NA^2$ with λ being the wavelength of the illuminating light, n the refractive index of the surrounding media and NA the numerical aperture of the objective.

An indication for a 3 dimensional beat comes from the observation that intact WT cells perform a counterclockwise (ccw) rotation with a frequency of 1.4-2.5 Hz around their long axis as they swim forward [Rüffer and Nultsch, 2005]. This rotation can be understood when considering that the left and right flagellum are identical and attached to the cell in such a way that their minus ends point towards the cell body. To have them bend into opposite directions one of them is rotated 180° around its long axes with respect to the other, see Figure 1.7. When the axonemal beat exhibits a force component that is directed normal to the beating plane, this force component will have different signs for the flagella attached with opposite orientation, which then rotate the cell as depicted in Figure 4.18 A. From the direction of the rotation one can now predict the direction of the out of plane component of the beat, and thus the expected direction of rotation of the axoneme when isolated from the cell. Since the arrangement of the doublet microtubules in the flagellum with respect to the cell body is known, I can even tell the position of the motors in the axoneme, which are most likely responsible for the 3d component of the beat.

Predicted rotational frequency of the cell. Since the beat of the isolated axoneme appears to be planar in light microscopy images, the z components must have a magnitude of 1 μm or less. Assuming that the z displacement d_z of the flagella between base and tip is 1 μm per beat cycle at a flagella length L of L=10μm it would take approximately 60 beats for a full rotation of the cell. At a beat frequency of 60 Hz the rotational frequency f_r would then be approximately $f_r = 1\,\text{Hz}$, which is in agreement with the reported valued for the rotation frequency of the WT cell. From the tracking of cell attached flagella I know that cell bound flagella exhibit a stronger z component since I never managed to track the last 2 distal μm over a full beat cycle. Assuming a 2μm out of plane component for the cell, which is reasonable, the reported rotational frequencies can be explained.

Predicted sense of rotation of reactivated axonemes on the surface: As shown in Section 4.1.2 the direction of wave propagation of WT axonemes is from the base to the tip, which defines the swimming direction of the axoneme that is opposite to the direction of wave propagation. A 3-dimensional component added to a planar beat will result in a helical swimming path. Since the left and right flagellum are identical both flagella should have a swimming path with equal handedness and a common direction of rotation on the surface. The idea is that a motor-force component normal to the beating plane bends the axoneme in certain phases of the beat, which leads to a non-zero mean curvature in z direction as depicted in Figure 4.18 A. The swimming path is now defined by (1) the direction of wave propagation (2) the mean curvature of the axoneme in the xy image plane and (3) the mean curvature in the z direction. Following these considerations, the predicted sense of rotation of an isolated axoneme viewed form above onto a surface would be ccw as depicted in Figure 4.18 A.

Sense of rotation of WT axonemes: In a flow chamber reactivated WT axonemes are only found on the chamber surfaces and not in the bulk fluid. WT axonemes reactivated with 0.5-1 mM of ATP and ATP regenerating system show ccw-rotation on the lower surface. On the upper surface all of the axonemes rotate clockwise. However, when the ATP concentration is between 50 and 400μM up to 18% of the axonemes exhibit opposite sense of rotation.

Sense of rotation of mutant axonemes: I tested several motor mutants for their direction of rotation and summarized the results in Table 4.4 . I found that in the case of **ODA1**, which lack outer dynein arms 41% of the observed axonemes exhibit ccw-rotation meaning that the majority showed an opposite direction of rotation. In the case of **IDA5**, which lack IDA a, c, d, e, 77% rotated ccw. In the case of **IDA3**, which lack IDA f, 100% rotated ccw.

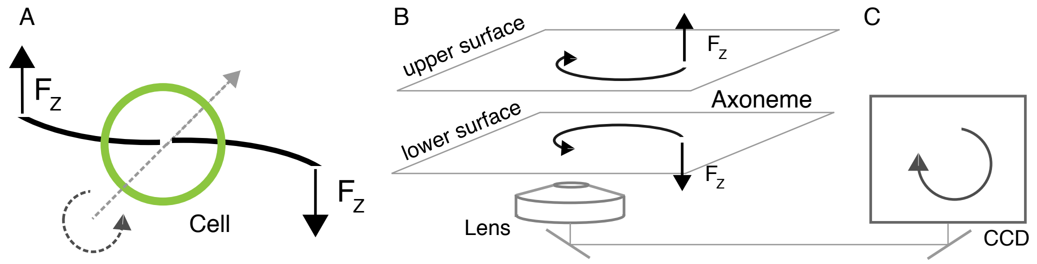

Figure 4.18: Schematic of cell rotation and axoneme rotation. **A** The intact *Chlamydomonas* cell performs a counter clockwise (ccw) rotation around its long body axis during its forward swimming motion. The arrows indicate the forces of the flagellum excreted on the fluid which are normal to the beating plane. These forces causes rotation of the cell. **B** When reactivated in a chamber, the isolated axonemes swim to the chamber surfaces. Filaments close to the upper surface circle CCW when, whereas those close to the lower surface circle CW when viewed below. **C** The optics of an inverted microscope change the sense of rotation. A ccw rotation in the sample appears to be cw when observed through the optics and the camera. Here axonemes swimming close to the lower surface are depicted.

Table 4.4: Direction of rotation of reactivated axonemes.

Strain	**ccw - Rotation** (%)	**N**
WT	100	130*
ODA1	41	72
IDA3	100	15
IDA5	77	51

Direction of rotation of reactivated axonemes of different strains was observed at standard reactivation conditions. Axonemes were observed on the lower surface of the flow chamber using an inverted microscope. Here the direction of rotation is defined as observed by a top view onto the surface. * Data from axonemes reactivated with 0.5-1 mM ATP were pooled.

Discussion: I find that the direction of rotation of reactivated wt axonemes on the surface can be predicted from the known rotation of the cell. This prediction is based on the assumption that a 3-dimensional beat component introduces a mean curvature in the axoneme in z direction. A rough approximation of the magnitude of this z component by the depth of field of the light microscope shows that this assumption is reasonable. This suggests that isolated axonemes swim on a helical swimming path. The fact that beating axonemes on opposite sides of the chamber have opposite direction of rotation confirms that the left and right axoneme are identical and share the same direction of rotation. In the case of opposite direction of rotation of the left and right flagellum or a pure planar beat, which has no chirality, one would expect an equal distribution of ccw and cw rotating axonemes.

The result of a defined chirality in the beat seems plausible considering the chirality of the axoneme that is defined by (1) the polarity of the axoneme, which sets the sliding direction caused by dynein motors and (2) the static binding of dynein motors to the B-tubule, which sets the radial polarity. Since these properties are structural features of the axoneme one might expect the chirality of the swimming path to be a common feature for all mutants. However, it has been shown theoretically how the direction of rotation of cilia is selected dynamically suggesting that a change in the motor response, which could be internal shear resistance or the on or off rates of the motors could in principle give rise to a reversal of the direction of rotation even though the structural chirality stays unchanged [Hilfinger and Jülicher, 2008]. When considering the direction of rotation of mutant axonemes or axonemes reactivated with low ATP, such a situation could be encountered.

At ATP concentrations below 400 μM, axonemes changes its direction of rotation. This result can be understood when assuming that a specific type of motors is mainly contributing to the 3-dimensionality of the beat. As discussed in Section 1.3.2, different affinities for ATP could cause a selective down-regulation of specific groups of motors at lower ATP concentrations. Outer dynein arms are the motors with the highest $\mathrm{K_m}$ value and thus the lowest affinity for ATP, see Table 1.2. To test their contribution to the direction of rotation, I analyzed ODA1 axonemes. I find that only 41% rotate ccw, which suggests that ODA's are greatly involved in defining the sense of rotation. A less pronounced effect has the absence of IDA a, c, d, e in the IDA5 mutant while the absence of the 2 headed IDA f shows no effect.

An explanation for this result could be that OAD and IAD a, c, d, e induce a curvature with positive sign. IDA f could counteract that bending by inducing a curvature with negative sign. If the direction of wave propagation is the same in both cases, the sign defines the direction of rotation. It could also be possible that IDA f is not involved in bending the axoneme in z direction. In that case, another set of motors would have to fulfill that function. Another possibility is that in case of ODA1 and IDA5 the z component of the waveform is much weaker thus the beat is much more planar. This would lead to a equal distribution of cw and ccw rotating axonemes on each of the surfaces. A reasonable explanation could also be that the direction of wave propagation is reversed for isolated axonemes of some of the mutants which is subject to ongoing work.

Since surface accumulation is a complicated hydrodynamic phenomenon thus it is well possible that additional factors, which are not discussed and considered in that section, are important to understand the described phenomenon. Therefore, it is interesting to verify these thoughts with theoretical descriptions.

These findings have implications for the swimming behavior of mutant cells. One prediction from the gained results is that ODA1 and IDA5 cells exhibit a rotational behavior different from WT. The prediction would be that cells either rotate with a decreased rotational frequency by showing cw and ccw rotation or exhibit a strongly attenuated rotation in the case of WT.

4.3.4 Summary:

In this section I investigated how shape parameters govern the swimming behavior. I showed that in the case of the isolated *Chlamydomonas* axoneme the curvature of the mean shape dictates the curvature of the swimming path with a ratio of $k/C \sim 1$. Previous studies on sperm cells found $k/C \sim 2$ and theoretically predicted a decreasing ration for the absence of the sperm head [Friedrich et al., 2010] . I tested simplified hydrodynamic relations for small amplitude waves and confirm that the swimming velocity depends linearly on wavelength and beat frequency and quadratic on the amplitude of the beat. I use these relations to determine the ratio of normal to tangential friction coefficients, which I find to be $\frac{\xi_n}{\xi_t} \sim 2$. The found value agrees to the theoretically predicted limit for an infinitely thin cylinder swimming close to a surface [Hunt et al., 1994]. Using the determined ratio of friction coefficients, a hydrodynamic model and the averaged shape parameters I successfully reconstruct the swimming path of the axoneme.

These results explain why the axoneme swims on a circular path but assume a planar beat. If the beat would be completely planar axonemes would not have a preferred direction of swimming and equal amounts of axonemes would swim clockwise and counterclockwise on a flow chamber surface. I show that this is not the case for WT axonemes where all axonemes swim in clockwise direction. I discuss that a 3 dimensional component gives rise to a directional bios and show that an assumed 3 dimensional component applied to a cell-bound flagellum would give rise to the observed rotation of the cell. By investigating the direction of rotation of different motor-mutant axonemes I ask if specific motors are mainly involved in the production of the 3-dimensional component of the beat. I find that this is the case. The strongest effect has an OAD mutation, where 60% of the axonemes showed a counter-clockwise direction of rotation that is opposite to WT.

4.4 The molecular origin of the circular mean shape.

In this section, I analyze and compare waveforms of reactivated axonemes with different structural or motor mutations. Since there are more than 16 different dynein sub-species in the axoneme, the idea that each dynein has a specific function in shaping the beat is reasonable. This seems plausible when considering the asymmetric distributions of dyneins in the axoneme and when looking at the different biophysical properties of dyneins in *in vitro* assays. Here I present the waveform differences of mutants and reactivation conditions.

4.4.1 Motor Mutations do not abolish the mean shape, a structural mutation does

Axonemes were isolated from cells with different mutations and reactivated in standard reactivation conditions. Image and waveform analysis were performed as described in the previous sections. Since the *Chlamydomonas* waveform is well described by the averaged- shape parameters calculated from the arc-length dependent 0th and 1st Fourier modes (see, Section 4.2.2), I will concentrate on these parameters for waveform comparison of the mutant shapes. A summary on the specific mutation is given in Table 1.3. The length dependent shape parameters are presented in Figure 4.19 , a summary of the averaged shape parameters is given in Table 4.5 .

Motor mutations: I find that motor mutations reduce the amplitude of the beat. The effect on the beat frequency is more diverse. While a mutation in the outer dynein arms (ODA1) reduces the beat frequency strongest, a mutation in a single or a group of inner dynein arms can either increase (IDA3) or reduce (IDA5) the beat frequency. For all mutants, the wavelength is on the order of the length, which leads to a normalized wavelength of 1. I find that for all mutants the mean curvature is decreased. I find a significant difference between each mutant and WT when comparing the mean shear angles at the end. The strongest effect on the mean curvature shows the IDA3 mutant in which the ida f is missing. Comparing ODA and IDA mutants the mean curvature is more strongly influenced by the absence of IAD's.

Structural mutations: A mutation in the MBO gene produces a defined structural defect in the axoneme: the beak-like projection inside the microtubule doublets 1, 5, 6 are missing, see Section 1.3.3. The waveform of these cells looks planar and symmetric. The evaluation of isolated axonemes of these cells show that the mean curvature is about 10 times lower compared to wt axonemes, the beat frequency is reduced by a factor of 2. The amplitude and wavenumber are slightly increased.

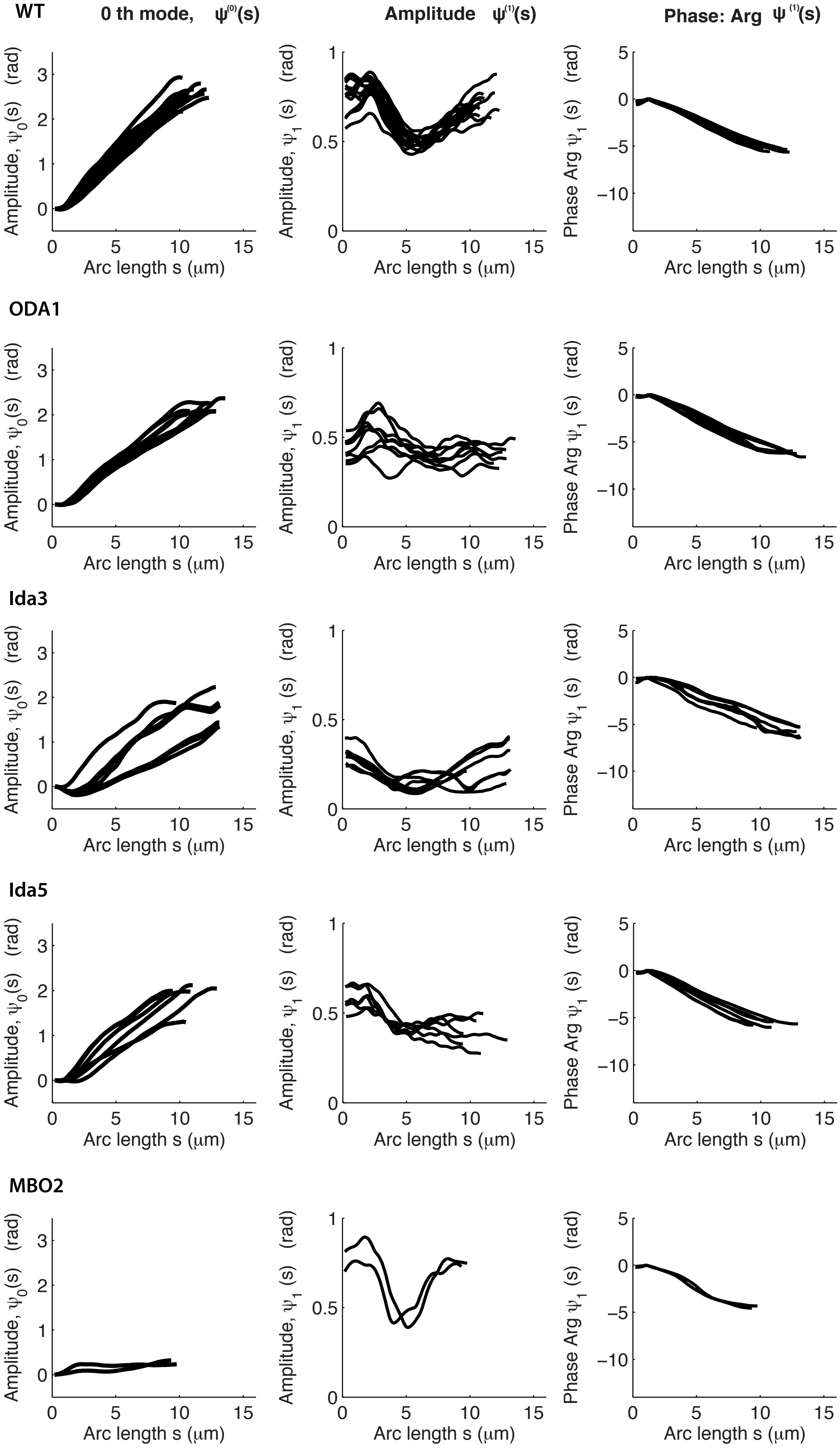

Figure 4.19: Shape Analysis reactivated wt and mutant axonemes.

Table 4.5: Shape Parameters of reactivated axonemes.

	Length L μm	Frequency f Hz	Rot freq f_{rot} Hz	0th Mode Curvature C rad/μm	Mean shear angle $\langle\Psi_S(L)\rangle$ (rad)	Amplitude A rad	Wavelength λ μm	Normal.λ (λ/L)	N
WT	11.1±0.7	65.0± 8.0	8.0±1.6	0.26±0.02	2.6±0.2	0.64±0.05	-11±1	1.00±0.04	13
ODA1	12.0±1.0	24.6± 5.4	1.1±0.2	0.22±0.02	2.2±0.1	0.43±0.05	-10±1	0.83±0.10	8
IDA3	12.6±1.3	87.0±11.0	0.6±0.2	0.17±0.05	1.7±0.3	0.19±0.03	-12±2	0.95±0.10	7
IDA5	10.7±1.3	39.0± 4.0	1.7±0.7	0.22±0.02	1.9±0.3	0.43±0.05	-10±1	0.94±0.10	6
MBO2	9.6±0.3	32.3± 6.6	0.39±0.38	0.02±0.01	0.28±0.06	0.72±0.04	-11±0.02	1.15±0.03	2

Shape parameters are averages of the data presented in Figure 4.12 which are wt axonemes reactivated in standard reactivation conditions and wt cells observed in shallow observation chambers. The individual values for the 0th mode and the phase were determined by least square fitting of the data. Values are (mean±SD,N).

Discussion: The absence of different single or sets of motors affects the waveform. A longstanding statement about the difference of IDA and ODA mutants in the field is that: IDA's are responsible for the shape of the waveform, ODA's contributing to the power [Brokaw and Kamiya, 1987].
The waveform parameters show that mutations in the IAD's consistently affect the mean curvature and beat amplitude, which mainly shape the waveform. The effect of the ODA's is less clear. They seem to contribute to the waveform in a less specific manner. Their effect on the beat frequency can also be achieved by other mutations like IDA5 or MBO. A specific contribution seems to come from IDA f because beat frequency is increased only in its absence the. IDA f is the only double headed IAD. It has been shown to have a low processivity with a duty ratio of 0.6-0.7 [Kotani et al., 2007]. Interestingly, it is also the axonemal dynein with the slowest velocity of microtubule propulsion in a gliding assay. Given these properties it is conceivable, that IDA f acts like a sliding break as it is slow and could act like an additional cross-linker due to its processivity. These properties could be responsible for a high beat-frequency and low amplitude in absence of IDA f. Faster sliding could lead to faster detachment without additional cross-linkers and a lower amplitude and an increased switching rate would be the consequence.

Another parameter is the mean curvature of the shape. One could image different sources for a static curvature: (1) a specific motor with an asymmetric distribution or activation could be responsible for bending the axoneme. (2) a structural asymmetry could rise to a pre-bend axoneme. For the investigated dynein mutants I find that the mean curvature is not abolished in all of the considered cases. If there is a specific dynein, which is solely responsible for the mean curvature it must be among the non considered species which are: IAD b, IAD g or the lately identified low-abundance dyneins DHC 3/4/ and 11. From that selection, currently only the IAD b mutant exists which is IDA 10 which has paralyzed flagella. Further investigations of that mutant have not been carried out yet.

Among the structural mutants the MBO 1-3 mutation results in a symmetric beat. This mutant lacks the intra-doublet projections. For the MBO2 mutant, the mean curvature is almost completely abolished. One explanation could be that the beaks in the wt axoneme are responsible for a pre-bend of the structure in absence of motor activity. This idea can be tested by measuring the curvature of axonemes in absence of motor activity, which I will discuss in Section 4.4.2.

4.4.2 The axoneme is straight in absence of ATP but bend at low ATP concentrations.

The question of the origin of the mean-shape is addressed by analyzing the shape of WT axonemes reactivated at different ATP concentrations. The first question I want to answer is if the axoneme is pre-bent in absence of motor activity, which would suggest a structural determination of the mean shape. On the other hand, the mean shape could be an output of the dynamic system and determined as a balance of motor, bending and hydrodynamic forces. Since a reduction of ATP has been shown to affect the beat frequency [Brokaw, 1975a] I can study the dependence of the mean shape as a function of beat frequency using different ATP concentrations. As I have discussed in Section 1.3.2, different motors have different affinities to ATP. If specific motors determine the mean-shape, can we identify them by analyzing the mean shape at different ATP concentrations as their relative contribution to the shape will relate to their ATP affinity?

To investigate these questions, I perform a standard reactivation assay with different ATP concentrations in presence of ATP-regenerating system. The results of this experiment are summarized in Figure 4.22 and Table 4.6.

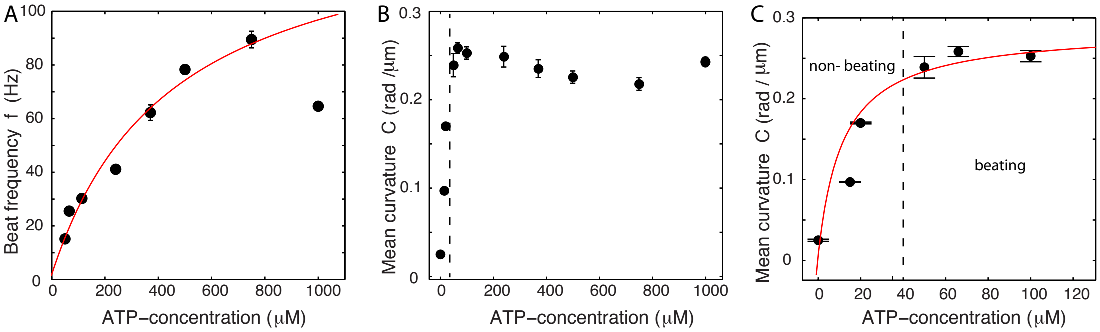

Figure 4.20: Beat frequency and mean curvature dependence on ATP The dependence of the beat frequency and the mean curvature of reactivated wt axonemes on the ATP concentration is considered. **A** Dependence of mean-beat frequency on ATP concentration. Data is presented as mean±SEM values see Table 4.6 . The solid red line depicts a least square fit of a Michaelis-Menten kinetics model: $\mathrm{f} = \mathrm{f}_{\mathrm{max}}([\mathrm{ATP}]/\mathrm{K}_{\mathrm{m}}/1 + [\mathrm{ATP}]/\mathrm{K}_{\mathrm{m}})$ with the maximal frequency of $\mathrm{f}_{\mathrm{max}}$ = 142±13 Hz and the K_{m} of 449±83 μM, R^2=97. For the fit the last point has been discarded. **B** Dependence of mean curvature on ATP concentration. The dashed black line depicts the transition between beating and non beating. **C** Section of panel B shows the transition between beating and non beating (black dashed line). The solid red line depicts a least square fit of a Michaelis-Menten kinetics model: $\mathrm{C} = \mathrm{C}_{\mathrm{max}}([\mathrm{ATP}]/\mathrm{K}_{\mathrm{m}}/1 + [\mathrm{ATP}]/\mathrm{K}_{\mathrm{m}})$ with the maximal curvature of $\mathrm{C}_{\mathrm{max}}$ = 0.27±0.03 rad/μm and the K_{m} = 10.9±0.6 μM, R^2=94. The mean curvature of non-beating axonemes was measured by calculating $C = \psi(L) - \psi(0)/L$. Values are (mean±SEM, N≥113).The fit parameters are presented with its SD.

I find that the beat frequency decreases with ATP concentration as shown in Figure 4.20 A. I determine the critical ATP concentration for reactivation to be 40 μM. Interestingly, at high ATP concentrations, the beat frequency is lower than at intermediate concentrations so that ATP concentrations of 1000 and 400 μM exhibit the same frequencies. When I take the beat frequency as a measure for the combined enzyme kinetics of the dynein motors that contribute to the beat, I can calculate an averaged K_{m} value by fitting a Michaelis-Menten kinetics model to the data as suggested by [Brokaw, 1975a]. I get a K_m value of 449±83 μM. For the fit I discarded the last data point since the model assumes a saturating substrate turn over and thus is not capable of describing the experimental data for high ATP concentrations.

Mean curvature: I find that the mean curvature of beating axonemes is above 0.2 rad/μm irrespective of ATP concentration which results in the typical breast and recovery stroke like beat as reported in Section 4.2.2. For higher ATP concentrations, and higher beat frequencies the mean curvature decreases but this decrease is only less than 10% as shown in Figure 4.20 B. Below an ATP concentration of 40μM the axoneme does not beat. However, the mean curvature stays hight at the transition to the non-beating state and decays with decreasing ATP concentration as shown in Figure 4.20 B and C. In absence of ATP the axoneme is almost straight with a mean curvature of 0.025±0.02 rad/μm. Since the decrease in mean curvature is ATP dependent and thus motor driven, I calculate a K_M value for the set of contributing motors using the beat frequency. I find that the Michaelis Menten model can describe the data well and gain a K_M of 10.9±2.5 μM. The fit of the data is shown in Figure 4.20 C.

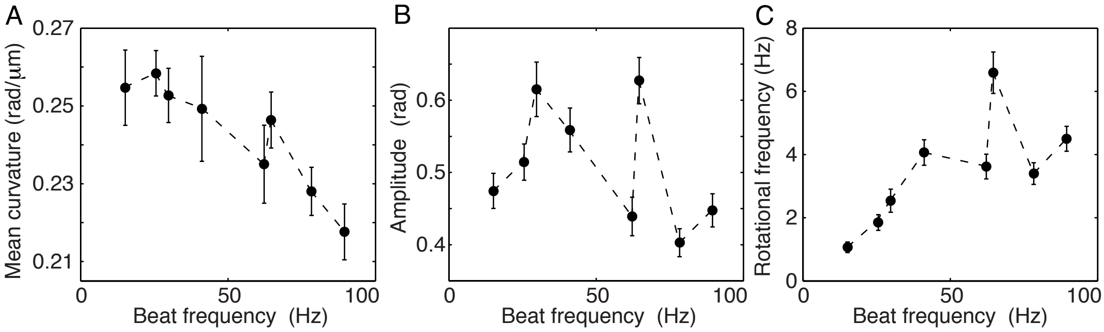

Figure 4.21: Frequency response of shape parameters. The frequency response of the averaged shape parameters for reactivated wt axonemes is presented. The frequency of the axonemes was altered by using different ATP concentrations. The dependence of the beat frequency on ATP concentration is depicted in Figure 4.20. **A** Averaged 1st mode amplitude as a function of beat frequency. The dashed line is plotted to guide the eye **B** Mean curvature as a function of beat frequency **C** Rotational frequency of the axoneme as a function of beat frequency. Values represent mean±SEM, N>9. The valued are presented in Table 4.6.

Beat frequency: The ability to tune the beat frequency by ATP concentration allows me to explore the frequency dependence of the shape parameters, see Figure 4.21. Doing a comparison it is important to keep in mind that the axoneme works at different ATP concentrations. I find that the mean curvature decreases with increasing beat frequency. The amplitude shows the general trend to decrease with bead frequency. Interestingly, the amplitude has a maximal value at 60 Hz and shows a second maxima at 30 Hz. The rotational frequency increases with beat frequency. As mean curvature and amplitude the rotational frequency has a maximum at 60 Hz, which corresponds to an ATP concentration of 400 μM.

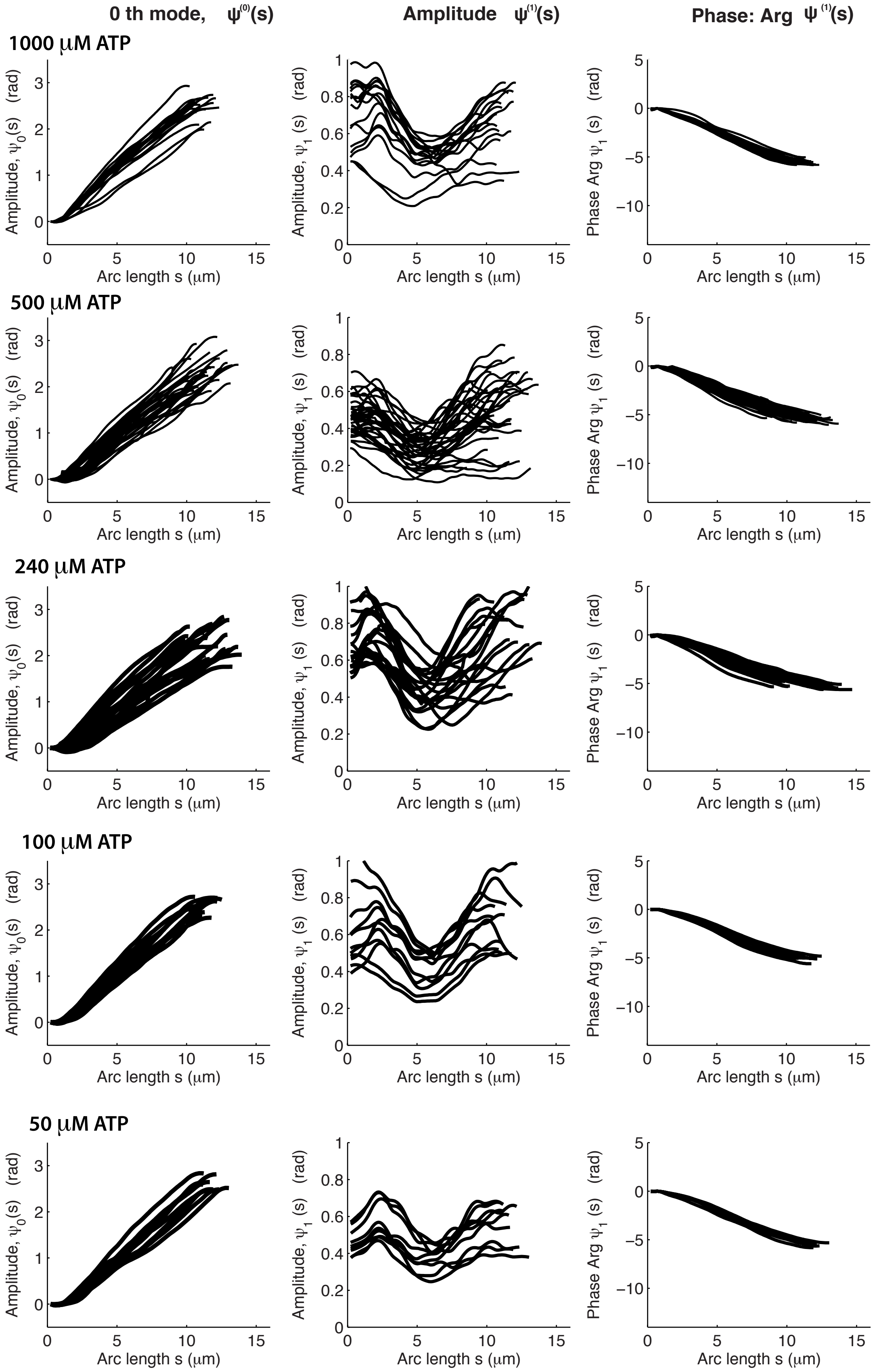

Figure 4.22: Shape Analysis wt axonemes reactivated with different ATP concentrations.

Table 4.6: **Shape Parameters of reactivated axonemes.**

ATP μM	Length L μm	Frequency f Hz	Rot freq f_{rot} Hz	0th Mode Curvature C rad/μm	Mean shear angle $\langle \Psi_S(L) \rangle$ (rad)	Amplitude A rad	Wavelength λ μm	λ Normal. (λ/L)	N
1000	11.2±0.6	64.6± 2.6	6.6±2.9	0.25±0.03	2.5±0.3	0.64±0.05	-11±1	1.00±0.04	18
750 *	12.0±1.0	89.5± 20.0	4.5±2.3	0.22±0.04	2.3±0.3	0.45±0.10	-12±1	0.98±0.04	46
500	11.5±1.2	78.3± 10.1	3.4±2.0	0.23±0.04	2.3±0.4	0.40±0.12	-11±2	0.87±0.44	37
370 *	11.0±1.8	62.2± 16.0	3.6±2.1	0.24±0.06	2.2±0.5	0.44±0.14	-12±2	0.97±0.05	30
240	12.0±1.5	41.1± 8.5	4.1±2.1	0.25±0.07	2.4±0.4	0.56±0.16	-13±2	0.94±0.05	26
100	11.4±0.7	29.8± 4.1	2.5±1.2	0.25±0.02	2.5±0.2	0.62±0.05	-12±2	0.98±0.04	11
66	11.0±0.7	26.0± 4.9	1.9±1.0	0.26±0.02	2.4±0.22	0.52±0.10	-10±2	0.90±0.48	15
50	11.8±0.6	15.1± 2.1	1.1±0.5	0.26±0.03	2.6±0.14	0.48±0.04	-12±0.5	1.0±0.04	9

Ensemble average of shape-parameters extracted from the data presented in Figure 4.22. Wt axonemes were reactivated in standard reactivation conditions. The individual values for the 0th mode and the phase were determined by least square fitting of the data. Values are (mean±SD,N).

* The beat-frequency distributions exhibited an bimodal appearance.

Discussion: Previous studies on demembranated Lytechinus spermatozoa have shown that the beat frequency dependence on ATP concentration follows a Michaels Menten enzyme kinetics model with $\mathrm{K_m} = 0.43$ mM and $\mathrm{f_{max}} = 26$ Hz [Brokaw, 1967, Brokaw and Josslin, 1973]. For reactivated *Chlamydomonas* axonemes I find a similar K_m value of $\mathrm{K_m} = 449\pm83\,\mu$M and a different f_{max}=142±13 Hz, which is 5.5x higher in the case of *Chlamydomonas*. The kinetic model does not capture the frequency decrease for the ATP concentrations above 750 μM where the beat frequency drops again. This decrease could have different sources: For sea urchin sperm flagella it was shown that the products of the de-phosphorylation of ATP, which are ADP and $\mathrm{P_i}$ as well as high concentrations of $\mathrm{ATP^{4-}}$ or $\mathrm{Mg^{2+}}$ inhibit the beat by reducing the beat frequency [Okuno and Brokaw, 1979]. In our case the ATP/ Magnesium/ ADP ratio is held constant by the regenerating system but the phosphate concentration increases over time. In Brokaw's study it was shown that the inhibitory effect of phosphate is most severe in the absence of ADP, which corresponds to the considered case. Since free phosphate will be mainly exist in form of $\mathrm{HPO_4^{2-}}$ at pH 7.5 I tested the effect of 10 mM $\mathrm{K_2HPO_4}$ on the beat frequency and did not find a significant difference. I also tested the effect of 10 mM $\mathrm{KH_2PO_4 \cdot 7H_2O}$ where I could not detect a significant difference either. In the considered case this suggests that there might be a different mechanism setting the frequency at high ATP concentrations, which could be subject to further studies.

Another interesting is the low ATP condition. I find that axonemes are reactivated above ATP concentrations of 40 μM where the slowest beat frequency observed was 13 Hz. see Figure 4.20 A. At lower ATP concentrations the axoneme does not reactivate spontaneously. One explanation for this cut-off concentration could be the existence of specific motors, which are responsible for the initialization of the beat. These motors could have a $\mathrm{K_m}$ values above 40 μM and thus might not be able to produce enough force to bend the axoneme at concentrations below. The minor dyneins have been suggested to have that function but have not been tested in motility assays yet. Other candidates could be IDA c,f and the ODA's considering their $\mathrm{K_m}$ values. Their contribution for the initialization of the beat could be tested by characterizing the ATP-concentration, which is sufficient to reactivate mutants that lack the specific sub-species. Interesting in that respect is that the axoneme exhibits a higher mean curvature at low beating frequencies as shown in Figure 4.21 A. As discussed in Section 4.2.4 this could mean that the axoneme spends a larger percentage of it's cycle time in a state with higher curvature. It could also show that at lower ATP concentrations motors, which are responsible for the asymmetry contribute more strongly to the total activity. This would suggest that these motors have a very low $\mathrm{K_m}$ values that can be measured by studying the mean curvature as a function of ATP concentration for non-beating axonemes. The results of this measurement as presented in Figure 4.21 C.

Origin of the mean curvature: The mean curvature is found to decrease with increasing ATP concentration, see Figure 4.20 A. In absence of ATP I find the WT axoneme to be almost straight with a remaining mean-curvature of 0.025±0.02 rad/μm. The mean curvature of bull sperm in the distal part and the mean curvature of the *Chlamydomonas* mutant MBO2 beating with a symmetrical waveform show similar values [Riedel-Kruse et al., 2007] and Figure 4.5. This could correspond to a general small structural asymmetry inherent to all axonemes and maybe needed to initialize the beat. However, in absence of ATP, dyneins are attached to the filaments and thus their holding forces could balance out an intrinsic curvature in the structure. To exclude this possibility, I repeated this experiment using Vanadate, a dynein inhibitor, which mimics the ADP bound state, in which dyneins are not attached to the filament. With Vanadate I got the same result allowing me to conclude that: the mean curvature in not due to structural elements, but to motor activity as discussed in Section 4.4.1.

For the MBO mutant, which beats with a symmetrical waveform and has no identified motor mutation, this would suggest that either the mean curvature producing dyneins specifically recognize a feature associated with the MIP's (Microtubule Inner Proteins), the beak like projections inside the microtubule or that they are missing a regulatory protein important for motor activity. An IDA associated polypeptide is among the missing components in the MBO mutant [Segal et al., 1984]. Therefor it would be interesting to characterize the MBO mutants more extensively, structurally and biochemically.

To characterize the mean curvature producing motors, I calculate a K_m value from the curvature - ATP dependence presented in Figure 4.21 C. The data is well described by a Michaelis Menten model and I find a $K_m = 10.9 \pm 0.6\,\mu M$. Comparing this value to the known properties of dynein motors summarized in Table 1.2 the only dynein with a comparable value is IDA b, which has K_m value of $10.3 \pm 4.7\ \mu M$ measured in the gliding geometry [Kotani et al., 2007] . Interestingly, this is also the only IDA, which does not rotate microtubules. If rotation of doublets promote twist, it could be possible that the initialization of the beat is related to the twist of the axoneme which can be accomplished by all the other IDA's. The mean-curvature and bending could mainly be supported by dyneins, which are only capable of sliding.

Coming back to IDA b and its possible relation to mean curvature. We know that the characteristic for the axonemal mean shape is its constant curvature. How would a motor need to act on the axoneme to bend it to a circular arc? From beam mechanics we know that an applied moment to the end of a beam bends it into a circular arc. This would suggest that a concentrated force at the end of the axoneme could technically be the origin of the mean shape. Recent studies of the asymmetric distribution of dyneins in the axoneme have been presented for *Chlamydomonas* [Bui et al., 2012]. The results of that study I present in Figure 1.7 , which show that IDA b is the only dynein that is completely missing in the proximal region of the axoneme and along the whole MTD 9. So far the exact distribution in the central region in unknown, but it exists in the distal region. This shows that IDA b has an asymmetric distribution radially and longitudinally. Based on these facts, it is conceivable that the radial asymmetry is important to define the bending direction, the longitudinal asymmetry is important the bend the axoneme into a circular arc and therefor defines the mean shape. Since we know the exact arrangement of the doublets with respect to the cell-body of an intact cell and the distribution of motors in the axoneme, we can think about the contribution of each set of motors to the bend. In Figure 1.8 the cell body with the attached axonemes and the individual doublets are depicted. The axoneme can be thought of as being composed of 2 halves. Motors in one half contribute to the principle, motors in the other half to the reverse bend. Motors that contribute to the mean curvature must be active in the same half as motors that contribute to the principle bend. They must be able to produce higher forces compared to the motors in the second half to introduce an asymmetry into the right direction. Ida b is completely missing on DMT 9 that is located in the half where motor activity contributes to the reverse stroke. Thus, IAD b motors on the half contributing to the principle stroke would win a tug of war situation which then would result in a mean curvature into the right direction (principle stroke direction).

The wavelength dos not depend on ATP concentration, which is the same for sea urchin sperm in the range of the considered ATP concentrations [Brokaw, 1975a].

Frequency response of shape parameters: The ability to reactivate the axoneme at different frequencies allows to study the shape parameters of the beat in a frequency dependent manner. Many oscillating systems hereby exhibit resonance, which means that they respond at greater amplitude when the oscillation frequency matches the system natural frequency. In the case of the axoneme I find that the amplitude is high at 30 Hz and 60 Hz. There sees to be a mechanical optimum for the system at these frequencies. It is interesting that the intact cell selects for a beat frequency close to 60 Hz. As I have shown in Section 4.3.1 the swimming velocity is proportional to the square of the amplitude. Selecting for a high amplitude therefore increases the swimming velocity, which is proportional to the rotational frequency presented in Figure 4.21 C. This suggests that the cell selects for an optimal waveform that promotes fast swimming. Its features are a high amplitude at an intermediate frequency, a high mean curvature considering the observed parameter range and a low ATP requirement. The axonemes beating at 60 Hz were reactivated in only 370 μM ATP. For the cell this could hint towards a comparable ATP concentration in the flagellum. Besides the swimming the nutrient uptake is crucial for the cell. It would be interesting to investigate if these shape parameters create an optimal flow field for nutrient uptake, which was considered for artificial shapes by [Tam and Hosoi, 2011] This optimal waveform gives rise to optimal propulsion conditions. based on these findings it would be interesting to compare the theoretical optimum for propulsion to the *Chlamydomonas* cell waveform. Another question that could be addressed theoretically is how the axoneme selects for its optimal beat frequency?

4.4.3 Viscous load decreases the mean curvature

During the beat, the viscous forces are counteracting the motor forces in the axoneme. Here, I increase the viscous forces acting on a reactivated axoneme using calibrated solutions of Ficoll-400 under standard reactivation conditions. The effect on the beat is presented in Figure 4.23. An increase in viscosity by a factor of 10 decreases the beat frequency by a factor of 4 and the mean-curvature by 25 %. All the other shape parameters are constant including the wavelength.

Discussion: Increasing viscous forces increase the load-force acting on the engaged motors. This can have different effects: The probability of a motor to detach from the filament can increase (force induced detachment) or the motor can be stalled in its action. Both scenarios influence the waveform. A decreasing number of motors can collectively produce less force thus lower sliding forces can be achieved. At constant load this has an effect on the sliding velocity, which relates to the beat frequency. In the case of the intact cell discussed in Section 4.2.4 I argued that increased viscous forces slow down the beat or change the mean curvature by increasing the force on the motors responsible for the mean curvature. Here, under controlled conditions of increased viscosity, I find that beat frequency and mean curvature decrease with increasing load, which supports that reasoning. Interestingly, I find that the remaining shape parameters, amplitude and wavelength are unaffected. For the considered range of viscosities this is supported by measurements on sea urchin sperm [Brokaw, 1975a] . These measurements are valuable since they contain information on the force response of the motor system, which potentially can be used to extract a force velocity curve of the motors. The beat response to increased viscosity can also be used to refine hydrodynamic simulations of the beating axoneme in close to surfaces which will be necessary to understand the differences between the beat of the isolated axoneme and the cell-bound flagellum.

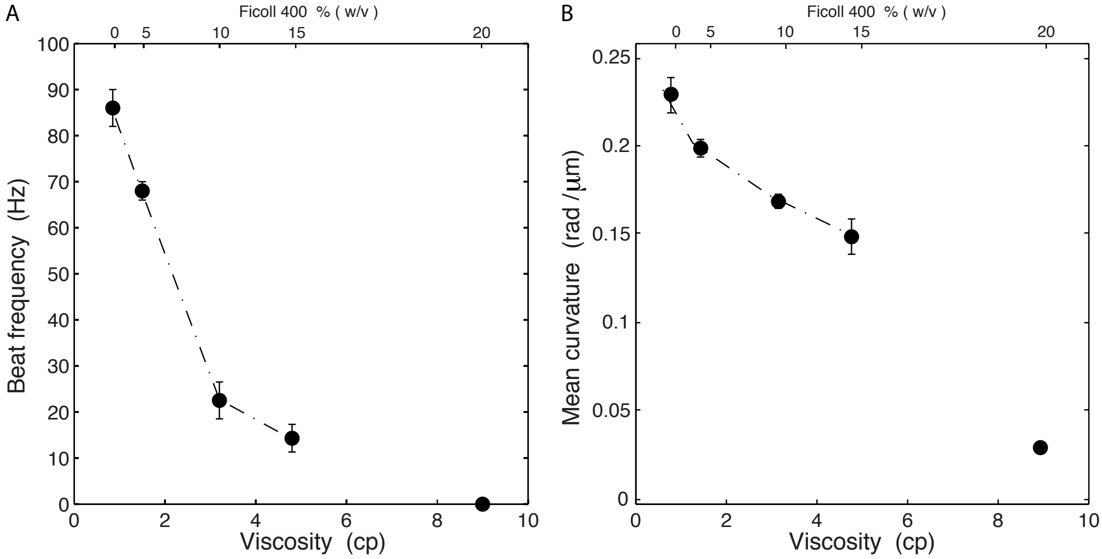

Figure 4.23: Beat frequency and mean curvature dependence on viscosity. The beat frequency and mean curvature of wt axonemes reactivated in standard conditions was measured in the presence of different Ficoll 400 concentrations. The corresponding viscosities have been determined prior to the experiment using a Brookfield viscosimeter. **A** Dependence of beat frequency on Viscosity. Axonemes at 9 cp were not beating. Values are (mean±SEM,N=80) **B** Dependence of mean curvature on viscosity. Values are (mean±SEM, N=10)

4.4.4 Summary:

In this section I investigated the origin of the circular mean shape, which is the key feature of the asymmetric beat. I showed that available motor mutants do not abolish the circular mean shape while a structural mutation does. Thus, I test if the mean shape has a purely structural origin in the sense that the axoneme is pre-curved in absence of motor activity. I find that even in the non-beating regime motor force is needed to curve the axoneme. This suggests that an asymmetric motor activity is the origin of the mean shape. To explore this asymmetry I study the mean shape at ATP conditions-below the critical ATP concentration for beating. In this range the mean curvature is ATP dependent and follows a Michaelis-Menten type behavior with a K_m value of K_m=10μM. A motor that performs work at this ATP concentration must have a low K_m value and thus would selectively be activated. I find that the IAD b has a K_m=10μM. If the activity of this motor gives rise to the mean-curvature it must have an asymmetric distribution in the axoneme. Indeed, IAD b is the only motor that is completely missing on MTD 9 and at the basal end, its abundance in the central part is unknown. Torque generation by IAD b at the distal end of the axoneme provides a reasonable explanation for the bend of the axoneme into a circular arc. In the beating regime I show that the mean curvature decreases with beat frequency. Even more pronounced is this effect when the viscosity of the surrounding medium is increased. Analogously, in the case of the intact cell a change in boundary conditions has a similar effect as the clamping of one end which increases the drag force acting on the axoneme and decrease the mean curvature. In all cases the viscous drag forces acting on the axoneme are increased. These drag forces decrease the mean curvature potentially by counteracting the responsible motors. The exact forces acting on the axoneme can be calculated using resistive force theory and compared in a beat cycle dependent manner. Separating the forces produced during the principle and the reverse bent at different loading conditions will help to characterize the force asymmetry responsible for the mean shape. These ideas are followed up as ongoing work.

4.5 Curvature-dependent dynein activation accounts for the shape of the beat of the isolated axoneme

In this section I present a comparison between two concepts for motor regulation, which are sliding and curvature control, formulated in a theoretical model. This model was then used to fit the experimental data gained for Chlamydomonas WT axonemes. The theory for this chapter was mainly developed and implemented by Ingmar Riedel and Andreas Hilfinger [Riedel-Kruse et al., 2007]. The refinement and adaptation of the model was done by Pablo Sartori with help of André Scholich, the fits presented were done by Pablo and André.

The application of the sperm equation to Chlamydomonas axoneme waveforms

The waveform of a beating flagellum can be described by a basic model that considers (1) elastic forces that straighten the filament, (2) fluid forces that act on the moving filament and (3) the internal shear forces, which are actively bending the structure. These forces are balanced in the beating axoneme. A theoretical description, which considers these forces was presented by Machin who used it to show that the axoneme must be an actively bending structure rather than a whip driven by an oscillator at its base [Machin, 1958]. Later, this concept was refined with models for the force generating molecular motors [Brokaw, 1972b, Camalet et al., 1999, Lindemann, 1994a]. In a study by Riedel-Kruse this concept was presented in a dynamic equation termed the sperm equation and applied to bull sperm waveforms [Riedel-Kruse et al., 2007]. Fitting the sperm equation to experimental data the authors found good agreement with a sliding-controlled motor regulation mechanism. In this study, we fit *Chlamydomonas* waveforms using the sperm equation:

Sperm equation in time domain: The sperm equation describes the shape dynamics by: (1) a hydrodynamic term with $\xi_\perp$ being the hydrodynamic drag for motion perpendicular to the axoneme with units of $[pN \cdot s/\mu m^2]$, (2) an elastic term with κ being the bending rigidity of the axoneme in units of $[pN \cdot \mu m^2]$, and (3) the shear-force density f in units of $[pN/\mu m]$, which includes active (the dynein motors) as well as passive elements (inter doublet links and protein friction). The diameter of the axoneme is a. The sperm equation in time domain is given by:

$$\xi_\perp \partial_t \psi(s,t) = -\kappa \partial_s^4 \psi(s,t) + a \partial_s^2 f(s,t) \tag{4.12}$$

The shear-force density f is described by a motor model, which assumes a linear force response to a small sliding displacement Δ trough a response coefficient $\chi(t-t')$. Analogous we define $\beta(t-t')$, which characterizes the force response to a change in curvature C. The force generated at any point and time depends on the past of the shearing and the curvature. In the linear regime, assuming a homogeneous response over the arc-length and using time invariance, we get:

$$f(s,t) = \int_0^t [\chi(t-t')\Delta(s,t') + \beta(t-t')C(s,t')]dt' \tag{4.13}$$

By balancing the internal shear forces we gain the following equation of motion for sliding at the base of the axoneme:

$$\gamma_s \frac{d}{dt}\Delta_0(t) = -k_s\Delta_0 - \int_0^L f(s,t)ds \tag{4.14}$$

with the basal friction coefficient γ_s, the basal stiffness k_s and the integral term, which describes the total force produced in the axoneme that sums up at the base.

Sperm equation in frequency space: Now we write the dynamic equation in frequency space. We only focus on the first mode as I have shown that the waveform is well characterized by the fundamental mode. **Note:** Form here on I will use $\widetilde{\psi} = \widetilde{\psi}^{(1)}$, $\widetilde{f} = \widetilde{f}^{(1)}$, $\widetilde{\Delta} = \widetilde{\Delta}^{(1)}$, $\widetilde{C} = \widetilde{C}^{(1)}$. Then the sperm equation in frequency space is given by:

$$i\omega\xi_\perp\widetilde{\psi} + \kappa\widetilde{\psi}'''' - a\widetilde{\beta}\widetilde{\psi}''' - a^2\widetilde{\chi}\widetilde{\psi}'' = 0 \tag{4.15}$$

The force density takes the form:

$$\widetilde{f}(s) = \widetilde{\chi}\widetilde{\Delta}(s) + \widetilde{\beta}\widetilde{C}(s) \tag{4.16}$$

The equation of motion for sliding at the base of the axoneme is given by:

$$\gamma_s i\omega\widetilde{\Delta}_0 = -k_s\widetilde{\Delta}_0 - \int_0^L \widetilde{f}(s)ds \tag{4.17}$$

Boundary conditions: To solve the sperm equation we have to consider boundary conditions that specify the balance of torques and forces at the ends of the axoneme. In the presented case we use the following two torque (1,2) and two force (3,4) boundary conditions, which define that there are no external forces or torques at either end:

(1) $\kappa\widetilde{\psi}'(0) = ak_s\widetilde{\Delta}_0 + a\gamma_s\ i\omega\widetilde{\Delta}s$, which considers sliding at the base
(2) $\widetilde{\psi}'(L) = 0$
(3) $\kappa\widetilde{\psi}''(0) = a\widetilde{f}(0)$
(4) $\kappa\widetilde{\psi}''(L) = a\widetilde{f}(L)$

The torque at the base is balanced by a basal spring. Experimentally we find that BC 2 is satisfied corresponding to zero curvature at the distal end of the axoneme as illustrated in Figure 1.11 for the wt axoneme. This is expected since there is no external torque acting on the distal end.

Defining Sliding and Curvature control: The general question that we want to address is if motors actively respond to sliding displacement or if they are activated by curvature. Our response coefficients are complex numbers: A positive value hereby describes a passive, a negative value describes an active response, an imaginary entry shows the existence of a time delayed response. Thus, we define what sliding and curvature control means in the frame work of our model:

Sliding control $\widetilde{\chi}_b > 0, \widetilde{\chi} < 0,\quad \widetilde{\beta} = 0$
Curvature control $\widetilde{\chi}_b > 0, \widetilde{\chi} > 0,\quad \widetilde{\beta} = +-i$

Fitting the sperm equation to experimental data: We now use the theoretical framework to fit experimental data. We use the following approximate values $\kappa = 400\,\text{pN}/\mu\text{m}^2$, a $= 0.185$ μm and $\xi_\perp = 0.0034\,\text{pN}\mu\text{m}^{-2}$ to fit the model. Similar values have been used to fit the bull-sperm waveforms using the sperm equation [Riedel-Kruse et al., 2007]. Compared to sperm, the *Chlamydomonas* axoneme is lacking additional stabilizing fibers and its bending rigidity κ has been reported to be lower, see Table 1.1 . We determine the motor-response coefficients by fitting the sperm-equation Equation 4.15 to waveforms gained from reactivated *Chlamydomonas* axonemes using the boundary conditions described above. We only consider the 1st Fourier mode of the oscillation. To discriminate between the two motor regulation mechanisms, we fit two different equations: (1) sperm equation with response coefficients for sliding and curvature and (2) the sperm equation with response coefficients for sliding only. To be able to compare the gained goodness of the fits, we used the same number of fit parameters in both cases. This was possible since in preliminary fits we found k_s and γ_s to have very small values in the case of the curvature control model. Setting these values to zero is similar to using boundary condition (2) for the basal end. This is a reasonable assumption as we also observe no curvature at the basal end in the experimental data. By setting these two parameters to zero, we gain equally good fits.

Fitting Results A typical fitting result for either model is presented in Figure 4.24. The averaged response coefficients of 7 axonemes are listed in Table 4.7. The R^2 values, which characterize the goodness of the fit show that the curvature control ($R^2 = 0.95$) model describes the data better than a pure sliding control model ($R^2 = 0.87$). The fits in Figure 4.24 show that especially the movement of the ends of the axoneme is much better captured by the curvature control mechanism.

Sliding control: The summarized fit parameters in Table 4.7 show χ to have a negative real part, which represents an active response to sliding that is 2 times stronger than the delayed passive response represented in the positive imaginary part of χ. The basal stiffness k_s and the basal friction coefficient γ_s show negative values, which describes an active response to sliding. The sliding displacement at the basal end is 200 nm.

Curvature control: The fit parameter χ shows a passive response to sliding, which is 800 times stronger than the delayed passive response. The delayed active response to curvature represented by the imaginary part of β is 60 times stronger than the passive curvature response. The sliding displacement at the basal end is 100 nm. Here, the base has no additional stiffness or friction.

Discussion: We use the linear sperm equation to fit experimental data. Strictly speaking, the sperm equation is only valid for small beat amplitudes, but provides a good starting point for a theoretical analysis. Fitting the experimental data with two different models, sliding and curvature control, we find that the curvature control model captures the experimental data best. We performed fits for multiple axonemes and find similar fit parameters in all cases, which allows us to calculate the averaged values for standard reactivation conditions as presented in Table 4.7. For the sliding control model, we gain negative stiffness and friction for the base. This means that this model suggests an active sliding response of the base. One could imagine that a specific set of Dyneins assists sliding in the basal region, which could than lead to a fast build up of a bend and to the initialization of the beat. The curvature control model on the other hand assumes that

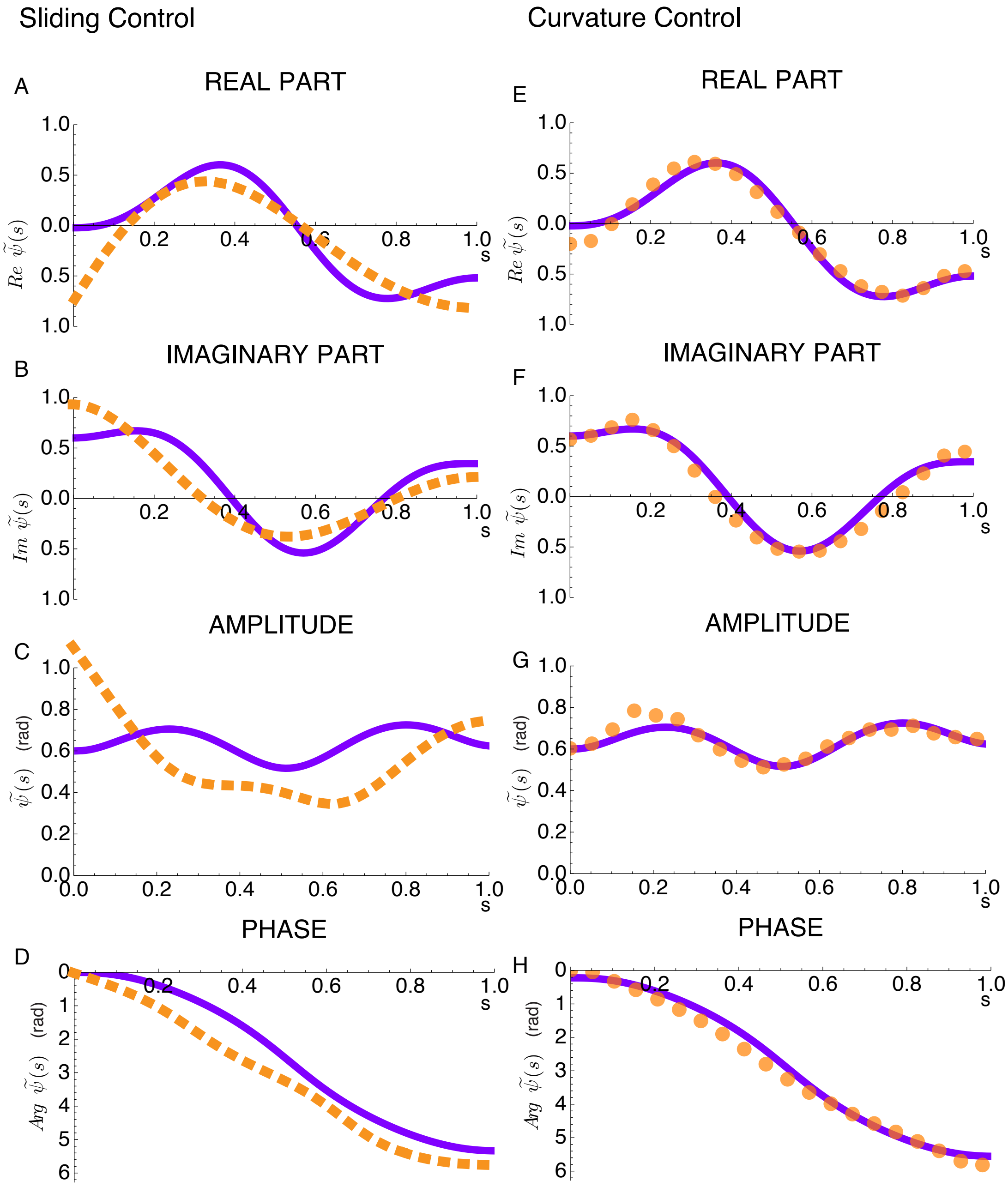

Figure 4.24: Fits of the sperm equation to Chlamydomonas waveforms. The sperm equation Equation 4.15 was fitted to the real and imaginary part of ψ of a typical *Chlamydomonas* WT waveform of an isolated axoneme with $\mathrm{l} = 12.2\mu\mathrm{m}, \mathrm{f} = 51.7\,\mathrm{Hz}$. The figure shows a representative fit of a sliding-control model (A-D) and a curvature control model (E-F). Both models comprise the same number of 2 free fit parameters. The solid purple lines represent the data, the dashed and dotted lines are the fits. The parameters gained from the fitting procedure are: **Sliding-control model** (A,B) $\chi = -2177 + 1117i\ \mathrm{pN}/\mu\mathrm{m}^2, \Delta_0 = 190\,\mathrm{nm}, \mathrm{k_s} = -30\,\mathrm{pN}/\mu\mathrm{m}, \gamma_\mathrm{s} = -18\,\mathrm{pN/s}/\mu\mathrm{m}, \mathrm{R}^2 = 0.84$ **Curvature-control model** (D,F) $\chi = 3728 + 6i\ \mathrm{pN}/\mu\mathrm{m}^2, \beta = 28 - 2683\mathrm{i}\ \mathrm{pN}/\mu\mathrm{m}^2, \Delta_0 = 119\,\mathrm{nm}, \mathrm{k_s} = 0\,\mathrm{pN}/\mu\mathrm{m}, \gamma_\mathrm{s} = 0\,\mathrm{pN/s}/\mu\mathrm{m}, \mathrm{R}^2 = 0.96$, Averaged values for the sliding and curvature response parameters (N=7) are given in Table 4.7.

Table 4.7: Averaged fit parameters for sliding and curvature control model.

Model		**Sliding Control**	**Curvature Control**
χ	pN/μm^2	$-2100 + 1100i \pm (330 + 290i)$	$+3317 + 4.3i \pm (837 + 1.7i)$
β	pN	0	$+42 - 2581i \pm (18 + 316i)$
Δ_0	nm	199±38	111 ± 21
k_s	pN/μm	-27±7	0
γ_s	pN/s/μm	-1±0.6	0
R^2		0.87 ± 0.02	0.95 ± 0.014

Averaged fit parameters for the sperm equation for the case of sliding and curvature control. In both cases 2 fit parameters $\chi Re/Im$ were used. Values are represented as (mean±SD, N=7). Axonemes were reactivated in standard reactivation conditions.

the base has the same mechanical properties as the rest of the axoneme meaning that it does not consider additional springs or dash-pots at the base. Although this is assumed the sliding displacement at the base has a 2 times smaller value compared to the sliding control model. This could imply that during the beat the forces acting on the base are small. From the EM images presented in Section 4.1.1 we learned that even in the bend configuration there is no sliding at the basal end. This would argue for an increased stiffness at the basal end. A combination of both ideas could be that for bending the axoneme into a static bend a basal restriction is needed. However, in the dynamic case this restriction might be unnecessary. These ideas are explored theoretically and are subject to ongoing work in collaboration with Pablo Sartori. The result that motors respond to curvature still does not suggest a mechanism by which the motors are able to sense it. One idea in the literature is related the production of normal forces, which would separate the doublets in the bending axoneme. The local regulation of motors by such a geometric detachment is a mechanism that could be used to explain the gained result and thus should be explored in a next step [Lindemann, 1994a] .

Chapter 5

Conclusions and Outlook

In this thesis I used the experimental model 'the isolated axoneme' to characterize the beat of the single cell green alga *Chlamydomonas reinhardtii.* The reactivated axoneme system allows the characterization of the beat under controlled, cell free conditions. Other than most flagella, the *Chlamydomonas* axoneme contains no additional stabilizing structures with unknown mechanical properties, which facilitates the theoretical description of the waveform. However, to my knowledge, an exact waveform description of the isolated axoneme was not presented so far.

5.1 Summary of the results

I characterized the isolated axoneme system by showing that: The isolated and demembranated axoneme lacks the basal body and the membrane while the axonemal structure is still intact. Bend axonemes exhibit a blunt base, which shows that sliding at the base is efficiently restricted in the axoneme. The diameter at the distal end of the axoneme is smaller than at the basal end. Dark-field intensity decreases from base to tip and therefore can be used to identify the axonemal polarity. In a isolated and reactivated axoneme the traveling bending-wave propagates from base to tip.

I parameterized the shape using Fourier decomposition and presented a continuous waveform description with 4 parameters: frequency, amplitude, mean-curvature and wavelength. I found that the mean curvature is described by a circular arc. This property shapes the asymmetric beat and provides the difference between the sinusoidal sperm-like-beat and the asymmetric *Chlamydomonas*-beat. This shows that the *Chlamydomonas*-beat can be understood as a sinusoidal beat around a circular arc. Using the shape parameterization I compared the beat of the isolated axoneme to the cell-bound flagellum. I found that the beat shows the same properties. The boundary impact the hydrodynamic loading on the on the flagellum, which alters amplitude and wavelength.

I investigated how shape parameters govern the swimming behavior: I showed that the curvature of the mean shape dictates the curvature of the swimming path. I tested simplified hydrodynamic relations for small amplitude waves and confirmed that the swimming velocity depends linearly on wavelength and beat frequency and quadratic on the amplitude of the beat. I used these relations to determine the ratio of normal to tangential friction coefficients, which I found to be $\frac{\xi_n}{\xi_t} \sim 2$. I successfully reconstructed the swimming path of the axoneme using the determined ratio of friction coefficients, a hydrodynamic model and the averaged shape parameters. I investigated the direction of rotation of axonemes on the surfaces of a reactivation chamber and identified motors, that change the direction of rotation. I presented arguments for the idea that these motors are responsible for the 3D beat of the axoneme and the rotation of the cell. A 3D beat cases a 3D swimming path of the isolated axoneme, which sets the direction of rotation. I showed that these ideas match my experimental findings.

I investigated the molecular origin of the circular-mean shape, which is the key feature of the asymmetric beat. I showed that available motor mutants do not abolish the circular mean shape while a structural mutation does. I showed that the axoneme is not pre-curved in absence of motor activity. I identified IAD b, as a potential motor-candidate responsible for the mean shape using the motors ATP affinity. The asymmetric distribution of IAD b makes it a strong candidate for a torque generator at the distal end, which could explain the bending of the axoneme into a circular-arc. I directly showed that the asymmetry of the flagellar beat decreases with increased viscous load.

I tested two concepts for motor regulation, which are sliding and curvature control by fitting experimental data gained for *Chlamydomonas* WT axonemes with the corresponding theoretical descriptions. I found that used the curvature control mechanism describes the data best. I also found that for the curvature control mechanism an additional sliding restriction at the basal end is not required to describe the beat.

5.2 Future directions

The experimental and theoretical framework developed in this thesis can now be used to explore the molecular origin of the waveform in greater detail.

The shape parameterization makes waveform comparison to theoretical descriptions possible. The increasing accessibility of dynein mutants allows to directly study the specific contribution of a dynein species on the beat. On the other hand, specific mutants can be used to directly address questions asked by the theory. The reactivated-axoneme system also allows for the use of specific dynein inhibitors, which would be interesting to explore in detail for the same reason.

The high spatial and temporal resolution of the beat allows for precise shape characterization. It can also be used elucidate structural changes during the beat. One interesting direction is to directly investigate sliding at the axonemal end during the beat. Preliminary studies I performed have shown that this is technically possible and that a periodic sliding difference between tip and base can be observed. Another direction is to measure the diameter of the axoneme during the beat. This information is valuable when thinking about the time evolution of stresses and strains produced by the motors, which can help to gain deeper inside into the way how motors are controlled.

In the *in situ* system, hydrodynamic forces can be controlled. By studying the shape of specific dynein mutants under different loading conditions one can gain inside into the force velocity properties of the concerted action of dynein motors. These results can then be compared to high resolution measurements performed by optical tweezers on a reconstituted *in vitro* system. The comparison of both has the potential to elucidate motor or axoneme specific control mechanisms.

The presented waveform characterization can be applied to WT axoneme reactivated under different conditions. It has been shown that Taxol decreases the bending rigidity of microtubules. In preliminary studies I found that the reactivation of axonemes in presence of Taxol greatly decreases the beating amplitude at the distal end. Therefore it would be interesting to (1) measure the bending rigidity of axonemes in presence of Taxol and (2) to use theoretical modeling to predict the change of waveform, based on the change of bending rigidity. This experiment has great potential to learn about the curvature or sliding controlled motor regulation mechanism.

Finally, the isolated axoneme system could be used to explore human disease related mutations of cilia and their capability to move fluid. To do this, the waveform of isolated mutant axonemes could be studied in mucus with different properties.

Abbreviation

λ_n	wavelength on the nth mode
A_n	amplitude of the nth mode
f_n	frequency of the nth mode
C_n	curvature on the nth mode
v	swimming velocity
Δ	sliding displacement
λ	wavelength
$\widetilde{x}(f)$	Fourier transform
$\widetilde{x}^{(n)}(f)$	Fourier coefficient of the nth mode
f	shear force density
k	curvature of the swimming path
t	time
1D	one-dimensional
2D	two-dimensional
3D	three-dimensional
κ	bending rigidity
Ψ	tangent angle
ψ	bend angle
Ψ_S	shear angle
ξ	drag coefficient
a	diameter of the axoneme
AAA	superfamily of ring-shaped P-loop NTPases
ADP	adenosine diphosphate
ATP	adenosine triphosphate

ccw	counter-clockwise
cw	clockwise
DC	docking complex
ddH_2O	demineralized water
DRC	dynein regulation complex
DTT	dithiothreitol
EDTA	ethylene-di-amine-tetra-acetate
EGTA	ethylene-glycol-tetraacetic-acid
EM	electron microscopy
FIESTA	fluorescence image evaluation software for tracking and analysis
GDP	guanosine-5'-diphosphate
GTP	guanosine-5'-triphosphate
IAD	inner arm dynein, specific motor
IC	intermediate chain
IDA	inner arm dynein, specific mutant
IFT	intra flagellar transport
K_m	Michaelis-Menten constant
LC	light chain
LED	light-emitting diode
MPI-CBG	Max Planck Institut of Cell Biology and Genetics, Dresden
MTD	microtubule doublet
N	number of measurements
NA	numerical aperture
OAD	outer arm dynein, specific motor
ODA	outer arm dynein, specific mutant
P_i	phosphate
PEG	polyethylene-glycol
PSD	power spectral density
RAM	random-access memory
s	arc length

SD	standard deviation
SEM	standard error of the mean
TEM	transmission electron microscope
TRIS	tris(hydroxymethyl)aminomethane
TTL	transistorâtransistor logic
v	normalized wavelength
V_{max}	maximal rate of substrate turn over

List of Figures

List of Tables

Bibliography

Afzelius, B. A., Dallai, R., Lanzavecchia, S., Bellon, P. L., 1995. Flagellar structure in normal human spermatozoa and in spermatozoa that lack dynein arms. Tissue & Cell 27, 241–247.

Alper, J., Geyer, V. F., Mukundan, V., Howard, J., 2012. Reconstitution of flagellar sliding. Methods in Enzymology 524, 343–369.

Alper, J. D., Tovar, M., Howard, J., 2013. Displacement-weighted velocity analysis of gliding assays reveals that chlamydomonas axonemal dynein preferentially moves conspecific microtubules. Biophysical Journal 104, 1989–1998.

Aoyama, S., Kamiya, R., 2005. Cyclical interactions between two outer doublet microtubules in split flagellar axonemes. Biophysical Journal 89, 3261–3268.

Bessen, M., Fay, R. B., Witman, G. B., 1980. Calcium control of waveform in isolated flagellar axonemes of chlamydomonas. Journal of Cell Biology 86, 446–455.

Bower, R., Tritschler, D., Vanderwaal, K., Perrone, C. A., Mueller, J., Fox, L., Sale, W. S., Porter, M. E., 2013. The N-DRC forms a conserved biochemical complex that maintains outer doublet alignment and limits microtubule sliding in motile axonemes. Molecular Biology of the Cell.

Brokaw, C. J., 1967. Adenosine triphosphate usage by flagella. Science 156, 76–78.

Brokaw, C. J., 1972a. Computer simulation of flagellar movement. I. Demonstration of stable bend propagation and bend initiation by the sliding filament model. Biophysical Journal 12, 564–586.

Brokaw, C. J., 1972b. Flagellar movement: a sliding filament model. Science 178, 455–462.

Brokaw, C. J., 1975a. Effects of viscosity and ATP concentration on the movement of reactivated sea-urchin sperm flagella. Journal of Experimental Biology 62, 701–719.

Brokaw, C. J., 1975b. Molecular mechanism for oscillation in flagella and muscle. Proceedings of the National Academy of Science 72, 3102–3106.

Brokaw, C. J., Josslin, R., 1973. Maintenance of constant wave parameters by sperm flagella at reduced frequencies of beat. Journal of Experiential Biology 59, 617–628.

Brokaw, C. J., Kamiya, R., 1987. Bending patterns of Chlamydomonas flagella: IV. Mutants with defects in inner and outer dynein arms indicate differences in dynein arm function. Cell Motility and the Cytoskeleton 8, 68–75.

Brokaw, C. J., Luck, D. J., Huang, B., 1982. Analysis of the movement of Chlamydomonas flagella:" the function of the radial-spoke system is revealed by comparison of wild-type and mutant flagella. Journal of Cell Biology 92, 722–732.

Brokaw, C. J., Luck, D. J. L., 2005. Bending patterns of Chlamydomonas flagella I. Wild-type bending patterns. Cell Motility 3, 131–150.

Bui, K. H., Yagi, T., Yamamoto, R., Kamiya, R., Ishikawa, T., 2012. Polarity and asymmetry in the arrangement of dynein and related structures in the Chlamydomonas axoneme. Journal of Cell Biology 198, 913–925.

Burgess, S. A., Walker, M. L., Sakakibara, H., Knight, P. J., Oiwa, K., 2003. Dynein structure and power stroke. Nature 421, 715–718.

Camalet, S., Jülicher, F., 2000. Generic aspects of axonemal beating. New Journal of Physics 2, 241–2423.

Camalet, S., Jülicher, F., Prost, J., 1999. Self-organized beating and swimming of internally driven filaments. Physical Review Letters.

Carter, A. P., 2013. Crystal clear insights into how the dynein motor moves. Journal of Cell Science 126, 705–713.

Carter, A. P., Cho, C., Jin, L., Vale, R. D., 2011. Crystal structure of the dynein motor domain. Science 331, 1159–1165.

Carvalho-Santos, Z., Azimzadeh, J., Pereira-Leal, J. B., Bettencourt-Dias, M., 2011. Evolution: Tracing the origins of centrioles, cilia, and flagella. Journal of Cell Biology 194, 165–175.

Coquelle, F. M., Vitre, B., Arnal, I., 2009. Structural basis of EB1 effects on microtubule dynamics. Biochemical Society Transactions 37, 997–1001.

Elgeti, J., Gompper, G., 2013. Emergence of metachronal waves in cilia arrays. Proceedings of the National Academy of Sciences 110, 4470–4475.

Felgner, H., Frank, R., Schliwa, M., 1996. Flexural rigidity of microtubules measured with the use of optical tweezers. Journal of Cell Science 109, 509–516.

Friedrich, B. M., Riedel-Kruse, I. H., Howard, J., Jülicher, F., 2010. High-precision tracking of sperm swimming fine structure provides strong test of resistive force theory. Journal of Experimental Biology 213, 1226–1234.

Gee, M. A., Heuser, J. E., Vallee, R. B., 1997. An extended microtubule-binding structure within the dynein motor domain. Nature 390, 636–639.

Geyer, V., Jülicher, F., Howard, J., Friedrich, B. M., 2013. Cell body rocking is a dominant mechanism for flagellar synchronization in a swimming algae. arXiv:1305.0782.

Gibbons, I. R., 1982. Sliding and bending in sea urchin sperm flagella. Symposia of the Society for Experimental Biology 35, 225–287.

Gorman, D. S., Levine, R. P., 1965. Cytochrome f and plastocyanin: their sequence in the photosynthetic electron transport chain of Chlamydomonas reinhardi. Proceedings of the National Academy of Sciences 54, 1665–1669.

Gray, J., Hancock, G. J., 1955. The propulsion of sea-urchin spermatozoa. Journal of Experimental Biology 32, 802–814.

Heintzmann, R., Ficz, G., 2007. Breaking the resolution limit in light microscopy. Microtubules, in Vitro 81, 561–580.

Heuser, T., Raytchev, M., Krell, J., Porter, M. E., Nicastro, D., 2009. The dynein regulatory complex is the nexin link and a major regulatory node in cilia and flagella. Journal of Cell Biology 187, 921–933.

Hilfinger, A., Jülicher, F., 2008. The chirality of ciliary beats. Physical Biology 5, 016003.

Hoops, H. J., Witman, G. B., 1983. Outer doublet heterogeneity reveals structural polarity related to beat direction in Chlamydomonas flagella. Journal of Cell Biology 97, 902–908.

Howard, J., 2001. Mechanics of Motor Proteins & the Cytoskeleton. Sinauer Associates Incorporated.

Howard, J., Hudspeth, A. J., Vale, R. D., 1989. Movement of microtubules by single kinesin molecules. Nature 342, 154–158.

Hunt, A. J., Gittes, F., Howard, J., 1994. The force exerted by a single kinesin molecule against a viscous load. Biophysical Journal 67, 766–781.

Hutner, S. H., 1950. Anaerobic and aerobic growth of purple bacteria (Athiorhodaceae) in chemically defined media. Journal of General Microbiology 4, 286–293.

Hutner, S. H., Provasoli, L., Schatz, A., Haskins, C. P., 1950. Some approaches to the study of the role of metals in the metabolism of microorganisms. Proceedings of the American Philosophical Society 94, 152–170.

Hyams, J. S., Borisy, G. G., 1975. Flagellar coordination in Chlamydomonas reinhardtii: isolation and reactivation of the flagellar apparatus. Science 189, 891–893.

Jülicher, F., Prost, J., 2009. Generic theory of colloidal transport. European Physical Journal E 29, 27–36.

Kagami, O., Kamiya, R., 1992. Translocation and rotation of microtubules caused by multiple species of Chlamydomonas inner-arm dynein. Journal of Cell Science 103, 653–664.

Kamiya, R., 2000. Analysis of cell vibration for assessing axonemal motility in Chlamydomonas. Methods 22, 383–387.

Kamiya, R., 2009. Assays of cell and axonemal motility in chlamydomonas reinhardtii. Methods in Cell Biology 91, 241–253.

Kamiya, R., Kurimoto, E., Muto, E., 1991. Two types of Chlamydomonas flagellar mutants missing different components of inner-arm dynein. Journal of Cell Biology 112, 441–447.

Kikumoto, M., Kurachi, M., Tosa, V., Tashiro, H., 2006. Flexural rigidity of individual microtubules measured by a buckling force with optical traps. Biophysical Journal 90, 1687–1696.

King, S. M., Sep. 2011. Dyneins. Structure, Biology and Disease. Academic Press.

King, S. M., Otter, T., Witman, G. B., 1986. Purification and characterization of Chlamydomonas flagellar dyneins. Methods in Enzymology 134, 291–306.

Kon, T., Nishiura, M., Ohkura, R., Toyoshima, Y. Y., Sutoh, K., 2004. Distinct functions of nucleotide-binding/hydrolysis sites in the four AAA modules of cytoplasmic dynein. Biochemistry 43, 11266–11274.

Kon, T., Oyama, T., Shimo-Kon, R., Imamula, K., Shima, T., Sutoh, K., Kurisu, G., 2012. The 2.8âA crystal structure of the dynein motor domain. Nature 484, 345–350.

Kotani, N., Sakakibara, H., Burgess, S. A., Kojima, H., Oiwa, K., 2007. Mechanical properties of inner-arm dynein-f (dynein I1) studied with in vitro motility assays. Biophysical Journal 93, 886–894.

Kurachi, M., Hoshi, M., Tashiro, H., 1995. Buckling of a single microtubule by optical trapping forces: Direct measurement of microtubule rigidity. Cell Motility and the Cytoskeleton 30, 221–228.

Leduc, C., Ruhnow, F., Howard, J., Diez, S., 2007. Detection of fractional steps in cargo movement by the collective operation of kinesin-1 motors. Proceedings of the National Academy of Sciences 104, 10847–10852.

Lefebvre, P. A., Nordstrom, S. A., Moulder, J. E., Rosenbaum, J. L., 1978. Flagellar elongation and shortening in Chlamydomonas: Effects of flagellar detachment, regeneration, and resorption on induction of flagellar protein-synthesis. Journal of Cell Biology 78, 8–27.

Linck, R. W., May 2001. Cilia and Flagella. John Wiley & Sons, Ltd, Chichester, UK.

Lindemann, C. B., 1994a. A “geometric clutch” hypothesis to explain oscillations of the axoneme of cilia and flagella. Journal of Theoretical Biology 168, 175–189.

Lindemann, C. B., 1994b. A model of flagellar and ciliary functioning which uses the forces transverse to the axoneme as the regulator of dynein activation. Cell Motility and the Cytoskeleton 29, 141–154.

Lindemann, C. B., Macauley, L. J., Lesich, K. A., 2005. The counterbend phenomenon in dynein-disabled rat sperm flagella and what it reveals about the interdoublet elasticity. Biophysical Journal 89, 1165–1174.

Lodish, H. F., Aug. 2012. Molecular Cell Biology. International Edition. W.H. Freeman.

Lohret, T. A., McNally, F. J., Quarmby, L. M., 1998. A role for katanin-mediated axonemal severing during Chlamydomonas deflagellation. Molecular Biology of the Cell 9, 1195–1207.

Machin, K. E., 1958. Wave propagation along flagella. Journal of Experimental Biology 35, 796–806.

Mickey, B., Howard, J., 1995. Rigidity of microtubules is increased by stabilizing agents. Journal of Cell Biology 130, 909–917.

Mocz, G., Gibbons, I. R., 1996. Phase partition analysis of nucleotide binding to axonemal dynein. Biochemistry 35, 9204–9211.

Namba, K., Yamashita, I., Vonderviszt, F., 1989. Structure of the core and central channel of bacterial flagella. Nature 342, 648–654.

Nicastro, D., Schwartz, C., Pierson, J., Gaudette, R., Porter, M. E., McIntosh, J. R., 2006. The molecular architecture of axonemes revealed by cryoelectron tomography. Science 313, 944–948.

Nogales, E., Wolf, S. G., Downing, K. H., 1998. Structure of the alpha beta tubulin dimer by electron crystallography. Nature 391, 199–203.

Norrander, J. M., Perrone, C. A., Amos, L. A., Linck, R. W., 1996. Structural comparison of tektins and evidence for their determination of complex spacings in flagellar microtubules. Journal of Molecular Biology 257, 385–397.

Oda, T., Hirokawa, N., Kikkawa, M., 2007. Three-dimensional structures of the flagellar dynein-microtubule complex by cryoelectron microscopy. Journal of Cell Biology 177, 243–252.

Okuno, M. M., Brokaw, C. J. C., 1979. Inhibition of movement of trition-demembranated sea-urchin sperm flagella by Mg2+, ATP4-, ADP and P1. Journal of Cell Science 38, 105–123.

Pigino, G., Maheshwari, A., Bui, K. H., Shingyoji, C., Kamimura, S., Ishikawa, T., 2012. Comparative structural analysis of eukaryotic flagella and cilia from Chlamydomonas, Tetrahymena, and sea urchins. Journal of Structural Biology 178, 199–206.

Piperno, G., Mead, K., Shestak, W., 1992. The inner dynein arms I2 interact with a ”dynein regulatory complex” in Chlamydomonas flagella. Journal of Cell Biology 118, 1455–1463.

Polin, M., Tuval, I., Drescher, K., Gollub, J. P., Goldstein, R. E., 2009. Chlamydomonas swims with two ”gears” in a Eukaryotic version of run-and-tumble locomotion. Science 325, 487–490.

Purcell, E. M., Dec. 1976. Life at low Reynolds number. In: AIP Conference Proceedings Vol. 28. AIP, pp. 49–64.

Quarmby, L. M., 1996. Ca2+ influx activated by low pH in Chlamydomonas. Journal of General Physiology 108, 351–361.

Riedel-Kruse, I. H., Hilfinger, A., Howard, J., Jülicher, F., 2007. How molecular motors shape the flagellar beat. HFSP Journal 1, 192–208.

Rikmenspoel, R., 1978. Movement of sea urchin sperm flagella. Journal of Cell Biology 76, 310–322.

Ringo, D. L., 1967. Flagellar motion and fine structure of the flagellar apparatus in Chlamydomonas. Journal of Cell Biology 33, 543–571.

Roberts, A. J., Malkova, B., Walker, M. L., Sakakibara, H., Numata, N., Kon, T., Ohkura, R., Edwards, T. A., Knight, P. J., Sutoh, K., Oiwa, K., Burgess, S. A., 2012. ATP-driven remodeling of the linker domain in the dynein motor. Structure 20, 1670–1680.

Roberts, A. J., Numata, N., Walker, M. L., Kato, Y. S., Malkova, B., Kon, T., Ohkura, R., Arisaka, F., Knight, P. J., Sutoh, K., Burgess, S. A., 2009. AAA plus ring and linker swing mechanism in the dynein motor. Cell 136, 485–495.

Rüffer, U., Nultsch, W., 2005. High-speed cinematographic analysis of the movement of Chlamydomonas. Cell Motility 5, 251–263.

Ruhnow, F., Zwicker, D., Diez, S., 2011. Tracking single particles and elongated filaments with nanometer precision. Biophysical Journal 100, 2820–2828.

Sager, R., Granick, S., 1953. Nutritional studies with Chlamydomonas reinhardi. Annals of the New York Academy of Sciences 56, 831–838.

Sakakibara, H., Nakayama, H., 1989. Translocation of microtubules caused by the alpha beta, beta and gamma outer arm dynein subparticles of Chlamydomonas. Journal of Cell Science 111, 1155–1164.

Samso, M., Koonce, M. P., 2004. 25 angstrom resolution structure of a cytoplasmic dynein motor reveals a seven-member planar ring. Journal of Molecular Biology 340, 1059–1072.

Sanders, M. A., Salisbury, J. L., 1989. Centrin-mediated microtubule severing during flagellar excision in Chlamydomonas reinhardtii. Journal of Cell Biology 108, 1751–1760.

Schmidt, H., Gleave, E. S., Carter, A. P., 2012. Insights into dynein motor domain function from a 3.3-Å crystal structure. Nature Structural & Molecular Biology 19, 492–7– S1.

Segal, R. A. R., Huang, B. B., Ramanis, Z. Z., Luck, D. J. D., 1984. Mutant strains of Chlamydomonas reinhardtii that move backwards only. Journal of Cell Biology 98, 2026–2034.

Shannon, C. E., 1949. Communication in the presence of noise. Proceedings of the IEEE 86, 447 – 457.

Silflow, C. D., Lefebvre, P. A., 2001. Assembly and motility of eukaryotic cilia and flagella. Lessons from Chlamydomonas reinhardtii. Plant Physiology 127, 1500–1507.

Smith, E. F., Sale, W. S., 1991. Microtubule binding and translocation by inner dynein arm subtype I1. Cell Motility and the Cytoskeleton 18, 258–268.

Sowa, Y., Berry, R. M., 2008. Bacterial flagellar motor. Quarterly Reviews of Biophysics 41, 103–132.

Summers, K. E., Gibbons, I. R., 1971. Adenosine triphosphate-induced sliding of tubules in trypsin-treated flagella of sea-urchin sperm. Proceedings of the National Academy of Sciences 68, 3092–3096.

Tam, D., Hosoi, A. E., 2011. Optimal feeding and swimming gaits of biflagellated organisms. Proceedings of the National Academy of Science 108, 1001–1006.

Thompson, R. E., Larson, D. R., Webb, W. W., 2002. Precise nanometer localization analysis for individual fluorescent probes. Biophysical Journal 82, 2775–2783.

Tilney, L. G., Bryan, J., Bush, D. J., Fujiwara, K., Mooseker, M. S., Murphy, D. B., Snyder, D. H., 1973. Microtubules: evidence for 13 protofilaments. Journal of Cell Biology 59, 267–275.

Tynan, S. H., Gee, M. A., Vallee, R. B., 2000. Distinct but overlapping sites within the cytoplasmic dynein heavy chain for dimerization and for intermediate chain and light intermediate chain binding. Journal of Biological Chemistry 275, 32769–32774.

Ueno, H., Yasunaga, T., Shingyoji, C., Hirose, K., 2008. Dynein pulls microtubules without rotating its stalk. Proceedings of the National Academy of Sciences 105, 19702–19707.

Vincensini, L., Blisnick, T., Bastin, P., 2011. 1001 model organisms to study cilia and flagella. Biology of the Cell / under the Auspices of the European Cell Biology Organization 103, 109–130.

Walker, R. A., O'Brien, E. T., Pryer, N. K., Soboeiro, M. F., Voter, W. A., Erickson, H. P., Salmon, E. D., 1988. Dynamic instability of individual microtubules analyzed by video light microscopy: rate constants and transition frequencies. Journal of Cell Biology 107, 1437–1448.

Wiech, H., Geier, B. M., Paschke, T., Spang, A., Grein, K., Steinkotter, J., Melkonian, M., Schiebel, E., 1996. Characterization of green alga, yeast, and human centrins - Specific subdomain features determine functional diversity. Journal of Biological Chemistry 271, 22453–22461.

Witman, G., Mar. 2009. The Chlamydomonas Sourcebook: Cell Motility and Behavior. Academic Press.

Witman, G. B., 1986. Isolation of Chlamydomonas flagella and flagellar axonemes. Methods in Enzymology 134, 280–290.

Yagi, T., Uematsu, K., Liu, Z., Kamiya, R., 2009. Identification of dyneins that localize exclusively to the proximal portion of Chlamydomonas flagella. Journal of Cell Science 122, 1306–1314.